Uplift and exhumation of a mountain belt:

A stable isotopes and thermochronology approach to the Central Apennines of Italy, and its geodynamic implications

Malwina San Jose

Universita degli studi Roma Tre
Dipartimento di Scienze della Terra
XXXII° ciclo

November 2019

Table of content

Abstract

Estimates of surface uplift and exhumation are necessary to reconstruct the evolution of mountain belts and quantify the contributions of shallow and deep processes to the underlying geodynamics. We focus on the Central Apennines, which formed as an accretionary wedge before undergoing post-orogenic extension. Since ~2 Ma, it overlies an area of local slab detachment. We aim to better relate surface observations to possible geodynamic processes. To do so, we combine low-temperature thermochronology to date exhumation and stable isotope paleoaltimetry to reconstruct surface topography. Samples were collected from ten intermontane basins in the central Apennines that record both tectonic and climatic events.

We present 25 new apatite (U-Th)/He ages and 10 new apatite fission track ages. from Miocene sandstones range from 8 Ma on the Thyrrenean coast to 1.62 Ma in the Central-Eastern Apennines. This pattern reflects 1) the onset of extension in the Tyrrhenian back-arc basin during the Tortonian, 2) the progressive eastwards migration of the orogenic thrust front, and 3) a regional scale uplift signal around 2 Ma, with local exhumation rates >0.5 mm/yr of 2-4 km of crust. However, exhumation history does not necessarily translate into uplift history. To constrain paleoelevations, we also analyze 1488 lacustrine and paleosol carbonate $\delta^{18}O$ measurements collected from various elevations along the mountain range. Since the Pliocene, the gradient in $\delta 1^{8}O$ between basins near sea-level today and those at high-elevation today has continuously increased. We attribute this 5 ‰ shift to increasing orographic rainout, thereby causing progressively lower $\delta^{18}O$ in high-elevation basins as they are uplifted. Using this data and the modern meteoric water $\delta^{18}O$ lapse rate, we estimate that there has been more than 1 km of surface uplift since late Pliocene.

Both our isotopic data and exhumation ages record an uplift and exhumation signal in the high topography area of the central Apennines at 2Ma. This event matches the suggested timing and expected amplitude of slab break-off, and supports the hypothesis that the opening of the Adriatic slab window caused substantial uplift in the central Apennines since Late Pliocene.

Part 1

Rapid uplift of the central Apennines since the late Pliocene

Malwina San Jose[1,2], Jeremy K. Caves Rugenstein[2,3], Domenico Cosentino[1], Claudio Faccenna[1,4], Maria Giuditta Fellin[2], Massimiliano Ghinassi[5], Ivan Martini[6]

[1] *Dipartimento di Scienze, Università degli Studi Roma Tre, Largo S. L. Murialdo, 1, 00146 Roma, Italy*

[2]*Department of Earth Sciences, ETH Zürich, Sonneggstrasse 5 8092 Zürich, Switzerland*

[3]*Max Planck Institute for Meteorology, Bundesstr. 53 20251 Hamburg, Germany*

[4]*Jackson School of Geosciences, University of Texas at Austin, US*

[5]*Università di Padova, Dip. di Geoscienze, via G. Gradenigo, 6, 35131 Padova, Italy*

[6]*Department of Physical Sciences, Earth and Environment, University of Siena, Via Laterina 8, 53100, Siena, Italy*

ABSTRACT

The central Apennines, an accretionary wedge overlying an area of slab detachment, are characterized by prominent topography, active normal faulting, and high uplift rates. However, previous studies have failed to resolve the surface uplift history, complicating efforts to link the topographic evolution with underlying geodynamic processes. We aim to better quantify

orographic changes by using stable oxygen isotope paleoaltimetry. Modern surface water $\delta^{18}O$ are 5‰ lower at high elevation than at sea level, reflecting orographic rainout over the Apennines. We present 1,488 lacustrine and paleosol carbonate $\delta^{18}O$ measurements collected from ten extensional intermontane basins, spanning both high and low elevations. Since the Pliocene, $\delta^{18}O$ in high-elevation basins today has continuously decreased, even as $\delta^{18}O$ in lowland basins has remained constant over time. We attribute this continuous 5‰ shift to increased orographic rainout as the central Apennines were uplifted. We estimate an increase in mean elevation in excess of 1 km since late Pliocene. Our paleoelevation estimates match the suggested timing and expected amplitude of slab break-off related uplift. This supports the hypothesis that the opening of the Adriatic slab window and associated mantle flow contributed significantly to building topography in the central Apennines.

INTRODUCTION

The rise of mountain belts at convergent margins is the result of different contributions, derived from erosional unloading, crustal thickening and mantle dynamics. Disentangling, dating and quantifying their contributions to topographic growth remains challenging. In particular, topographic changes related to mantle and slab dynamics are commonly slower (Duretz et al., 2011; van Hunen and Allen, 2011) and easily overprinted by isostatic and climatic signals. However, the topography of subduction-type orogens are expected to be particularly sensitive to slab behaviour (e.g. Royden and Faccenna, 2018).

The Apennines—formed during the consumption of the Adria Plate (Patacca et al., 1990)— represent a remarkable example of a subduction orogen potentially influenced by mantle dynamics. Its topography culminates in the central portion of the orogenic chain, a region where the lack of deep seismicity, the presence of a low velocity anomaly in the upper

mantle, and the shallowing of the Moho have been considered as evidence of local slab break-off (Wortel and Spakman, 2000). These observations suggest that the modern topography of the central Apennines might also relate to deep geodynamic processes (e.g. Faure Walker et al., 2012; Faccenna et al., 2014). Further, a major change in the tectonic behaviour of the Central Apennines occurred in the early Pleistocene, at ~2.5-1.8 Ma, when thrusting along the orogenic front ceased (Patacca et al., 1990) and the entire region underwent extension (Cosentino et al., 2017). However, it is still unclear when the orogenic backbone attained its modern elevation. We rely on stable isotope paleoaltimetry to reconstruct the long-wavelength elevation of the central Apennines through time. Adiabatic decompression of an air mass over an orographic barrier causes preferential condensation and rainout of ^{18}O, thus resulting in lower precipitation $\delta^{18}O$ at higher elevations (e.g. Rowley and Garzione, 2007) and its preservation in authigenic carbonates formed in lacustrine sediments and paleosols. These deposits reflect the original $^{18}O/^{16}O$ ratio of meteoric water (Cerling and Quade, 1993) and can thus be used to evaluate the degree of rainout—related to elevation—at the time of deposition. We combine the existence of a large decrease in present-day precipitation $\delta^{18}O$ with elevation in the central Apennines with the unique preservation of Plio-Pleistocene sediments in both low- and high-elevation basins to constrain the difference between low and high-elevation meteoric paleo-$\delta^{18}O$ through time, thereby yielding constraints on the amplitude and timing of elevation change of the central Apennines.

GEOLOGIC AND CLIMATIC SETTING

The Apennine chain is a Neogene fold-and-thrust belt resulting from the westwards subduction of the Adriatic microplate (Royden et al., 1987). The frontal thrusts have progressively migrated towards the NE, mainly incorporating thick Meso-Cenozoic marine

limestones (Bally et al., 1986). The onset of rifting in the Tyrrhenian Sea during late Miocene lead to extensional tectonics, that were progressively superimposed on the thrust structures. Normal faults that steeply dip towards WSW cleave the Apennine chain in the westernmost part around 8 Ma, later shifting eastward towards the central part of the orogen (Patacca et al., 1993; Cosentino et al., 2017). The series of half-grabens thus created have evolved into intermontane basins filled with thick Plio-Pleistocene continental deposits, which are now spread along the Italian peninsula (Fig. 1). The ongoing extension and uplift in the central Apennines (~ 1 mm/yr) are well documented by geodetic data (e.g., Serpelloni et al., 2013), seismicity (e.g., Chiarabba et al., 2015), and geological records (e.g., Cosentino et al 2017).

The Apennines are characterized by a Mediterranean climate. Though precipitation is sourced from both the Atlantic/Western Mediterranean and the Adriatic/Eastern Europe, it predominantly comes from the west. Mean annual rainfall is approximately 800 mm, with higher amounts in areas with orographically-forced precipitation and at higher-elevation. This orographic precipitation induces a decrease in precipitation $\delta^{18}O$ of up to 5‰ between sea level and the high-elevation central Apennines (Longinelli and Selmo, 2003; Giustini et al., 2016; Fig. 1 and 2, DR Fig. 1).

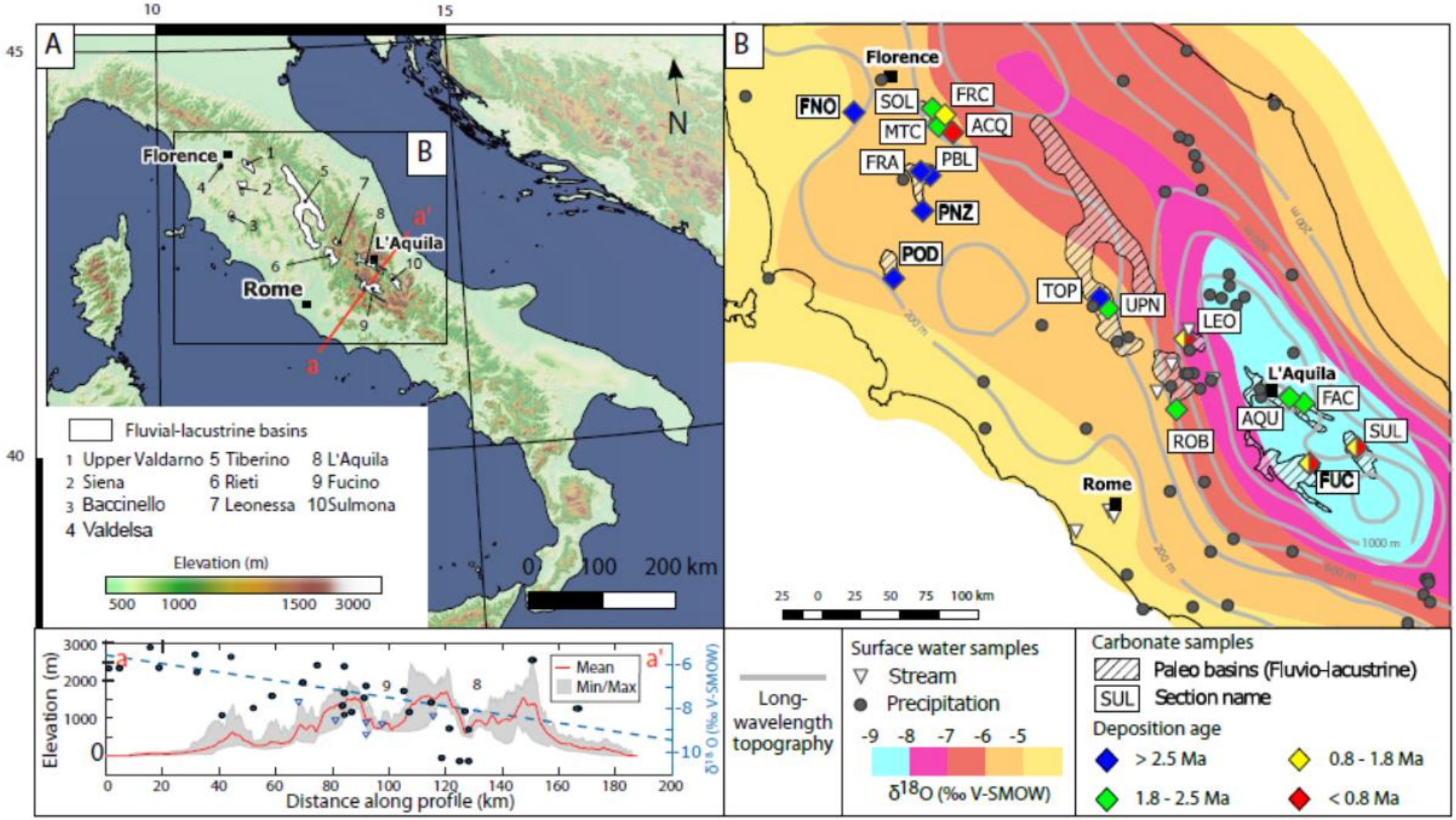

Figure 1: A. Topographic map of the Apennines (Italy) and location of the studied basins. a-a': topographic 40 km-wide swath profile across the central Apennines. δ18O water measurements within 1° of the profile are shown in blue; triangles and circles indicate data points respectively from this study and from Giustini et al., 2016; blue dashed line is a linear fit of the δ 18O data. Black box indicates the location of figure 1B: Location of sampled basins with the modern surface water δ18O as background shading (after Longinelli et al., 2003). Long wavelength topography calculated from DEM filtered with a 50 km-wide window is shown in grey. V-SMOW: Vienna standard mean ocean water

Table 1. Results of the isotope analysis for $\delta^{18}O$ and $\delta^{13}C$ in sediments (averages per section). Sample names: ACQ= Acquaborra Pit, FRA=Frasta Mine, FRC=Francalanci Pit, MTC= Montevarchio, PBL= Poggio Bonelli, POD= Podere La Locca, SOL= Solava Quarry, AQU= L'Aquila, FAC=Faccione section, LEO= Leonessa, ROB= Rieti Ornaro Basso, SUL=Sulmona, TOP=Cava Topetti, UPN= Upper Ponte Naja, FUC=Fucino, PNZ=Pienza, FNO=Fiano. GPS coordinates are given in the WGS84 reference frame. VPDB: measurements calibrated to the Vienna Pee Dee Belemnite ratio. Carbonate type: 1= paleosol (nodules, rootcasts), 2=lacustrine, 3=shell.

Basin	$\delta^{13}C$ (‰ VPDB ±1s)	$\delta^{18}O$ (‰ VPDB ±1s)	Elevation (m)	Deposition Age (Ma)	Latitude (° ' ")	Longitude (° ' ")	Carbonate type	Number of samples
				Tuscany				
ACQ	-11.70 ±1.39	-4.77 ±0.41	220	0.75	43 31 20	11 37 13	1	14
FNO	-9.52 ±0.73	-4.33 ±0.14	125	3.1	43 34 55	11 07 00	2	3
FRA	-9.34 ±2.24	-4.48 ±0.66	230	4	43 21 41	11 25 45	1	14
FRC	-8.68 ±2.50	-4.25 ±0.90	305	1.79	43 31 38	11 34 09	1	26
MTC	-6.05 ±1.09	-3.30 ±0.87	173	2.4	43 32 55	11 31 46	3	30
PBL	-5.68 ±0.99	-5.68 ±0.23	240	3	43 20 34	11 28 38	3	6
PNZ	-4.26 ±0.78	-4.52 ±0.35	125	4.5	43 03 50	11 40 25	2	4
POD *	-11.3 ±0.30	-3.61 ±0.15	280	6.6	42 48 46	11 22 55	1	11
SOL	-7.25 ±3.94	-5.04 ±0.45	170	1.85	43 37 37	11 29 59	1	32
				Central Apennines				
AQU	-3.02 ±2.23	-4.06 ±2.07	800	1.85	42 19 55	13 31 31	1, 2	10
FAC	-1.06 ±0.38	-5.90 ±0.73	812	2	42 16 55	13 35 31	2	36
LEO1	-1.60 ±0.66	-8.70 ±1.13	839	0.7	42 35 20	12 56 03	2, 3	6
LEO2	-1.99 ±1.49	-6.47 ±1.00	836	1.5	42 35 20	12 56 03	2, 3	20
ROB	1.36 ±0.79	-2.45 ±0.33	556	2.5	42 17 58	12 51 28	2	15
SUL1 †	-3.17 ±1.68	-9.23 ±0.85	500	0.2	42 05 50	13 52 59	2	634
SUL2 †	-1.46 ±0.55	-7.94 ±0.88	500	0.8	42 05 50	13 52 59	2	509
TOP	-0.72 ±0.25	-3.56 ±0.31	176	2.6	42 45 46	12 25 32	2	44
UPN	-2.19 ±0.78	-4.29 ±0.26	177	2	42 45 46	12 25 32	2	5
FUC1	-7.68 ±0.59	-6.23 ±0.33	850	0.36	41 59 45	13 40 14	1	4
FUC2 §	No data available	-4.06 ±0.80	600	0-1.8	41 59 46	13 34 11	2	64

*Data from Matson et al., 2012; † Data from Regattieri et al., 2016, 2017, 2019; § Data from Giaccio et al., 2015

METHODS AND APPROACH

To constrain high- and low-elevation changes in $\delta^{18}O$ through time, we sampled authigenic carbonates in both high- and low-elevation intermontane extensional basins that contain Plio-Pleistocene continental deposits and combine our records with published data. All of these samples consist primarily of lacustrine carbonate, carbonate nodules and rootcasts from paleosols, and interstitial carbonates within fluvial deposits. The depositional age of the sediments is constrained by bio- and magnetostratigraphic data and from dated ash layers (see DR). Low-elevation sites are currently at 100-350 m above sea level, within basins where continental deposits are interlayered with marine sediments, indicating deposition close to sea level. These low-elevation sites bear 189 samples and are picked up in nine sections (ACQ, FNO, FRA, FRC, MTC, PBL, PNZ, SOL and POD), which come from four basins in the Tuscan lowlands (Fidolini et al., 2013; Ghinassi et al., 2013), and of two sections (TOP, UPN) from the central Apennines (Fig. 1; Table 1). Our high-elevation sites are distributed in five basins in the central Apennines, between 550 and 1000 m and surrounded by 2 to 3 km high ranges (Fig. 1; Table 1). They are comprised of four new sections (AQU, FAC, FUC1 and ROB) consisting of 92 samples, that we combine with 1207 data-points from two cores (FUC2, SUL) examined in previous studies (Giaccio et al., 2015; Regattieri et al., 2016, 2017, 2019). We measured the $\delta^{18}O$ and $\delta^{13}C$ of these samples using a ThermoFisher Delta V and a GasBench at ETH Zürich. We also collected nine spring and stream water samples to supplement existing precipitation $\delta^{18}O$ data (Longinelli and Selmo, 2003; Giustini et al., 2016). These waters were measured for $\delta^{18}O$ on a Picarro CRDS at ETH Zürich. Because streams drain surface waters from the surrounding highlands, we correct our sampling altitude for the mean hypsometry of the drainage basin located upstream of the sampling point (Hoke et al., 2014).

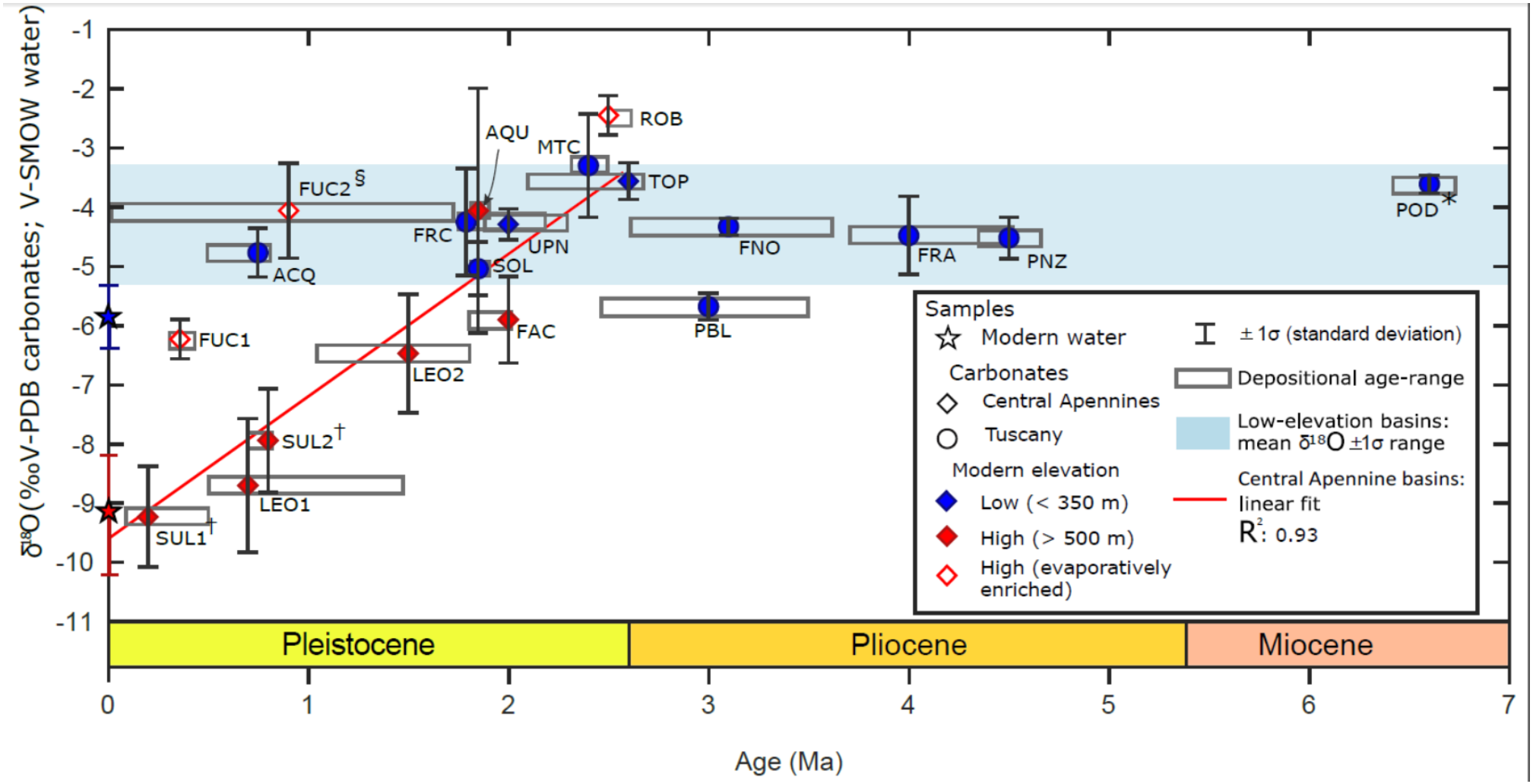

*Figure 2. Average δ18O of the sampled basins and their estimated formation age, and modern water δ18O binned by elevation. Number of individual samples per basin (3 to 634) are given in Table 1. Grey boxes show the full possible age ranges of our carbonate samples. The estimated carbonate ages are constrained by their stratigraphic location relative to layers of known depositional age (see DR). Blue and red stars indicate modern water composition at sea level (<100 m) and at the highest sampled elevations (>1500 m), respectively. * indicates data from Matson et al., 2012. † data from Regattieri et al., 2016, 2017, 2019. § data from Giaccio et al., 2015. V-SMOW: Vienna standard mean ocean water. V-PDB: Vienna Pee Dee Belemnite.*

RESULTS

We present the results binned by basin and by deposition age (Fig 2). Each basin contains from 3 to 44 samples, either within the same stratigraphic layer, or along a vertical section. Carbonate $\delta^{18}O$ values from low-elevation basins vary between -5.27 and -3.39‰ (1σ range; blue shading in Fig. 2), and there is no apparent long-term trend. Values of $\delta^{18}O$ from central Apennine basins range from -3‰ to -10‰ and show a significant decrease with time (Fig. 2). We estimate a $\delta^{18}O$ decrease of ~5.3 ‰ (+/– 1.5‰) from 2.6 Ma to 0.5 Ma, based on a linear fit weighted by the 1σ of the basin average. This decreasing trend can also be observed among samples from the same basin but with significantly different depositional ages; for example, in both SUL and LEO, deposits separated by approximately 1 My have lower $\delta^{18}O$ values in stratigraphically higher samples (Fig. 2).

DISCUSSION

Prior to 2 Ma, both Tuscany and the central Apennines are characterized by high $\delta^{18}O$ values (-3 to -5 ‰). After 2 Ma, $\delta^{18}O$ diverges between these two regions. In Tuscany, $\delta^{18}O$ values remain in the same high range, likely reflecting approximately constant $\delta^{18}O$ since the late Miocene. Further, the low elevation sections within the central Apennines (TOP, UPN) are also the oldest and their mean $\delta^{18}O$ value falls within the 1σ range of the mean $\delta^{18}O$ value of lowland basins in Tuscany. In the central Apennines, $\delta^{18}O$ progressively decreases from -3 to -10 ‰ such that, remarkably, the $\delta^{18}O$ difference between the mean values of the youngest samples in the high- and low-elevation basins is equivalent to the modern-day meteoric water $\delta^{18}O$ difference between the coast and high elevation. This decreasing trend could reflect*:* (1) increased orographic rainout in areas where mean elevation increased over the last 2 My, (2) a

shift from endorheic to exorheic conditions in the lacustrine basins, and/or (3) Plio-Pleistocene climate change towards colder conditions. We rule out long-term Plio-Pleistocene climate change as a driver of the observed decrease in high-elevation $\delta^{18}O$ as lowland $\delta^{18}O$ remains approximately constant over time (Fig. 2), and climate change would likely impart a measurable shift in lower-elevation $\delta^{18}O$ as well. Further, even though changing lapse rates may shift high-elevation $\delta^{18}O$ independently from low-elevation $\delta^{18}O$ (Poulsen and Jeffery, 2011), it is unlikely to account for the entirety of the 5‰ high-elevation decrease that we observe given that mean late Pliocene climate was not substantially warmer than in the late Pleistocene (Lisiecki and Raymo, 2005). The shift from closed to open basins can be assessed by the covariance of $\delta^{18}O$ and $\delta^{13}C$ in lacustrine facies (Talbot, 1990). In most of lacustrine basins we studied, $\delta^{18}O$ and $\delta^{13}C$ vary independently and there is no clear geomorphological evidence for an endorheic stage, supporting the idea that the recent outward drainage is not the main driver of $\delta^{18}O$ decrease. The two basins that do show geomorphological evidence for endorheic basin conditions are the Fucino Basin (D'Agostino et al., 2001) and the Rieti Basin (Cosentino et al., 2014) (FUC1, FUC2, and ROB). Samples from ROB are remarkably characterized by both $\delta^{18}O$ and $\delta^{13}C$ values higher than the 2σ standard deviation of our dataset (Data Repository Figure DR2). We therefore consider these outlier $\delta^{18}O$ values as influenced substantially by evaporation and exclude them from the tectonic interpretation.

Consequently, we conclude that an increase in orographic rainout since the late Pliocene is most likely the primary process behind the progressive decrease in $\delta^{18}O$ in the central Apennines. We attribute increased orographic rainout to growth of topography within the central Apennines since 2 Ma. Given the modern isotopic lapse rate of 2 ‰/km, the minimum shift (3.8 ‰) that we observe within basins of comparable modern elevation suggests an increase in mean elevation in excess of 1 km. We note that the preponderance of lacustrine carbonate samples from high-elevation basins suggests that this estimate relates to the change

in long wavelength elevation, rather than the height of individual ranges or basins, as lacustrine carbonate $\delta^{18}O$ likely averages surface water over the scale of the drainage basin. That the difference in $\delta^{18}O$ between the youngest samples in the high- and low-elevation basins resembles the modern water $\delta^{18}O$ difference lends credence to our inference that carbonate $\delta^{18}O$ is faithfully recording the change in the meteoric water $\delta^{18}O$ with elevation through time.

IMPLICATIONS

Our new stable isotope data provide critical constraints on the history of topography within the central Apennines. Previous studies have suggested an increase in exhumation and normal faulting since the Pliocene, mainly based upon geomorphology (Galadini et al., 2003) and stratigraphy (Cosentino et al., 2017). Our results support the notion of a corresponding major change in surface elevation since the late Pliocene, and provide the first direct dating of surface uplift in the area. This timing compares well with the sealing of the latest thrust faults in the Adriatic foredeep, which has been linked to the cessation of subduction by slab break-off and of hypothesized uplift based upon 2–3 Ma angular unconformities within Pliocene foredeep deposits in the Adriatic foreland (Pizzi, 2003; Bigi et al., 2013). Though our results alone cannot uniquely identify the mechanism driving surface uplift, both the timing and magnitude of topographic uplift support inferences that slab detachment occurred in the late Pliocene-early Pleistocene, resulting in concomitant surface uplift. We thus provide the first direct dating of slab break-off and associated topographic growth. The uplift rates inferred by this study (>0.5 km/My) are both within range of those suggested by previous geodetic and geological data (Faccenna et al., 2014), and of those expected by shallow slab break-off (Duretz et al., 2011). Our study demonstrates the utility of linking spatially and temporally resolved authigenic carbonate stable isotope data to unravel the mechanisms that build topography in

subduction-zone orogens. Further work will elucidate how other surface processes, including drainage reorganization and erosion, responded to the rapid Plio-Pleistocene uplift of the central Apennines.

ACKNOWLEDGMENTS

The project is funded by the European Union's Horizon 2020 research and innovation programme under the Marie Skłodowska-Curie grant agreement No 674899. JKCR is funded by ETH and Alexander von Humboldt Postdoctoral Fellowships. The grant to Dipartimento di Scienze, Università degli Studi Roma Tre (MIUR-Italy Dipartimenti di Eccellenza, articolo 1, commi 314 – 337 legge 232/2016) is gratefully acknowledged. We are thankful to B. Giaccio and to E. Regattieri for sharing their dataset and their constructive discussions.

REFERENCES CITED

Aldinucci, M., Benvenuti, M., Andreetta, A., Dominici, S., Foresi, L.M., Carnicelli, S., and Martini, I., 2019, Composite sequence stratigraphic patterns in alluvial to shallow-marine successions: Examples from the Piacenzian of the Valdelsa Basin (Central Italy): Sedimentary Geology, v. 388, p. 99–113, doi:10.1016/j.sedgeo.2019.05.005.

Bally, A.W., Burbi, L., Cooper, C., and Ghelardoni, R., 1986, Balanced sections and seismic reflection profiles across the central Apennines: Memorie della Società Geologica Italiana, v. 35, p. 257–310.

Basilici, G., 1997, Sedimentary facies in an extensional and deep-lacustrine depositional system: The Pliocene Tiberino Basin, Central Italy: Sedimentary Geology, v. 109, p. 73–94, doi:10.1016/S0037-0738(96)00056-5.

Bertini, A., Magi, M., Mazza, P.P.A., and Fauquette, S., 2010, Impact of short-term climatic events on latest Pliocene land settings and communities in Central Italy (Upper Valdarno basin): Quaternary International, v. 225, p. 92–105, doi:10.1016/j.quaint.2009.05.011.

Bigi, S., Conti, A., Casero, P., Ruggiero, L., Recanati, R., and Lipparini, L., 2013, Geological model of the central Periadriatic basin (Apennines, Italy): Marine and Petroleum Geology, v. 42, p. 107–121, doi:10.1016/j.marpetgeo.2012.07.005.

Bougeois, L., de Rafélis, M., Reichart, G.J., de Nooijer, L.J., Nicollin, F., and Dupont-Nivet, G., 2014, A high resolution study of trace elements and stable isotopes in oyster shells to estimate central asian middle eocene seasonality: Chemical Geology, v. 363, p. 200–212, doi:10.1016/j.chemgeo.2013.10.037.

Breitenbach, S.F.M., and Bernasconi, S.M., 2011, Carbon and oxygen isotope analysis of small carbonate samples (20 to 100 μg) with a GasBench II preparation device: Rapid Communications in Mass Spectrometry, v. 25, p. 1910–1914, doi:10.1002/rcm.5052.

Casero, P., 2004, Structural setting of petroleum exploration plays in Italy: Special Volume of the Italian Geological Society for the IGC 32, v. 107, p. 319–322.

Cavinato, G.P., Carusi, C., Dall'asta, M., Miccadei, E., and Piacentini, T., 2002, Sedimentary and tectonic evolution of Plio-Pleistocene alluvial and lacustrine deposits of Fucino Basin (central Italy): Sedimentary Geology, v. 148, p. 29–59, doi:10.1016/S0037-0738(01)00209-3.

Cavinato, G.P., Cosentino, D., Funiciello, R., Parotto, M., Salvini, F., and Tozzi, M., 1994, Constraints and new problems for geodynamical modelling of central Italy (CROP11 Civitavecchia - Vasto deep seismic line): Bolletino di Geofisica Teorica ed Applicata, v. 36, p. 141–144.

Cerling, T.E., and Quade, J., 1993, Stable Carbon and Oxygen Isotopes in Soil Carbonates: 217–231 p., doi:10.1029/GM078p0217.

Chiarabba, C., De Gori, P., and Mele, F.M., 2015, Recent seismicity of Italy: Active tectonics of the central Mediterranean region and seismicity rate changes after the Mw 6.3 L'Aquila earthquake: Tectonophysics, v. 638, p. 82–93, doi:10.1016/j.tecto.2014.10.016.

Cosentino, D. et al., 2017, New insights into the onset and evolution of the central Apennine extensional intermontane basins based on the tectonically active L'Aquila Basin (central Italy): Bulletin of the Geological Society of America, v. 129, p. 1314–1336, doi:10.1130/B31679.1.

Cosentino, D. et al., 2008, Note Illustrative della carta geologica d'Italia alla scala 1:50.000 Foglio 357 Cittaducale:

D'Agostino, N., Jackson, J.A., Dramis, F., and Funiciello, R., 2001, Interactions between mantle upwelling, drainage evolution and active normal faulting: An example from the Central Appennines (Italy): Geophysical Journal International, v. 147, p. 475–497, doi:10.1046/j.1365-246X.2001.00539.x.

Duretz, T., Gerya, T. V., and May, D.A., 2011, Numerical modelling of spontaneous slab breakoff and subsequent topographic response: Tectonophysics, v. 502, p. 244–256, doi:10.1016/j.tecto.2010.05.024.

Faccenna, C., Becker, T.W., Miller, M.S., Serpelloni, E., and Willett, S.D., 2014, Isostasy, dynamic topography, and the elevation of the Apennines of Italy: Earth and Planetary Science Letters, v. 407, p. 163–174, doi:10.1016/j.epsl.2014.09.027.

Faure Walker, J.P., Roberts, G.P., Cowie, P.A., Papanikolaou, I., Michetti, A.M., Sammonds, P., Wilkinson, M., McCaffrey, K.J.W., and Phillips, R.J., 2012, Relationship between topography, rates of extension and mantle dynamics in the actively-extending Italian Apennines: Earth and Planetary Science Letters, v. 325–326, p. 76–84, doi:10.1016/j.epsl.2012.01.028.

Fidolini, F., Ghinassi, M., Magi, M., Papini, M., and Sagri, M., 2013, The plio-pleistocene fluvio-lacustrine upper valdarno basin (central Italy): Stratigraphy and Basin fill evolution: Italian Journal of Geosciences, v. 132, p. 13–32, doi:10.3301/IJG.2012.06.

Fubelli, G., Falcucci, E., Mei, A., and Dramis, F., 2008, Evoluzione Quaternaria Del Bacino Di Leonessa (Rieti): Il Quaternario, v. 21(2), p. 457–468.

Fubelli, G., Della Seta, M., and Amato, G., 2014, Drainage system adjustment in response to the opening of the Rieti intermontane basin (Central Italy): geostatistical reconstruction of the PaleoFarfa River alluvial plain: Rendiconti Lincei, v. 25, p. 167–176, doi:10.1007/s12210-014-0322-0.

Galadini, F., Messina, P., Giaccio, B., and Sposato, A., 2003, Early uplift history of the Abruzzi Apennines (central Italy): Available geomorphological constraints: Quaternary International, v. 101, p. 125–135, doi:10.1016/S1040-6182(02)00095-2.

Ghinassi, M., Abbazzi, L., Esu, D., Gaudant, J., and Girotti, O., 2005, Facies analysis, stratigraphy

and palaeontology (Molluscs and Vertebrates) in the Upper Pliocene sandy flood-basin deposits of the Upper Valdarno Basin (Northern Apennines): Rivista Italiana di Paleontologia e Stratigrafia, v. 111, p. 467–487.

Ghinassi, M., Fidolini, F., Magi, M., and Sagri, M., 2013, Depositional environments of the plio-pleistocene upper Valdarno Basin (Tuscany, Italy): Italian Journal of Geosciences, v. 132, p. 33–53, doi:10.3301/IJG.2012.07.

Giaccio, B. et al., 2015, A key continental archive for the last 2Ma of climatic history of the central Mediterranean region: A pilot drilling in the Fucino Basin, central Italy: Scientific Drilling, v. 20, p. 13–19, doi:10.5194/sd-20-13-2015.

Giustini, F., Brilli, M., and Patera, A., 2016, Mapping oxygen stable isotopes of precipitation in Italy: Journal of Hydrology: Regional Studies, v. 8, p. 162–181, doi:10.1016/j.ejrh.2016.04.001.

Hoke, G.D., Liu-Zeng, J., Hren, M.T., Wissink, G.K., and Garzione, C.N., 2014, Stable isotopes reveal high southeast Tibetan Plateau margin since the Paleogene: Earth and Planetary Science Letters, v. 394, p. 270–278, doi:10.1016/j.epsl.2014.03.007.

van Hunen, J., and Allen, M.B., 2011, Continental collision and slab break-off: A comparison of 3-D numerical models with observations: Earth and Planetary Science Letters, v. 302, p. 27–37, doi:10.1016/j.epsl.2010.11.035.

Kirby, M.X., 2000, Paleoecological Differences between Tertiary and Quaternary Crassostrea Oysters, as Revealed by Stable Isotope Sclerochronology: Palaios, v. 15, p. 132, doi:10.2307/3515499.

Lisiecki, L.E., and Raymo, M.E., 2005, A Pliocene-Pleistocene stack of 57 globally distributed benthic δ 18 O records: Paleoceanography, v. 20, p. 1–17, doi:10.1029/2004PA001071.

Longinelli, A., and Selmo, E., 2003, Isotopic composition of precipitation in Italy: a first overall map: Journal of Hydrology, v. 270, p. 75–88.

Mancini, M., D'Anastasio, E., Barbieri, M., and De Martini, P.M., 2007, Geomorphological, paleontological and87Sr/86Sr isotope analyses of early Pleistocene paleoshorelines to define the uplift of Central Apennines (Italy): Quaternary Research, v. 67, p. 487–501, doi:10.1016/j.yqres.2007.01.005.

Martini, I., and Aldinucci, M., 2017, Sedimentation and Basin-Fill History of the Pliocene Succession Exposed in the Northern Siena-Radicofani Basin (Tuscany, Italy): a Sequence-Stratigraphic Approach: Riv. It. Paleontol. Strat, v. 123, p. 407–432, https://www.researchgate.net/profile/Ivan_Martini/publication/319353769_Sedimentation_and_basin-fill_history_of_the_pliocene_succession_exposed_in_the_Northern_Siena-Radicofani_Basin_Tuscany_Italy_A_sequence-stratigraphic_approach/links/59a6c3e80f7e9b41b7.

Martini, I., Aldinucci, M., Foresi, L.M., Mazzei, R., and Sandrelli, F., 2011, Geological map of the Pliocene succession of the Northern Siena Basin (Tuscany, Italy): Journal of Maps, v. 7, p. 193–205, doi:10.4113/jom.2011.1176.

Martini, I.P., and Sagri, M., 1993, Tecto-sedimentary characteristics of Late Miocene-Quaternary extensional basins of the Northern Apennines, Italy: Earth Science Reviews, v. 34, p. 197–233, doi:10.1016/0012-8252(93)90034-5.

Nocentini, M., Asti, R., Cosentino, D., Durantec, F., Gliozzi, E., Macerola, L., and Tallini, M., 2017, Plio-quaternary geology of L'Aquila-Scoppito basin (Central Italy): Journal of Maps, v. 13, p. 563–574, doi:10.1080/17445647.2017.1340910.

Patacca, E., Sartori, R., and Scandone, P., 1990, Tyrrhenian basin and Apenninic Arcs: kinematic relations since Late Tortonian times.: Mem. Soc. Geol. It, v. 45, p. 425–451, doi:10.1007/978-94-011-2016-6_7.

Pizzi, A., 2003, Plio-Quaternary uplift rates in the outer zone of the central Apennines fold-and-thrust belt, Italy: Quaternary International, v. 101–102, p. 229–237, doi:10.1016/S1040-6182(02)00105-2.

Poage, M.A., and Chamberlain, C.P., 2001, Stable isotope composition of precipitation and surface waters: considerations for studies of paleoelevation change: American Journal of Science, v. 301, p. 1–15, http://www.ajsonline.org/content/301/1/1.full.pdf.

Poulsen, C.J., and Jeffery, M.L., 2011, Climate change imprinting on stable isotopic compositions of high-elevation meteoric water cloaks past surface elevations of major orogens: Geology, v. 39, p. 595–598, doi:10.1130/G32052.1.

Regattieri, E. et al., 2017, A Last Interglacial record of environmental changes from the Sulmona Basin (central Italy): Palaeogeography, Palaeoclimatology, Palaeoecology, v. 472, p. 51–66, doi:10.1016/j.palaeo.2017.02.013.

Regattieri, E. et al., 2019, Frequency and dynamics of millennial-scale variability during Marine Isotope Stage 19: Insights from the Sulmona Basin (central Italy): Quaternary Science Reviews, v. 214, p. 28–43, doi:10.1016/j.quascirev.2019.04.024.

Regattieri, E., Giaccio, B., Galli, P., Nomade, S., Peronace, E., Messina, P., Sposato, A., Boschi, C., and Gemelli, M., 2016, A multi-proxy record of MIS 11-12 deglaciation and glacial MIS 12 instability from the Sulmona basin (central Italy): Quaternary Science Reviews, v. 132, p. 129–145, doi:10.1016/j.quascirev.2015.11.015.

Rowley, D.B., and Garzione, C.N., 2007, Stable Isotope-Based Paleoaltimetry: Annual Review of Earth and Planetary Sciences, v. 35, p. 463–508, doi:10.1146/annurev.earth.35.031306.140155.

Royden, L., and Faccenna, C., 2018, Subduction Orogeny and the Late Cenozoic Evolution of the Mediterranean Arcs: Annual Review of Earth and Planetary Sciences, v. 46, p. 261–289, doi:10.1146/annurev-earth-060115-012419.

Royden, L., Patacca, E., and Scandone, P., 1987, Segmentation and configuration of subducted lithosphere in Italy: an important control on thrust-belt and foredeep-basin evolution.: Geology, v. 15, p. 714–717, doi:10.1130/0091-7613(1987)15<714:SACOSL>2.0.CO;2.

Serpelloni, E., Faccenna, C., Spada, G., Dong, D., and Williams, S.D.P., 2013, Vertical GPS ground motion rates in the Euro-Mediterranean region: New evidence of velocity gradients at different spatial scales along the Nubia-Eurasia plate boundary: Journal of Geophysical Research: Solid Earth, v. 118, p. 6003–6024, doi:10.1002/2013JB010102.

Spadi, M., 2018, Ostracod Assemblages From the Palaeolake Tiberino (Piacenzian-Gelasian , Central Italy): a Synthesis: v. 31, p. 193–197.

Spadi, M., Gliozzi, E., Cosentino, D., and Nocentini, M., 2016, Late Piacenzian–Gelasian freshwater ostracods (Crustacea) from the L'Aquila Basin (central Apennines, Italy): Journal of Systematic Palaeontology, v. 14, p. 617–642, doi:10.1080/14772019.2015.1079561.

Spadi, M., Gliozzi, E., and Medici, M.C., 2017, A Plio–Pleistocene Caspiocypris species flock (Candoninae, Ostracoda) from the Palaeolake Tiberino (Umbria, central Italy): Journal of Systematic Palaeontology, v. 2019, p. 1–18, doi:10.1080/14772019.2017.1310143.

Talbot, M.R., 1990, A review of the palaeohydrological interpretation of carbon and oxygen isotopic composition: Chemical Geology, v. 80, p. 261–279.

Wortel, M.J.R., and Spakman, W., 2000, Subduction and slab detachment in the Mediterranean-Carpathian region: Science, v. 290, p. 1910–1917, doi:10.1126/science.290.5498.1910.

Zarlenga, F., 1987, I depositi continentali del bacino del Fucino (L'aquila, Italia centrale): Geologica Romana, v. 26, p. 223–253.

Zhong, S., and Gurnis, M., 1994, Controls on trench topography from dynamic models of subducted

slabs: Journal of Geophysical Research, v. 99, p. 15683, doi:10.1029/94JB00809.

Data Repository

Rapid uplift of the central Apennines since the late Pliocene

Malwina San Jose[1,2], Jeremy K. Caves Rugenstein[2,3], Domenico Cosentino[1], Claudio Faccenna[1,4], Maria Giuditta Fellin[2], Massimiliano Ghinassi[5], Ivan Martini[6]

[1] *Dipartimento di Scienze, Università degli Studi Roma Tre, Largo S. L. Murialdo, 1, 00146 Roma, Italy*

[2]*Department of Earth Sciences, ETH Zürich, Sonneggstrasse 5 8092 Zürich, Switzerland*

[3]*Max Planck Institute for Meteorology, Bundesstr. 53 20251 Hamburg, Germany*

[4]*Jackson School of Geosciences, University of Texas at Austin, US*

[5]*Università di Padova, Dip. di Geoscienze, via G. Gradenigo, 6, 35131 Padova, Italy*

[6]*Department of Physical Sciences, Earth and Environment, University of Siena, Via Laterina 8, 53100, Siena, Italy*

Table of contents

A. SAMPLE DESCRIPTION AND DATING CONSTRAINTS

1. Tuscan Basins

a. Upper Valdarno Basin

ACQ (Acquaborra) comes from the uppermost fluvial deposits outcrop (Torrente Ciuffenna synthem) in the Acquaborra pit. The unit's age is younger than the Matuyama-Bruhnes boundary at 0.78 Ma, making it our youngest sample from the Upper Valdarno Basin (Fidolini et al., 2013). The deposits are mainly fluvial sands and gravels, with many pedogenized, clay-rich overbank layers. The abundant vertic features and carbonate nodules with clay coatings are characteristic of soils developing in a well-drained environment.

FRC (Francalanci Quarry) is set in the Montevarchi synthem (VRCg and VRCe in Fidolini et al., 2013). Stratigraphically, it overlays a tephra layer dated 2.21 Ma and ends with the Olduvai subchron inversion at 1.78 Ma. The deposit consists of interfingering sand-dominated layers and argillaceous beds, respectively channelized and overbank deposits of the axial alluvial system. Several horizons have been heavily pedogenized, yielding lignite debris as well as root casts and carbonate nodules that we used for analysis.

The MTC samples (Montecarlo section, Ghinassi et al., 2005) come from the unit designated as VRCc in Fidolini et al., 2013 and dated ca. 2.3 to 2.5 Ma (Early Gelasian, described as from the Early-Mid Villafranchian mammal age), based on a tephra age (2.21 Ma) and the Gauss-Matuyama boundary (2.58 Ma). The MTC section yields layers rich in freshwater mollusc shells, mostly broken and not in life position, alternating with more silty layers. These facies hint at a depositional environment with variable hydrology, shifting between small channels and shoal ponds. We measured the isotopic composition of carbonate bioclasts from gastropods and bivalves.

SOL (Solava clay pit) in the so-called Poggio Rosso succession in the Montevarchi synthem has been magnetostratigraphically correlated to the Olduvai period, between 1.8 and 1.9 Ma (Bertini et al., 2010). The deposits are silts and sands, with 5 to 50 cm thick pedogenized beds showing dessication cracks, root casts, and abundant carbonate nodules up to 2 cm in size. Large mammal fossils have been found in the same unit, indicative of a vegetated floodplain environment. We sampled 3 to 20 mm large nodules in charcoal bearing layers, as well as root casts.

b. Siena Basin

FRA (Frasta Mine) was sampled from an outcrop composed of silty floodplain deposits. The Zanclean age is constrained by micropaleontological evidence from the overlying shoreface and deltaic sands. The 30 m thick layer is dominantly comprised of a clay matrix with thin-bedded sands and few lens-shaped gravel bodies, referred as facies A1 in Martini et al. (2011). Interbedded peat layers and continental molluscs indicate an on-shore depositional environment. We sampled carbonate concretions from strongly pedogenized clay-rich horizons (Martini et al., 2011).

PBL (Poggio Bonelli) is from a unit dated to the late-middle Pliocene (biostratigraphically constrained unit S3 in Martini and Aldinucci, 2017). The deposit consists of coarse sand with abundant bioclasts in life position, reflecting a low-energy fluvial environment with limited sediment supply. The deposit was later drowned by a marine transgression, as shown by the overlying marine deltaic deposits containing marine shells. We collected continental carbonates among which bivalves and concretions.

PNZ (Pienza) samples consist of lacustrine material from the early Pliocene Siena Basin. PNZ was sampled among lacustrine carbonates rich in organic matter. The lacustrine deposit is interbedded with a marine succession, dated to the Zanclean. The coeval marine shoreline is a few kilometres west from the sampling point, indicating that its paleo-elevation is near 0 m (Martini and Sagri, 1993; Martini et al., 2011; Martini and Aldinucci, 2017).

c. Valdelsa Basin

FNO (Fiano) samples come from a fluvial succession interbedded with marine deposits. We sampled carbonate nodules from the Piacenzian pedogenized horizons occurring within the continental deposits (Aldinucci et al., 2019).

2. Central Apennine Basins

The Tiberino basin mostly yields late Piacenzian-Gelasian deep-lake deposits dated by faunal assemblages and magnetostratigraphy (Basilici, 1997; Spadi, 2018). The TOP samples are from the unit described as the Fosso Bianco Formation, the oldest lacustrine infill of the basin, and UPN samples are from the overlying Ponte Naja Formation. The facies are white silty clays, deposited in a distal lacustrine environment.

The L'Aquila basin contains deep-lake facies in the San Nicandro Formation, dated to the late Piacenzian-Gelasian by faunal assemblages, which include a Plio-Pleistocene *Caspiocypris* species flock similar to that described for the Tiberino Basin (Spadi et al., 2016; Nocentini et al., 2018). We sampled the FAC section in the San Nicandro Formation. The younger deposits from L'Aquila basin (AQU) are from red paleosol layers interbedded within fluvial deposits in the Petogna Quarry (Valle dell'Inferno Formation). For its stratigraphical position, the Valle dell'Inferno Formation is considered upper Gelasian (Nocentini et al., 2018). The top of the Valle dell'Inferno Formation (Valle Daria paleosurface) represents the abandoned surface of the drainage system that corresponds to a regionally extensive uplift event in the central Apennines (ca. 2 Ma).

The Rieti basin (sampled in the Ornaro Basso locality - ROB) is infilled with lacustrine material from the late Pliocene-early Pleistocene, mainly white-greyish carbonate clays with a few organic-matter-rich horizons (Cosentino et al., 2008). These deposits pre-date the opening of the Rieti basin due to later Quaternary fault activity (Fubelli et al., 2014). Prior to the opening of the basin, the Rieti basin was likely closed (e.g., Ornaro Basso Unit; Cosentino et al., 2014), causing the carbonate $\delta^{18}O$ to be evaporatively enriched.

Leonessa (LEO) is a higher-elevation subdivision of the Rieti basin. We sampled Bithynia opercules from lignite horizons, and carbonate-rich clay deposits in the Villa Pulcini synthem, characteristic of cold shallow lake to palustrine conditions. The section has been dated to the lower part of middle Pleistocene (Galerian mammal age) via biostratigraphy (Fubelli et al., 2008).

In the Fucino basin, the paleosols sampled by this study (FUC1) are younger in age than the lacustrine sediments sampled by Giaccio et al. (2015) (FUC2). They outcrop as a white/red pedogenized layer among coarse alluvial deposits in the eastern part of the basin. We stratigraphically correlate them to the red paleosols from the Mindel-Riss stage described in Zarlenga (1987).

B. STABLE ISOTOPES METHOD

1. Carbonate Samples

Bulk samples were powdered using either a Dremel or a mortar and pestle. Individual shells and nodules were extracted and washed with deionized water, then dried for 24-48 hours

in a 40°C oven. Depending on the sample's carbonate content, 90 to 300 µg of sample powder was enclosed in 12.5 mL vials and flushed with Helium before being reacted with phosphoric acid at 72°C for 1 hour. Stable O and C isotope values were determined using a ThermoFinnigan (Bremen, Germany, now Thermo Fisher Scientific) GasBench II, equipped with a CTC autosampler (CTC Analytics AG, Zwingen, Switzerland), and coupled to a ConFlow IV interface and a Delta V Plus mass spectrometer (both Thermo Fisher Scientific) at the ETH Zurich (Breitenbach and Bernasconi, 2011). The internal standard deviation (measured on internal Carrara marble standards and international standards NBS18 and NBS19) is <0.07 ‰ for $\delta^{18}O$. The results are reported with respect to VPDB (Vienna Pee Dee Belemnite).

2. Water Samples

Measurements of water $\delta^{18}O$ were made on a Picarro L2120-i isotopic water analyzer coupled to a Picarro A0211 High Precision Vaporizer at ETH Zurich (Switzerland). Water aliquots of 1 mL were filtered through 0.45 µm disposable membrane filters before injection. Values of $\delta^{18}O$ and δD were calibrated using secondary water standards (standardized using IAEA primary water standards) injected at regular intervals. The data was processed using Picarro's ChemCorrect software to report mean and standard deviation values.

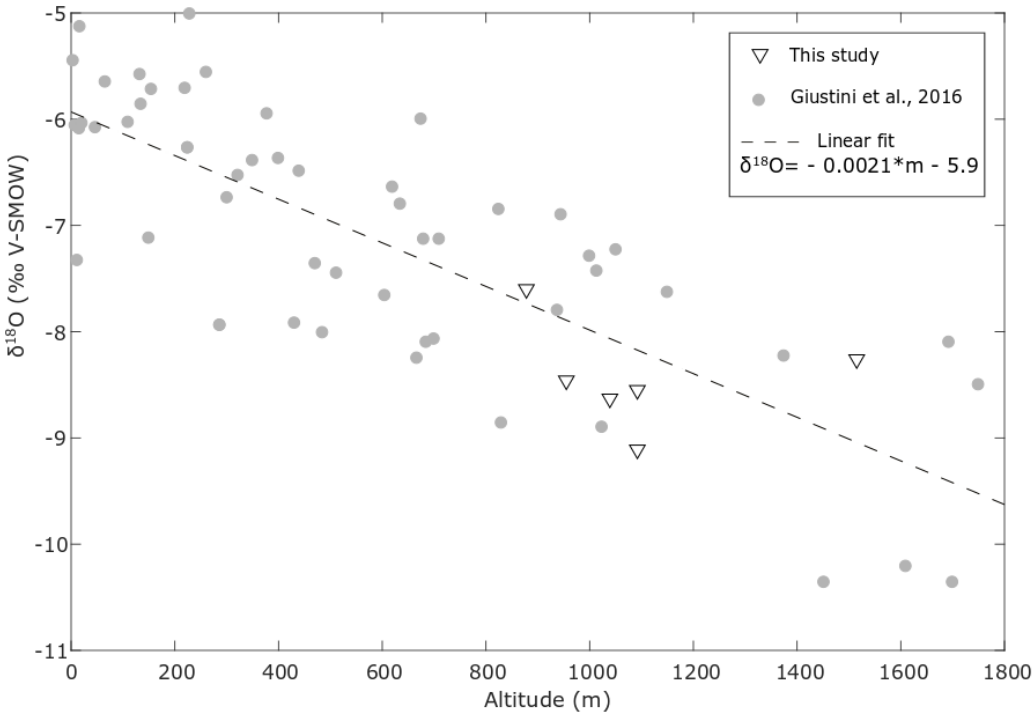

C. FIGURE DR1. *$\delta^{18}O$ gradient with elevation in modern surface water. Triangles indicate stream water measurements from this study, for which the altitude has been corrected for the average hypsometry of the drainage basin. Grey dots indicate rain water measurements from previous studies (compiled in Giustini et al., 2016). The linear fit includes all data. All measurements are reported with respect to V-SMOW (Vienna Standard Mean Ocean Water)*

D. TABLES

Table 1. Surface water $\delta^{18}O$ and δD collected and analyzed in this study. GPS coordinates are given in the WGS84 reference frame. All isotope values are reported relative to V-SMOW (Vienna Standard Mean Ocean Water). Mean hypsometry of the basin is obtained by extracting the catchment area upstream of the sampling location of SRTM DEM using GIS tools.

Sample	$\delta^{18}O$ (‰ ±1s)	$\delta^{2}H$ (‰ ±1s)	Sampling altitude (m)	Mean hypsometry (m)	Longitude (°E)	Latitude (°N)
L1	-7.60 ±0,02	-42.6 ±0,4	498	878	12.7516	42.3761
L2	-8.46 ±0,06	-50.1 ±0.2	381	955	12.8414	42.4899
L3	-8.63 ±0.05	-52.1 ±0.4	780	1039	12.9509	42.6367
L4	-9.11 ±0.08	-55.1 ±0.3	491	1092	13.0811	42.4182
L5	-8.55 ±0.04	-50.3 ±0.3	490	1092	13.0802	42.4196
L6	-8.26 ±0.07	-55.9 ±0.3	714	1515	13.5769	42.2919

Table 2. Results of the isotope analysis for $\delta^{18}O$ and $\delta^{13}C$ in sediments for individual samples of each section. Averages for each section are used for the interpretation and are reported in main text Table 1.

Tuscany – Upper Valdarno basin

ACQ (Acquaborra)

Sample	$\delta^{13}C$	$\delta^{18}O$	Carbonate type
ACQ1w	-10.61	-4.71	Mud
ACQ1g	-10.68	-4.88	Mud
ACQ2w	-10.32	-4.73	Mud
ACQ4a	-13.23	-4.82	Nodule
ACQ4b	-13.20	-4.65	Nodule
ACQ4c	-12.81	-4.09	Micrite
ACQ51	-12.65	-5.67	Nodule
ACQ52	-12.62	-5.35	Nodule
ACQ53	-11.85	-5.11	Nodule
ACQ54	-11.47	-4.97	Nodule
ACQ55	-12.14	-4.88	Nodule
ACQ6bulk	-7.89	-4.66	Mud
ACQ61	-11.94	-4.31	Nodule
ACQ63	-12.22	-4.44	Nodule
ACQ64	-11.96	-4.28	Nodule

FRC (Francalanci)

Sample	$\delta^{13}C$	$\delta^{18}O$	Carbonate type
FRC3	-1.67	-5.14	Nodule
FRC5-1	-10.71	-4.31	Nodule
FRC5-2	-12.84	-5.00	Nodule
FRC5-3	-11.95	-4.35	Nodule
FRC6	-11.95	-4.21	Nodule
FRC6N1	-9.26	-3.64	Nodule
FRC6N2	-5.72	-3.49	Nodule
FRC6N3	-9.25	-3.76	Nodule
FRC6N4	-8.12	-3.94	Nodule
FRC7-1	-9.10	-4.48	Nodule
FRC7-2	-6.36	-4.06	Nodule
FRC7-3	-8.79	-3.97	Nodule
FRC8-1	-4.61	-4.47	Shell
FRC8-2	-7.17	-6.16	Shell
FRC8S1	-9.42	-5.70	Shell (bivalve)
FRC8S2	-8.77	-4.73	Shell (bivalve)
FRC8S3	-6.50	-5.04	Shell (bivalve)
FRC8S4	-8.48	-3.73	Shell (bivalve)
FRC8S5	-7.20	-3.91	Shell (bivalve)
FRC8S6	-7.12	-4.10	Shell (bivalve)
FRC8S7	-5.41	-1.36	Shell (bivalve)
FRC8S8	-6.79	-3.36	Shell (bivalve)
FRC8S9	-5.80	-5.23	Shell (bivalve)
FRC9-1	-9.40	-4.00	Nodule
FRC9-2	-10.38	-3.83	Nodule
FRC9-3	-10.28	-3.93	Nodule

MTC (Montecarlo)

Sample	$\delta^{13}C$	$\delta^{18}O$	Carbonate type
MTC1-1	-3.32	-1.13	Shells (bythinia)
MTC1-2	-4.75	-1.77	Shells
MTC2-1	-4.94	-2.66	Shells
MTC2-2	-4.93	-3.33	Shells
MTC3-1	-4.45	-3.77	Shell (bythinia)
MTC3-2	-8.22	-3.73	Shells (bivalve)
MTC3-3	-5.94	-3.03	Shell gastropod
MTC4-1	-5.88	-2.59	Shell gastropod
MTC4-2	-5.39	-3.96	Shell gastropod
MTC4S1	-7.82	-2.86	Shell (bivalve)
MTC4S2	-6.76	-3.00	Shell (bivalve)
MTC4S3	-6.70	-3.03	Shell (bivalve)
MTC4S4	-6.20	-3.46	Shell (bivalve)
MTC4S5	-6.04	-3.12	Shell (bivalve)
MTC4S6	-5.87	-3.08	Shell (bivalve)
MTC4S7	-6.29	-2.89	Shell (bivalve)
MTC4S8	-6.41	-3.28	Shell (bivalve)
MTC4S9	-5.74	-2.95	Shell (bivalve)
MTC5-1	-6.88	-3.42	Shells
MTC5-2	-6.88	-2.69	Shells
MTC6-1	-6.52	-2.13	Shell (bivalve)
MTC6-2	-5.10	-4.54	Shells
MTC6-3	-4.19	-3.65	Shells
MTC7-1	-6.76	-3.36	Shell (bivalve)
MTC7-2	-6.36	-4.03	Shells
MTC7-3	-6.11	-3.79	Shells
MTC7-4	-7.43	-3.22	Shell (bivalve)
MTC8-1	-7.48	-5.44	Shells
MTC8-2	-5.89	-4.84	Shells
MTC8-3	-6.32	-4.34	Shells

SOL (Solava)

Sample	$\delta^{13}C$	$\delta^{18}O$	Carbonate type
SOL12	-7.32	-5.53	Nodule
SOL13	-8.61	-5.77	Nodule
SOL14	-4.55	-5.66	Nodule
SOL21	-11.43	-3.92	Nodule
SOL22i	-11.11	-4.11	Nodule
SOL23	-1.60	-5.13	Nodule
SOL24	-4.05	-4.40	Nodule
SOL25	-2.30	-4.64	Nodule
SOL26	-4.62	-4.33	Nodule
SOL31	-5.57	-4.70	Nodule
SOL32	-3.47	-4.68	Nodule
SOL41	-5.32	-4.79	Nodule
SOL42	-4.52	-4.71	Nodule
SOL43	-5.25	-4.79	Nodule
SOL44	-5.32	-4.85	Nodule
SOL45	-3.42	-4.60	Nodule
SOL50	-1.59	-5.40	Nodule

SOL51	-1.23	-5.37	Nodule
SOL52	-5.93	-5.74	Nodule
SOL53	-5.15	-5.27	Nodule
SOL54	-3.39	-5.24	Nodule
SOL55	-1.84	-5.45	Nodule
SOL6R1	-11.96	-5.30	Rootcast
SOL6R2	-11.42	-5.20	Rootcast
SOL6R3	-11.93	-5.16	Rootcast
SOL64	-11.46	-5.17	Nodule
SOL65	-11.48	-5.38	Nodule
SOL66	-11.64	-5.21	Nodule
SOL7R1	-11.69	-5.38	Rootcast
SOL7R2	-11.82	-5.17	Rootcast
SOL7R3	-11.84	-5.29	Rootcast
SOL83	-11.18	-4.89	Nodule
SOL84	-11.48	-4.96	Nodule
SOL85	-11.23	-5.18	Nodule

Tuscany – Siena Basin

FRA (Frasta)

Sample	**$\delta^{13}C$**	**$\delta^{18}O$**	**Carbonate type**
FRA1N1	-10.30	-4.23	Nodule
FRA1N2a	-10.39	-4.33	Nodule
FRA1N3	-4.03	-3.52	Nodule
FRA1N4	-4.92	-3.45	Nodule
FRA1N5	-10.49	-4.29	Nodule
FRA2b	-7.25	-6.33	Nodule
FRA2N1	-10.40	-4.57	Nodule
FRA2N1a	-10.58	-4.66	Nodule
FRA2N2	-10.71	-4.59	Nodule
FRA2N3	-10.59	-4.43	Nodule
FRA2N4	-10.38	-4.44	Nodule
FRA2N4a	-10.36	-4.35	Nodule
FRA2N5	-9.92	-4.67	Nodule
FRA2N6	-10.46	-4.41	Nodule

PBL (Poggio Bonelli)

Sample	**$\delta^{13}C$**	**$\delta^{18}O$**	**Carbonate type**
PBL bulk	-9.52	-5.87	Clay
PBL1	-11.58	-5.38	Nodule
PBL2	-11.43	-5.66	Nodule
PBL3	-11.44	-5.49	Nodule
PBL4	-9.68	-6.00	Nodule
PBL5	-11.61	-5.71	Nodule

PNZ (Pienza)

Sample	**$\delta^{13}C$**	**$\delta^{18}O$**	**Carbonate type**
PNZ1	-3.621	-4.084	Nodule
PNZ2	-5.014	-4.451	Nodule

PNZ3	-4.869	-4.914	Nodule
PNZ4	-3.550	-4.639	Nodule

Tuscany – Valdelsa Basin

FNO (Fiano)

Sample	$\delta^{13}C$	$\delta^{18}O$	Carbonate type
FNO1	-10.34	-4.26	Lacustrine
FNO2	-9.24	-4.49	Lacustrine
FNO3	-8.96	-4.24	Lacustrine

Central Apennines – Tiberino Basin

TOP (Topetti)

Sample	$\delta^{13}C$	$\delta^{18}O$	Carbonate type
TOP1	-0.64	-3.838	Clay
TOP2	-0.82	-3.963	Clay
TOP3	-0.82	-3.873	Clay
TOP4	-0.79	-3.841	Clay
TOP5	-0.88	-3.927	Clay
TOP6	-0.61	-3.331	Clay
TOP7	-0.52	-3.041	Clay
TOP8	-1.05	-4.265	Clay
TOP9	-0.92	-3.869	Clay
TOP10	-0.46	-3.629	Clay
TOP12	-0.51	-3.942	Clay
TOP13	-0.49	-3.786	Clay
TOP14	-0.39	-3.355	Clay
TOP15	-0.56	-3.843	Clay
TOP16	-0.42	-3.628	Clay
TOP18	-0.715	-3.545	Clay
TOP19	-0.605	-3.434	Clay
TOP20	-0.478	-3.217	Clay
TOP21	-0.748	-3.465	Clay
TOP22	-0.571	-3.497	Clay
TOP23	-0.668	-3.476	Clay
TOP24	-0.400	-2.977	Clay
TOP25	-0.401	-3.135	Clay
TOP26	-0.320	-2.946	Clay
TOP27	-0.430	-3.314	Clay
TOP28	-0.717	-3.500	Clay
TOP29	-0.791	-3.622	Clay
TOP30	-0.530	-3.790	Clay
TOP31	-1.140	-3.820	Clay
TOP32	-0.960	-3.550	Clay
TOP33	-1.210	-3.960	Clay
TOP34	-1.020	-3.540	Clay
TOP35	-1.040	-3.780	Clay
TOP36	-0.930	-3.640	Clay
TOP40	-0.540	-3.310	Clay
TOP51	-1.180	-3.490	Clay

TOP52	-0.920	-3.330	Clay
TOP53	-0.950	-3.050	Clay
TOP54	-1.090	-3.430	Clay

UPN (Ponte Naja)

Sample	$\delta^{13}C$	$\delta^{18}O$	Carbonate type
TOP86	-1.040	-3.930	Clay
UPN106	-2.650	-4.284	Clay
UPN78	-2.669	-4.497	Clay
UPN60	-2.420	-4.440	Clay

Central Apennines – Rieti Basin

ROB (Rieti Ornaro Basso)

Sample	$\delta^{13}C$	$\delta^{18}O$	Carbonate type
ROB1	1.801	-2.620	Lacustrine
ROB2	1.823	-2.688	Lacustrine
ROB3	1.897	-3.101	Lacustrine
ROB4	1.667	-2.254	Lacustrine
ROB5	1.851	-2.637	Lacustrine
ROB6	1.813	-2.201	Lacustrine
ROB7	1.742	-2.188	Lacustrine
ROB8	1.746	-1.976	Lacustrine
ROB9	1.572	-2.107	Clay
ROB10	1.225	-2.473	Clay
ROB11	1.131	-2.521	Clay
ROB12	1.583	-2.159	Clay
ROB13	1.324	-2.234	Lacustrine
ROB14	0.540	-2.795	Concretion
ROB15	-1.191	-2.887	Concretion

LEO (Leonessa)

Sample	$\delta^{13}C$	$\delta^{18}O$	Carbonate type
LEO20B	-1.454	-8.931	Clay
LEO20S0	-1.873	-5.675	Shells
LEO20S1	-1.748	-5.999	Shell (Bythinia)
LEO20S2	-3.618	-6.207	Shell (Bythinia)
LEO20S3	1.184	-5.445	Shell (Bythinia)
LEO20S4	-4.835	-5.396	Shell (Bythinia)
LEO20S5	-4.29	-7.171	Shell (Bythinia)
LEO21S0	-1.507	-5.664	Shells
LEO21S2	-2.478	-5.802	Shell (Bythinia)
LEO21S3	-3.047	-5.937	Shell (Bythinia)
LEO21S4	-1.266	-5.421	Shell (Bythinia)
LEO21S5	-4.25	-5.5	Shell (Bythinia)
LEO21SX2	-3.049	-6.228	Shells
LEO22S0	-0.384	-7.143	Shells
LEO22S1	-1.118	-6.821	Shell (Bythinia)
LEO22S2	-1.701	-8.064	Shell (Bythinia)
LEO22S3	-1.501	-7.789	Shell (Bythinia)

LEO22S4	-1.159	-6.719	Shell (Bythinia)
LEO22S5	-0.966	-6.64	Shell (Bythinia)
LEO22SX	-0.653	-6.792	Shells
LEO23	-2.419	-8.718	Clay
LEO24	-2.174	-9.997	Clay
LEO25	-0.909	-9.795	Clay
LEO19b	-1.279	-8.252	Clay, mud
LEO19S	-0.914	-8.425	Shell
LEO16	-1.902	-6.905	Clay

Central Apennines – L'Aquila Basin

FAC (Faccione)

Sample	$\delta^{13}C$	$\delta^{18}O$	Carbonate type
F21	-1.29	-6.31	Lacustrine
F24	-0.63	-5.27	Lacustrine
F25	-0.62	-5.26	Lacustrine
F27	-1.30	-6.37	Lacustrine
F29	-0.77	-5.77	Lacustrine
F211	-1.03	-6.56	Lacustrine
F213	-1.21	-6.57	Lacustrine
F215	-1.05	-6.17	Lacustrine
F216	-1.26	-6.37	Lacustrine
F217b	-1.22	-6.16	Lacustrine
F219	-0.522	-4.25	Lacustrine
F222	-1.363	-6.55	Lacustrine
F230	-0.461	-6.23	Lacustrine
F232	-1.320	-6.42	Lacustrine
SN41	-1.992	-4.19	Lacustrine
SN42	-1.039	-5.21	Lacustrine
SN43	-0.898	-6.29	Lacustrine
SN44	-1.009	-6.44	Lacustrine
SN45	-0.654	-6.06	Lacustrine
SN46bis	-0.887	-6.53	Lacustrine
SN47	-0.781	-6.44	Lacustrine
LS291	-0.680	-4.39	Lacustrine
LS293	-1.456	-6.11	Lacustrine
LS295	-0.766	-6.36	Lacustrine
LS281	-1.473	-5.36	Lacustrine
LS302	-1.762	-5.66	Clay

AQU (L'Aquila)

Sample	$\delta^{13}C$	$\delta^{18}O$	Carbonate type
AQU26	-9.63	-5.35	Concretion
AQU28	-0.40	-1.71	Clay, mud
AQU27W	-8.19	-6.60	Concretion
AQU27Y	-2.24	-2.76	Concretion
AQU29	-3.66	-3.71	Nodule
AQU30	-4.72	-6.95	Lacustrine
AQU31	-3.64	-6.83	Lacustrine
AQU35	-2.75	-4.27	Concretion
AQU34	-1.83	-2.90	Clay, mud
AQU33	-1.94	-3.47	Concretion

AQU32	-1.00	-1.35	Clay, mud

Central Apennines – Fucino Basin

FUC1 (Fucino)

Sample	$\delta^{13}C$	$\delta^{18}O$	Carbonate type
FUC1-1	-8.16	-5.98	Nodule
FUC1-2	-8.16	-6.00	Nodule
FUC1-3	-7.02	-6.52	Nodule
FUC2red	-8.02	-6.67	Nodule
FUC2white	-7.05	-6.00	Nodule

E. DISCUSSION ON DATA VARIABILITY

Stable isotope data in natural and complex environments like lacustrine intramontane basins can be compromised by the influence of various parameters, that we can more or less (rather more, luckily) take into account, or even quantify.

Evaporation

Evaporation is a process subject to isotopic fractionation, as the lighter ^{16}O isotope will preferentially end up as a gas, and the heavier ^{18}O remain in the liquid. Although this process is continuous in any natural water body exchanging with the atmosphere, it can usually be neglected for exorheic basins, or more generally basins where the inflowing rainwater is balanced by an equivalent amount of outflow (into a river or the ground). On the contrary, evaporation is the major process of water loss in closed basins, meaning that the evaporatively enriched water will accumulate in the basin without flowing out. Carbonates forming in this setting will thus reflect this ^{18}O enrichment, rather than the original composition of precipitation water. To identify basins that might have been affected by evaporative conditions, we rely, when available, on geomorphological evidence (case of the Fucino Basin; FUC), or otherwise on the corresponding $\delta^{13}C$ measurements from the samples (ROB samples). Indeed, in evaporative settings, C isotopes undergo a similar fractionation process, where the water degasses preferentially ^{12}C. As a result, $\delta^{13}C$ and $\delta^{18}O$ covary in evaporatively enriched samples (Talbot and Kelts, 1990). The ROB samples yield high values of $\delta^{18}O$, but are also enriched in ^{13}C, which makes them likely to be influenced by evaporation. PBL on the other hand only shows a low ^{18}O, while ^{13}C is in the usual range of our samples (Fig DR2)

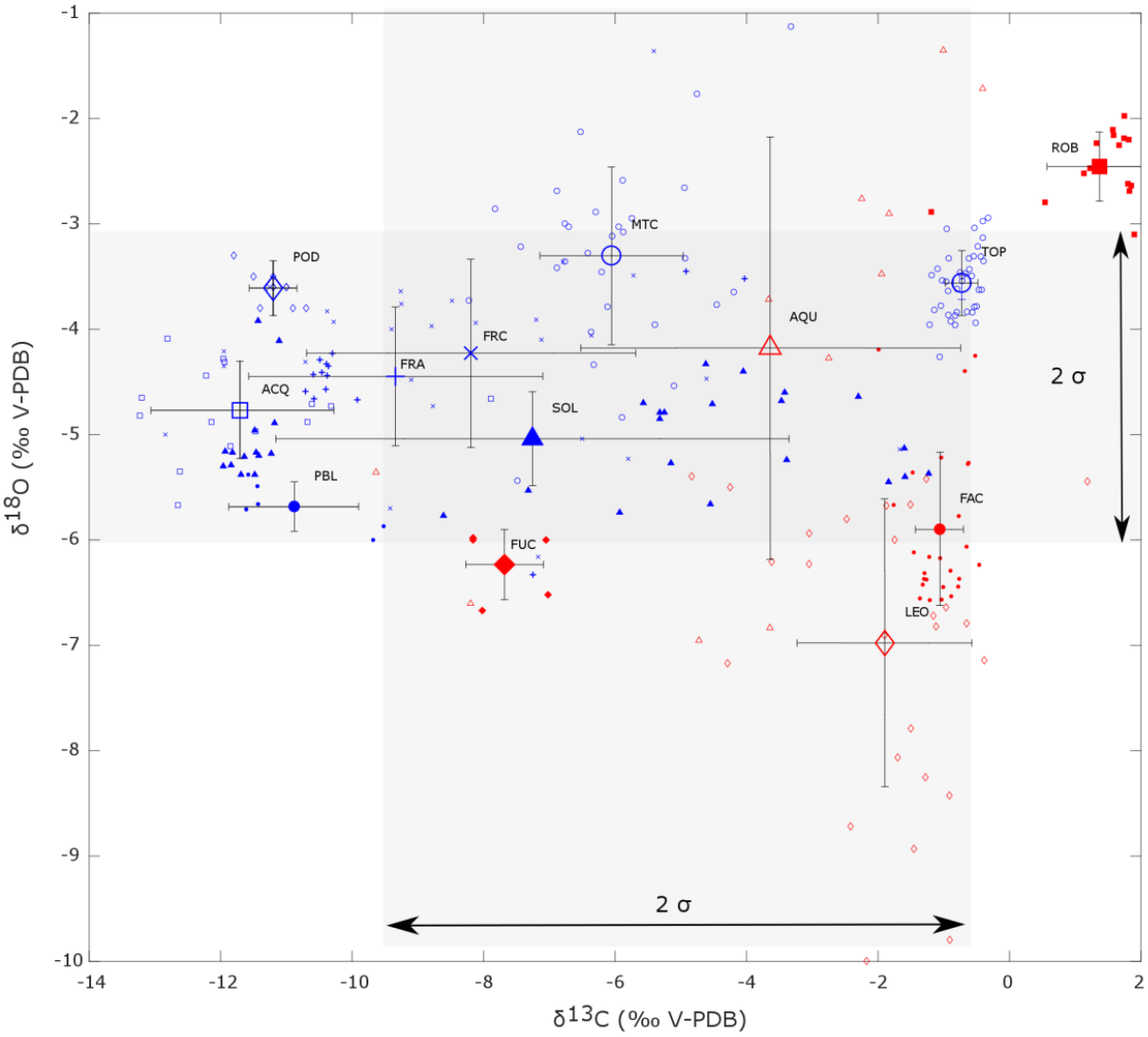

Figure DR2. δ18O and δ13C measurements of the samples for which δ13C data is available. Mean values for each sample are indicated by a bigger symbol with standard deviation bars and sample name. Individual data points constituting each sample are represented by smaller symbols of the same shape. Blue and red colours indicate lowland and highland samples, respectively. The grey areas represent the standard deviation around the mean value for all individual data points of the entire dataset.

Seasonal variability

In environments with important seasonal shifts in moisture, authigenic carbonates record variable isotopic compositions, depending on moisture provenance and/or temperature at the time of their formation (e.g. Bougeois et al., 2014). Since the Miocene, the Italian peninsula is located in a Mediterranean climate zone, which is characterized by dry summers and wet winters, receiving almost all their annual precipitation during the winter months. Temperatures

are usually warm during summer and mild during winter. We assess the influence of seasonal variability by analysing isotopic composition of the successive growth increments of carbonatic fossil shells (Fig DR4). We selected shells of big bivalves, that were found in living position in the MTC and FRC sections. Bivalves grow by progressive thickening of their shell, simultaneously from the outside towards the inside, and away from the hinge. Each growth increment is represented by a distinctive layer of calcium carbonate. Dark and thin layers form during winter, and alternate with thicker, lighter layers formed during summer (Kirby, 2000). We sampled a high resolution $\delta^{18}O$ profile perpendicular to the growth strata in a part of the shell where the layers were best defined, in order to allow a macroscopic separation. The resulting $\delta^{18}O$ variability between the layers is small, and shows no cyclicity. This allows us to rule out any strong seasonality signal during the life-time of those shells.

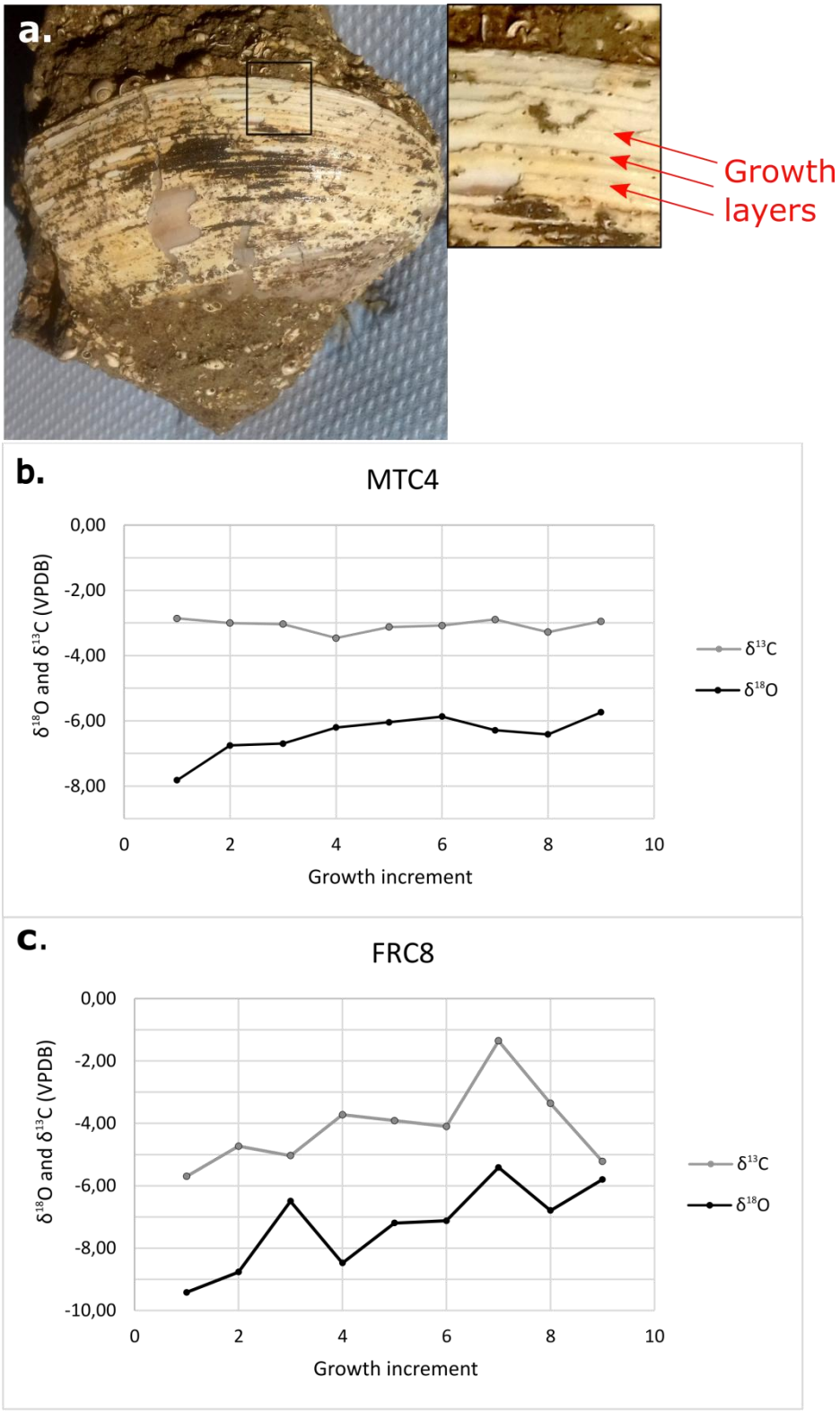

Figure DR4. a. Picture of a shell from sample MTC 6, similar to samples MTC4 and FRC8. b. and c. $\delta^{18}O$ and $\delta^{13}C$ results for two different freshwater bivalve shells. Growth increments are numbered starting from the hinge. No alternating fluctuations appear in the signal.

Glacial-interglacial cycles

The central Apennines show evidence of glaciers extending down to 1500 m AMSL during the LGM (Giaccio et al., 2012), and strong glacial-interglacial cycles are generally thought to have initiated later than 0.8 Ma, thus most of our samples are not affected. During glacial stages, lower temperatures as well as water supply from glacial melting may have influenced the isotopic records. We are not able to date most of our samples within the glacial cycle due to age uncertainties. However, we use high-resolution core records from Giaccio et al. and Regattieri et al. in the Sulmona basin that span from MIS5 to MIS19, to assess the potential influence of glacial-interglacial cycles on ^{18}O records. SUL1 integrates data from both glacial stage MIS12 (n=115) and interglacial stage MIS11 (n=200). Mean $d^{18}O$ values for those 2 stages are within error of each other (-8 ‰ and -9 ‰ respectively (Fig DR3; Regattieri et al., 2016; 2017)). We suppose that sediment mixing and precipitation water supply in the lacustrine basin were sufficient to dampen strong glacial-interglacial signals.

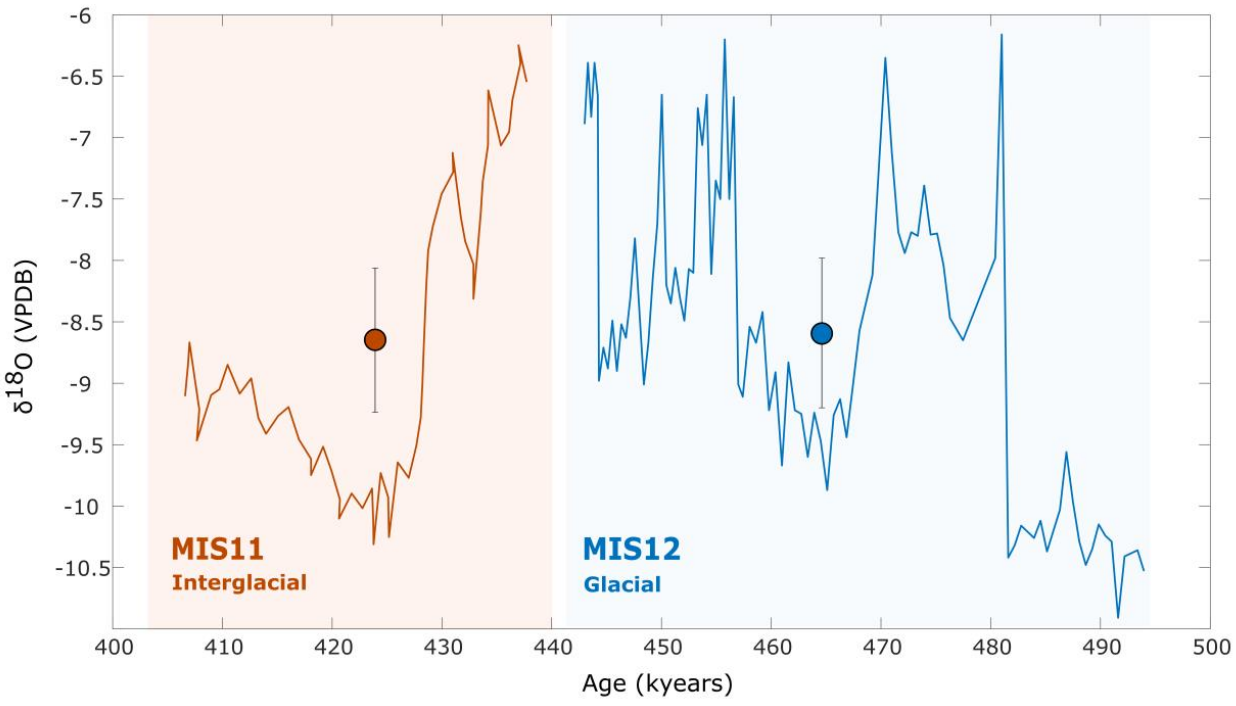

Figure DR3. Isotope results after Regattieri et al., 2016 and 2017 for an entire glacial-interglacial cycle. Solid lines indicate high resolution $\delta^{18}O$ records (red: MIS11; blue: MIS12). Red and blue dots represent average $\delta^{18}O$ + standard deviation over the corresponding stage.

Post-deposit alteration: diagenesis, hydrothermalism, surface water

The syn-sedimentary isotopic signal may be overprinted by post-deposit fluid circulation. In that case, hydrothermal or later surface water will dissolve authigenic carbonates and recrystallize secondary carbonates instead, which are not representative of the isotopic composition at time of deposition (Garzione et al., 2004). We avoided outcrops located nearby known hydrothermal areas or fault zones, and none of our samples has evidence of alteration such as veins or weathering aureoles. In case of significant alteration, we would expect the variability in $\delta^{18}O$ among replicates of a sample to show important scatter or a gradual trend: radially inside nodules, and vertically inside a section. There is no evidence for such trends, or alteration marks in our samples.

Furthermore, we know from stratigraphy that our samples were not buried more than a few hundred meters (typically 50-200 m), suggesting the sediments have not been affected by diagenesis (little compaction and cementation, no temperature increase).

Upwind/downwind side and moisture recycling

Most of the precipitation received in the highest parts of the Central Apennines comes with the dominant wind from the Thyrenean sea. As the moisture gets gradually depleted in ^{18}O while migrating inlands, we expect precipitation on the Adriatic side of the drainage divide to be slightly more depleted in ^{18}O than the western basins. The isotopic lapse-rate is thus steeper on the downwind side. We attribute the slightly lower $\delta^{18}O$ values of the Sulmona basin compared to basins of equivalent modern elevation on the upwind side of the range to the fact that it is located on the downwind side of the dominating moisture path.

An additional effect might come from the complex topographic shape of the Apennines chain. Instead of the ideal pyramid shape, it is made of a succession of lower basins between elevated ridges, which get increasingly higher towards the inlands. If at first order, orographic rainout compares well with long wavelength elevation, at basin scale, the isotopic composition of surface water might be influenced by local aerology. Indeed, recycling of moisture within the continent can mix the original signal of oceanic-sourced precipitation with moisture evaporating from inland basins. This complication is more likely for basins like Sulmona,

which is separated from the Thyrrenean coast by the extensive Fucino basin, which was a closed and highly evaporative basin.

Detrital material

Lacustrine and fluvial sediments may contain variable amounts of detrital material from the surrounding catchment area. In the case of the Apennines, the bedrock is formed by a thick limestone succession, which originated from the accretion of the Meso-Cenozoic carbonate platform and margin into the fold and thrust belt. Although most lacustrine sediments show a typical facies of biochemical sediments (e.g. mudstone from calcium precipitate and carbonate micro-shells), marine limestone pebbles from several fluvial deposits (Rieti Basso, Fucino) confirm that detrital material has reached the basins. As the isotopic composition of marine carbonates does not reflect the composition of Pliocene surface water, we tried to avoid any detrital clasts during sample preparation. We meticulously separated interstitial sparitic cement, clean fresh-water shells, and characteristic fine lacustrine material. Besides, basement carbonates have much higher $\delta^{18}O$ values (up to 30 ‰ in the calcare Massiccio (Billi et al, 2007) and around -1.5 ‰ in marine fossils from PBL) than the continental deposits, therefore any contamination would have shifted our values significantly.

F. DATA REPOSITORY REFERENCES

Aldinucci, M., Benvenuti, M., Andreetta, A., Dominici, S., Foresi, L.M., Carnicelli, S., and Martini, I., 2019, Composite sequence stratigraphic patterns in alluvial to shallow-marine successions: Examples from the Piacenzian of the Valdelsa Basin (Central Italy): Sedimentary Geology, v. 388, p. 99–113, doi:10.1016/j.sedgeo.2019.05.005.

Bally, A.W., Burbi, L., Cooper, C., and Ghelardoni, R., 1986, Balanced sections and seismic reflection profiles across the central Apennines: Memorie della Società Geologica Italiana, v. 35, p. 257–310.

Basilici, G., 1997, Sedimentary facies in an extensional and deep-lacustrine depositional system: The Pliocene Tiberino Basin, Central Italy: Sedimentary Geology, v. 109, p. 73–94, doi:10.1016/S0037-0738(96)00056-5.

Bertini, A., Magi, M., Mazza, P.P.A., and Fauquette, S., 2010, Impact of short-term climatic events on latest Pliocene land settings and communities in Central Italy (Upper Valdarno basin): Quaternary International, v. 225, p. 92–105, doi:10.1016/j.quaint.2009.05.011.

Bigi, S., Conti, A., Casero, P., Ruggiero, L., Recanati, R., and Lipparini, L., 2013, Geological model of the central Periadriatic basin (Apennines, Italy): Marine and Petroleum Geology, v. 42, p. 107–121, doi:10.1016/j.marpetgeo.2012.07.005.

Bougeois, L., de Rafélis, M., Reichart, G.J., de Nooijer, L.J., Nicollin, F., and Dupont-Nivet, G., 2014, A high resolution study of trace elements and stable isotopes in oyster shells to estimate central asian middle eocene seasonality: Chemical Geology, v. 363, p. 200–212,

doi:10.1016/j.chemgeo.2013.10.037.

Breitenbach, S.F.M., and Bernasconi, S.M., 2011, Carbon and oxygen isotope analysis of small carbonate samples (20 to 100 μg) with a GasBench II preparation device: Rapid Communications in Mass Spectrometry, v. 25, p. 1910–1914, doi:10.1002/rcm.5052.

Casero, P., 2004, Structural setting of petroleum exploration plays in Italy: Special Volume of the Italian Geological Society for the IGC 32, v. 107, p. 319–322.

Cavinato, G.P., Carusi, C., Dall'asta, M., Miccadei, E., and Piacentini, T., 2002, Sedimentary and tectonic evolution of Plio-Pleistocene alluvial and lacustrine deposits of Fucino Basin (central Italy): Sedimentary Geology, v. 148, p. 29–59, doi:10.1016/S0037-0738(01)00209-3.

Cavinato, G.P., Cosentino, D., Funiciello, R., Parotto, M., Salvini, F., and Tozzi, M., 1994, Constraints and new problems for geodynamical modelling of central Italy (CROP11 Civitavecchia - Vasto deep seismic line): Bolletino di Geofisica Teorica ed Applicata, v. 36, p. 141–144.

Cerling, T.E., and Quade, J., 1993, Stable Carbon and Oxygen Isotopes in Soil Carbonates: 217–231 p., doi:10.1029/GM078p0217.

Chiarabba, C., De Gori, P., and Mele, F.M., 2015, Recent seismicity of Italy: Active tectonics of the central Mediterranean region and seismicity rate changes after the Mw 6.3 L'Aquila earthquake: Tectonophysics, v. 638, p. 82–93, doi:10.1016/j.tecto.2014.10.016.

Cosentino, D. et al., 2017, New insights into the onset and evolution of the central Apennine extensional intermontane basins based on the tectonically active L'Aquila Basin (central Italy): Bulletin of the Geological Society of America, v. 129, p. 1314–1336, doi:10.1130/B31679.1.

Cosentino, D. et al., 2008, Note Illustrative della carta geologica d'Italia alla scala 1:50.000 Foglio 357 Cittaducale:

D'Agostino, N., Jackson, J.A., Dramis, F., and Funiciello, R., 2001, Interactions between mantle upwelling, drainage evolution and active normal faulting: An example from the Central Appennines (Italy): Geophysical Journal International, v. 147, p. 475–497, doi:10.1046/j.1365-246X.2001.00539.x.

Duretz, T., Gerya, T. V., and May, D.A., 2011, Numerical modelling of spontaneous slab breakoff and subsequent topographic response: Tectonophysics, v. 502, p. 244–256, doi:10.1016/j.tecto.2010.05.024.

Faccenna, C., Becker, T.W., Miller, M.S., Serpelloni, E., and Willett, S.D., 2014, Isostasy, dynamic topography, and the elevation of the Apennines of Italy: Earth and Planetary Science Letters, v. 407, p. 163–174, doi:10.1016/j.epsl.2014.09.027.

Faure Walker, J.P., Roberts, G.P., Cowie, P.A., Papanikolaou, I., Michetti, A.M., Sammonds, P., Wilkinson, M., McCaffrey, K.J.W., and Phillips, R.J., 2012, Relationship between topography, rates of extension and mantle dynamics in the actively-extending Italian Apennines: Earth and Planetary Science Letters, v. 325–326, p. 76–84, doi:10.1016/j.epsl.2012.01.028.

Fidolini, F., Ghinassi, M., Magi, M., Papini, M., and Sagri, M., 2013, The plio-pleistocene fluvio-lacustrine upper valdarno basin (central Italy): Stratigraphy and Basin fill evolution: Italian Journal of Geosciences, v. 132, p. 13–32, doi:10.3301/IJG.2012.06.

Fubelli, G., Falcucci, E., Mei, A., and Dramis, F., 2008, Evoluzione Quaternaria Del Bacino Di Leonessa (Rieti): Il Quaternario, v. 21(2), p. 457–468.

Fubelli, G., Della Seta, M., and Amato, G., 2014, Drainage system adjustment in response to the opening of the Rieti intermontane basin (Central Italy): geostatistical reconstruction of the PaleoFarfa River alluvial plain: Rendiconti Lincei, v. 25, p. 167–176, doi:10.1007/s12210-014-0322-0.

Galadini, F., Messina, P., Giaccio, B., and Sposato, A., 2003, Early uplift history of the Abruzzi Apennines (central Italy): Available geomorphological constraints: Quaternary International, v. 101, p. 125–135, doi:10.1016/S1040-6182(02)00095-2.

Ghinassi, M., Abbazzi, L., Esu, D., Gaudant, J., and Girotti, O., 2005, Facies analysis, stratigraphy and palaeontology (Molluscs and Vertebrates) in the Upper Pliocene sandy flood-basin deposits

of the Upper Valdarno Basin (Northern Apennines): Rivista Italiana di Paleontologia e Stratigrafia, v. 111, p. 467–487.

Ghinassi, M., Fidolini, F., Magi, M., and Sagri, M., 2013, Depositional environments of the plio-pleistocene upper Valdarno Basin (Tuscany, Italy): Italian Journal of Geosciences, v. 132, p. 33–53, doi:10.3301/IJG.2012.07.

Giaccio, B. et al., 2015, A key continental archive for the last 2Ma of climatic history of the central Mediterranean region: A pilot drilling in the Fucino Basin, central Italy: Scientific Drilling, v. 20, p. 13–19, doi:10.5194/sd-20-13-2015.

Giustini, F., Brilli, M., and Patera, A., 2016, Mapping oxygen stable isotopes of precipitation in Italy: Journal of Hydrology: Regional Studies, v. 8, p. 162–181, doi:10.1016/j.ejrh.2016.04.001.

Hoke, G.D., Liu-Zeng, J., Hren, M.T., Wissink, G.K., and Garzione, C.N., 2014, Stable isotopes reveal high southeast Tibetan Plateau margin since the Paleogene: Earth and Planetary Science Letters, v. 394, p. 270–278, doi:10.1016/j.epsl.2014.03.007.

van Hunen, J., and Allen, M.B., 2011, Continental collision and slab break-off: A comparison of 3-D numerical models with observations: Earth and Planetary Science Letters, v. 302, p. 27–37, doi:10.1016/j.epsl.2010.11.035.

Kirby, M.X., 2000, Paleoecological Differences between Tertiary and Quaternary Crassostrea Oysters, as Revealed by Stable Isotope Sclerochronology: Palaios, v. 15, p. 132, doi:10.2307/3515499.

Lisiecki, L.E., and Raymo, M.E., 2005, A Pliocene-Pleistocene stack of 57 globally distributed benthic δ 18 O records: Paleoceanography, v. 20, p. 1–17, doi:10.1029/2004PA001071.

Longinelli, A., and Selmo, E., 2003, Isotopic composition of precipitation in Italy: a first overall map: Journal of Hydrology, v. 270, p. 75–88.

Mancini, M., D'Anastasio, E., Barbieri, M., and De Martini, P.M., 2007, Geomorphological, paleontological and87Sr/86Sr isotope analyses of early Pleistocene paleoshorelines to define the uplift of Central Apennines (Italy): Quaternary Research, v. 67, p. 487–501, doi:10.1016/j.yqres.2007.01.005.

Martini, I., and Aldinucci, M., 2017, Sedimentation and Basin-Fill History of the Pliocene Succession Exposed in the Northern Siena-Radicofani Basin (Tuscany, Italy): a Sequence-Stratigraphic Approach: Riv. It. Paleontol. Strat, v. 123, p. 407–432, https://www.researchgate.net/profile/Ivan_Martini/publication/319353769_Sedimentation_and_basin-fill_history_of_the_pliocene_succession_exposed_in_the_Northern_Siena-Radicofani_Basin_Tuscany_Italy_A_sequence-stratigraphic_approach/links/59a6c3e80f7e9b41b7.

Martini, I., Aldinucci, M., Foresi, L.M., Mazzei, R., and Sandrelli, F., 2011, Geological map of the Pliocene succession of the Northern Siena Basin (Tuscany, Italy): Journal of Maps, v. 7, p. 193–205, doi:10.4113/jom.2011.1176.

Martini, I.P., and Sagri, M., 1993, Tectono-sedimentary characteristics of Late Miocene-Quaternary extensional basins of the Northern Apennines, Italy: Earth Science Reviews, v. 34, p. 197–233, doi:10.1016/0012-8252(93)90034-5.

Nocentini, M., Asti, R., Cosentino, D., Durantec, F., Gliozzi, E., Macerola, L., and Tallini, M., 2017, Plio-quaternary geology of L'Aquila-Scoppito basin (Central Italy): Journal of Maps, v. 13, p. 563–574, doi:10.1080/17445647.2017.1340910.

Patacca, E., Sartori, R., and Scandone, P., 1990, Tyrrhenian basin and Apenninic Arcs: kinematic relations since Late Tortonian times.: Mem. Soc. Geol. It, v. 45, p. 425–451, doi:10.1007/978-94-011-2016-6_7.

Pizzi, A., 2003, Plio-Quaternary uplift rates in the outer zone of the central Apennines fold-and-thrust belt, Italy: Quaternary International, v. 101–102, p. 229–237, doi:10.1016/S1040-6182(02)00105-2.

Poage, M.A., and Chamberlain, C.P., 2001, Stable isotope composition of precipitation and surface waters: considerations for studies of paleoelevation change: American Journal of Science, v.

301, p. 1–15, http://www.ajsonline.org/content/301/1/1.full.pdf.

Poulsen, C.J., and Jeffery, M.L., 2011, Climate change imprinting on stable isotopic compositions of high-elevation meteoric water cloaks past surface elevations of major orogens: Geology, v. 39, p. 595–598, doi:10.1130/G32052.1.

Regattieri, E. et al., 2017, A Last Interglacial record of environmental changes from the Sulmona Basin (central Italy): Palaeogeography, Palaeoclimatology, Palaeoecology, v. 472, p. 51–66, doi:10.1016/j.palaeo.2017.02.013.

Regattieri, E. et al., 2019, Frequency and dynamics of millennial-scale variability during Marine Isotope Stage 19: Insights from the Sulmona Basin (central Italy): Quaternary Science Reviews, v. 214, p. 28–43, doi:10.1016/j.quascirev.2019.04.024.

Regattieri, E., Giaccio, B., Galli, P., Nomade, S., Peronace, E., Messina, P., Sposato, A., Boschi, C., and Gemelli, M., 2016, A multi-proxy record of MIS 11-12 deglaciation and glacial MIS 12 instability from the Sulmona basin (central Italy): Quaternary Science Reviews, v. 132, p. 129–145, doi:10.1016/j.quascirev.2015.11.015.

Rowley, D.B., and Garzione, C.N., 2007, Stable Isotope-Based Paleoaltimetry: Annual Review of Earth and Planetary Sciences, v. 35, p. 463–508, doi:10.1146/annurev.earth.35.031306.140155.

Royden, L., and Faccenna, C., 2018, Subduction Orogeny and the Late Cenozoic Evolution of the Mediterranean Arcs: Annual Review of Earth and Planetary Sciences, v. 46, p. 261–289, doi:10.1146/annurev-earth-060115-012419.

Royden, L., Patacca, E., and Scandone, P., 1987, Segmentation and configuration of subducted lithosphere in Italy: an important control on thrust-belt and foredeep-basin evolution.: Geology, v. 15, p. 714–717, doi:10.1130/0091-7613(1987)15<714:SACOSL>2.0.CO;2.

Serpelloni, E., Faccenna, C., Spada, G., Dong, D., and Williams, S.D.P., 2013, Vertical GPS ground motion rates in the Euro-Mediterranean region: New evidence of velocity gradients at different spatial scales along the Nubia-Eurasia plate boundary: Journal of Geophysical Research: Solid Earth, v. 118, p. 6003–6024, doi:10.1002/2013JB010102.

Spadi, M., 2018, Ostracod Assemblages From the Palaeolake Tiberino (Piacenzian-Gelasian , Central Italy): a Synthesis: v. 31, p. 193–197.

Spadi, M., Gliozzi, E., Cosentino, D., and Nocentini, M., 2016, Late Piacenzian–Gelasian freshwater ostracods (Crustacea) from the L'Aquila Basin (central Apennines, Italy): Journal of Systematic Palaeontology, v. 14, p. 617–642, doi:10.1080/14772019.2015.1079561.

Spadi, M., Gliozzi, E., and Medici, M.C., 2017, A Plio–Pleistocene Caspiocypris species flock (Candoninae, Ostracoda) from the Palaeolake Tiberino (Umbria, central Italy): Journal of Systematic Palaeontology, v. 2019, p. 1–18, doi:10.1080/14772019.2017.1310143.

Talbot, M.R., 1990, A review of the palaeohydrological interpretation of carbon and oxygen isotopic composition: Chemical Geology, v. 80, p. 261–279.

Wortel, M.J.R., and Spakman, W., 2000, Subduction and slab detachment in the Mediterranean-Carpathian region: Science, v. 290, p. 1910–1917, doi:10.1126/science.290.5498.1910.

Zarlenga, F., 1987, I depositi continentali del bacino del Fucino (L'aquila, Italia centrale): Geologica Romana, v. 26, p. 223–253.

Zhong, S., and Gurnis, M., 1994, Controls on trench topography from dynamic models of subducted slabs: Journal of Geophysical Research, v. 99, p. 15683, doi:10.1029/94JB00809.

Part 2

Neogene exhumation pattern of the central Apennines (Italy) constrained by low-temperature thermochronology

Malwina San Jose[1,2], Maria Giuditta Fellin[2], Domenico Cosentino[1], Claudio Faccenna[1,3]

[1] Dipartimento di Scienze, Università degli Studi Roma Tre, Largo S. L. Murialdo, 1, 00146 Roma, Italy

[2]Department of Earth Sciences, ETH Zürich, Sonneggstrasse 5 8092 Zürich, Switzerland

[3]Jackson School of Geosciences, University of Texas at Austin, US

ABSTRACT

The topography of mountain belts results from interactions between surface processes, lithospheric thickening, and mantle dynamics. The Apennines (Italy) provide a study area where all of these processes are at play. The central part of the Apennines is an orogenic wedge formed by the westward subducting Adriatic microplate during the Neogene. It underwent post-orogenic extension, and overlies an area of local slab detachment.

By reconstructing the exhumation pattern of the orogen, we aim at linking thrusting, normal faulting, and mantle dynamics to local uplift events. We present a set of 25 new (U-Th)/He and 10 fission Track cooling ages on apatites sampled from widespread syn-orogenic flysch basin deposits, including one high-resolution vertical profile. Mean cooling ages range from Early Pleistocene to mid Tortonian. We rely on thermal modelling to interpret samples yielding partially reset He ages due to insufficient burial depth. The spatial distribution of the ages suggests an early uplift of the Tyrrhenian coast between ~5 and ~8 Ma linked to the onset of back-arc extension. Samples from different tectonic units of the accretionary wedge show cooling ages coeval with the orogenic transport of the unit, suggesting that their exhumation was caused by crustal thickening. However, nine AHe samples across the Central-Eastern part of the area show recent cooling ages between 3 and 1 Ma, with exhumation rates higher than 0.6 km/Ma. This signal is locally related to the deep exhumation of the footwall of the Gorzano fault, but also appears consistently throughout areas with little evidence of normal faulting. We interpret this rapid, large scale wave of exhumation as a possible effect of dynamic topography related to the Pliocene opening of the Adriatic slab window.

1. INTRODUCTION

The Apennines, a low-elevation but high relief mountain range, originated as a Neogene fold-and-thrust belt during the West-verging subduction of the Adria micro-plate (Patacca et al., 1990). Meso-Cenozoic sedimentary series were stacked and emerged in the process (Bally et al., 1986), forming the present topography, which culminates in the Central Apennines at almost 3000 m ASL. In this region, carbonate rocks typify the landscape together with a series of subduction front-parallel intramontane basins and ranges which today are deeply incised by outward draining river networks (Fig. 1). The use of thermochronometric methods to quantify exhumation is here limited by the type of bedrock exposed and consequently, it is difficult to identify temporal links between topography building and corresponding geodynamic events.

Due to the complex geodynamic history of the area, many contributions to surface uplift are likely. Pre-orogenic paleotopography and crustal thickening during compression have substantially influenced the morphology of the chain (Cosentino et al., 2010 and references therein), which was then overprinted by post-orogenic extension due to slab roll-back (Cavinato and Decelles, 1999). This normal faulting phase, starting in the mid Miocene, is responsible for local relief building as well as redistribution of topographic loads, and has likely influenced regional exhumation patterns. With the cessation of compression at the subduction front around 2.5-1.8 Ma (Pizzi, 2003; Bigi et al., 2013), the chain enters a different geodynamic phase. Recent studies indicate anomalously high uplift rates in this area (Faccenna et al., 2014), as well as a simultaneous onset of post-orogenic extension at ~2 Ma (Cosentino et al., 2017). Those observations lead to the hypothesis that up to 400 m of the central Apennine topography is dynamically sustained by mantle flow (e.g. Faure Walker et al., 2012; Faccenna et al., 2014).

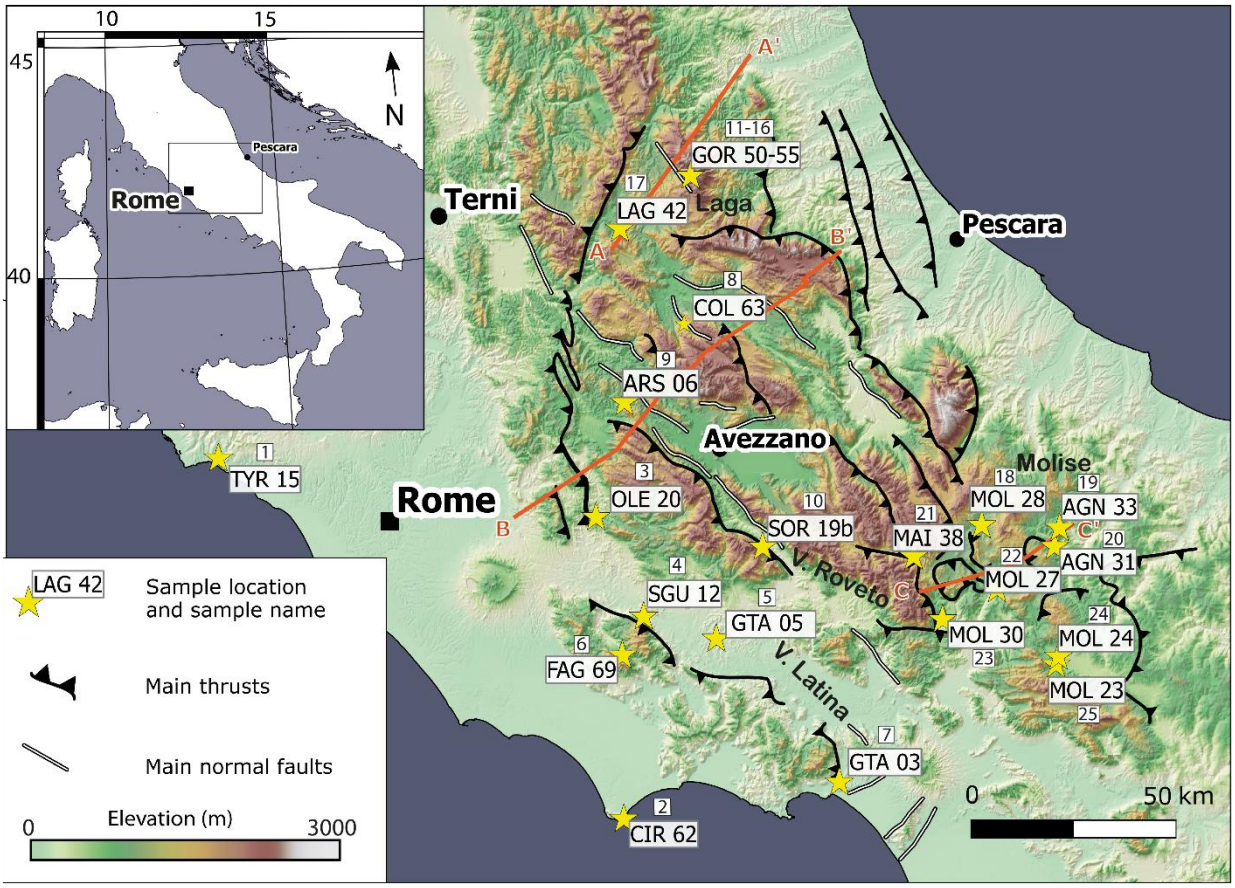

Figure 1. Topographic map of the central Apennines showing the sample locations, their names and their numbers. Main tectonic features are indicated by black (thrusts) and white (normal faults) lines. Red lines AA', BB' and CC' indicate the traces of the geological cross-sections pictured in Figure 3.

To improve the understanding of the Central Apennines uplift history, we compare timing of rock cooling with dated tectonic and/or geodynamic events. We focus on shallow crustal exhumation with low-temperature thermochronology of syn-orogenic siliciclastic turbidites that are commonly exposed in the intramontane basins (Fig. 2). Previous studies have provided few low-temperature thermochronology ages for the Central Apennines, suggesting a Pleistocene exhumation of the easternmost units (Satolli et al., 2014). Exhumation data for the Northern and Southern Apennines is more abundant (Corrado et al., 2010, and references therein). In these regions, the general pattern indicates progressively younger ages (2 – 4 Ma) close to the subduction front, and older and slower exhumation towards the core of the range (Thomson et al., 2010). Our new data suggest that a similar pattern may characterize also the Central Apennines. Moreover, we confirm previous geologic evidence that exhumation started immediately after the cessation of deposition of the turbidites series, and accelerated around 2 Ma in the central and eastern parts of the central Apennines.

2. GEOLOGICAL SETTING

2.1 Geodynamic evolution

The Apennines are part of the peri-Mediterrannean chain, which formed as a result of the Africa-Europe convergence during the Neogene (e.g. Gueguen et al., 1998). The pre-orogenic bedrock is a succession of Jurassic and Cretaceous limestones, which deposited as a carbonate shelf platform in the Tethys realm (e.g. Accordi et al., 1986; Bally et al., 1986; Cosentino et al., 2010). During the Late Oligocene-Early Miocene, the Adria plate started subducting westwards underneath Europe, thereby building the Apennine accretionary wedge at the plate boundary (Royden et al., 1987; Patacca and Scandone, 1989). The propagation of the apenninic front due to slab retreat resulted in the progressive North-Eastwards migration of the foredeep basin. Syn-orogenic turbiditic foreland sequences were incorporated into the chain, often evolving into thrust-top basins (Bally et al 1986; Mostardini and Merlini, 1986; Cipollari and Cosentino, 1995; Fig 2 and 3). These basins were progressively abandoned as the compressional activity moved towards more external domains. During the Apennine orogeny, the eastward retreat of the subduction zone lead to concurrent back-arc opening of the Tyrrhenian basin (Boccaletti et al., 1990). The onset of extension is dated around 8 Ma offshore the Tyrrhenian coast, and becomes younger towards the central part of the orogen (Patacca et al., 1992; Cavinato and De Celles, 1999; Cosentino et al., 2017). South-West dipping normal

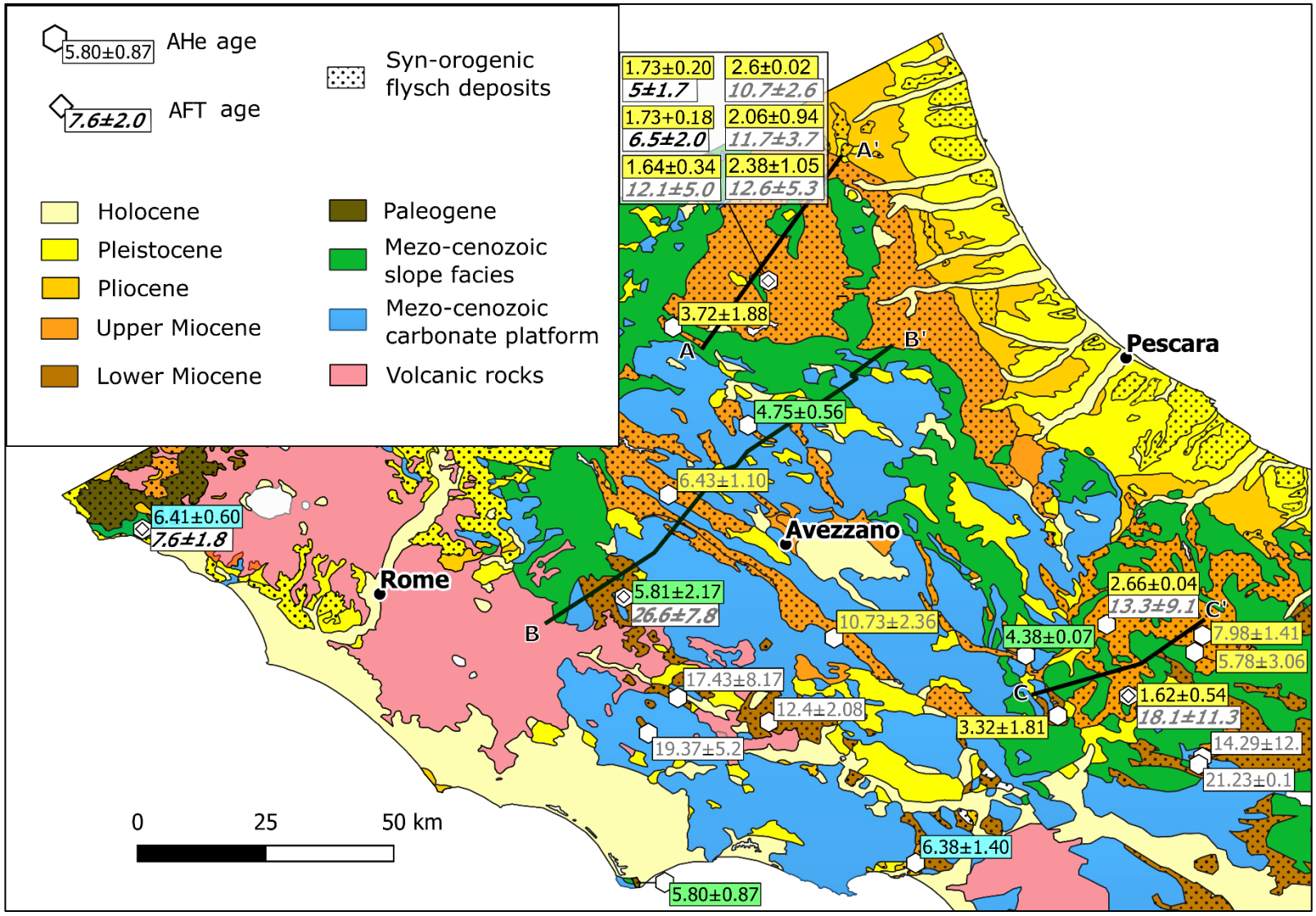

Figure 2. Simplified geological-lithofacies map (modified after Bigi et al., 1992) and low-temperature thermochronology mean age results. Totally reset ages are shown in black font, non- or partially reset ages are shown in grey. Background of the AHe data boxes are colored after the cooling age of the sample; cooling ages from partially reset samples are defined by thermal modelling (see text for details). Blue: Tortonian-Early Messinian; Green: Messinian-Early Pliocene; Yellow: middle Pliocene-Pleistocene; White AHe boxes indicate non reset data which were excluded from the interpretation. Black lines AA', BB' and CC' indicate the traces of the geological cross-sections pictured in Figure 3.

faults overprint the compressive structures. This evolution is testified by seismic reflexion studies in the Tyrrhenian basin (Mascle and Rehault, 1990), as well as geological data (Cippollari and Cosentino, 1992). Based on unconformably overlying sediments in the Adriatic foredeep (Casero, 2004), cessation of compression in the Central Apennines has been dated to the Late Pliocene (Pizzi, 2003; Bigi et al., 2013). This major geodynamic event has been linked to local slab detachement, based on lack of deep seismicity (Chiarabba et al., 2005) and mantel tomography (Wortel and Spakman, 2000; Piromallo and Morelli, 2003).

2.2 Description of sampled syn-orogenic basins

The siliciclastic sediments infilling the syn-orogenic basins are mainly sourced from the Alpine erosion, to a lesser extent in more recent times, from the local Apennine orogeny (e.g. Gandolfi et al., 2007; Stalder et al., 2018). Commonly, they stratigraphically overlay the latest pre-orogenic carbonates, generally represented by the Orbulina Marls (Fig. 3). The flysch deposits can be divided according to their deposition period. The three main kinematic units are defined by the successive eastward jumps of the Apennine thrust front: the pre- Tortonian deposits, the Upper Tortonian foredeep, and the Messinian foredeep.

Pre- Tortonian foredeep

The Cretaceous flysch outcrops as the Pietraforte formation on the northern part of the Tyrrhenian coast, where we sampled TYR15. It is the oldest deposit (94 – 72 Ma) sampled in this study, formed by quartzose turbidite sandstones in the southern and eastern Tethyan Realm (Critelli, 2018).

The Flysch di San Felice represents the earliest syn-orogenic flysch deposit in the Central Apennines, dated to the Late Oligocene (Boni et al., 1980). The lithology varies from marls to arenaceous micro-conglomerates, with an average thickness of 300 m (Boni, 1969). We sampled CIR 62 in a coarse-grained sandstone from the lowest outcropping part of the sequence.

Upper Tortonian foredeep

Upper Tortonian silicoclastic sediments were deposited during the activity of the Latina Valley thrust front, in the Upper Tortonian foredeep (Cipollari and Cosentino, 1995; Cosentino et al., 2003; Cosentino et al., 2010). It outcrops along the Latina Valley and is bounded in NW

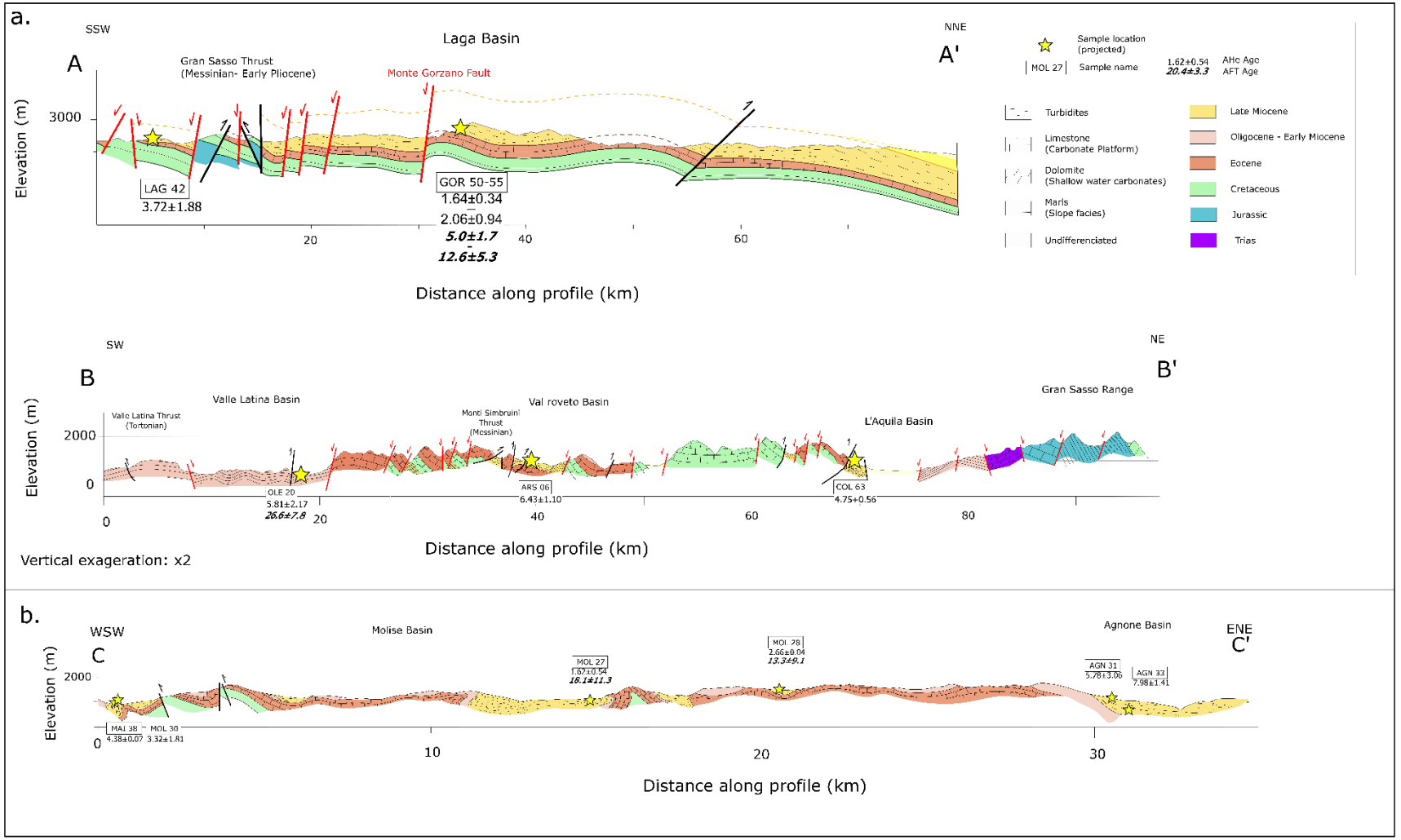

Figure 3. Geological cross-sections across the main syn-orogenic flysch basins and their related tectonic features. Thick red and black lines indicate normal and thrust faults, respectively. Locations are shown in Figs. 1 and 2. a. Northern part of the central Apennines. AA': Laga basin. Dashed lines indicate eroded material, as calculated from kinematic reconstructions using MOVE (Midland Valley, 2018). BB': Valle Latina, Val Roveto and L'Aquila basins. b. Southern sector: Molise and Agnone Basins. Sample locations are projected onto the closest sections.

by the Volsci Range, and extends to the South until the gulf of Gaeta. After being incorporated in the orogen as a piggy-back basin, the flysch deposit was locally overlain with argillaceous deposits known as the Torrice Flysch (Cipollari and Cosentino, 1995). Vitrinite reflectance data of 0.31+-0.03 to 0.35 +- 0.03 from the northernmost part of the basin (Table 1; Corrado, 1995) indicate a maximum burial temperature (Tmax) of 40-50°C (calculated from Barker and Pawlewicz, 1994). We sampled 4 locations in this unit (Fig. 1; Fig 3a):

- GTA 3 in the Gaeta Gulf, from the very bottom of the flysch sequence,
- GTA 5 in Frosinone, (burial depth < 1 km)
- SGU 12 in the footwall of the Latina Valley thrust (burial depth < 1 km)
- OLE 20 in the northernmost part of the Frosinone Unit.

Messinian Foredeep

The Argilloso-Arenacea unit fills the Messinian foredeep while the Monti Simbruini thrust front was active during Late Messinian-Early Pliocene (Cosentino et al., 2010). It outcrops in several areas in the Central Apennines (Fig. 2) and is sub-divided into various formations depending on their geographical locations. It is separated from younger foredeep deposits in the East by the Gran Sasso thrust.

In the Val Roveto basin, where we sampled SOR 19 and ARS 06 (Fig. 1), the Argilloso-Arenacea unit was deposited during the Lower Messinian. The formation appears to be slightly younger close to the L'Aquila basin, where COL 63 was sampled (Centamore et al., 2006). The Laga Formation (samples GOR50-55 and LAG 42) is the sub division of the Argilloso-Arenacea unit which infills the Messinian foredeep North of the Gran Sasso range. Its thickness reached up to 3-4 km close to the depocenter. Vitrinite reflectance values vary between 0.40 and 0.50% (Rusciadelli et al., 2005). In the Molise area, the Argilloso-Arenacea Unit is represented by the Molise Flysch in the South, where we sampled MOL23 to MOL30 and MAI 38, and by the Agnone Formation in the North East (AGN31 and AGN33). Vitrinite reflectance values are comprised between 0.40% and 0.44% (Table 1; Corrado, 1995; Corrado et al., 2005).

Table 1. Vitrinite reflectance and sampling data. Coordinates are given in WGS 84 system. ASL: above sea level.

N.	Sample name	Longitude (°)	Latitude (°)	Elevation (m ASL)	Deposition age (Ma)	Ro (%)	Geological formation name
1	**TYR 15**	11.9359	42.0479	27	94 - 72	-	Pietraforte Fm
2	**CIR 62**	13.0901	41.2247	2	23.03 - 20.44	-	
3	**OLE 20**	13.0494	41.8853	505	11.6 - 7.2	0.33 ± 0.05	Frosinone Unit
4	**SGU 12**	13.1764	41.6638	243	11.6 - 7.2	0.29 ± 0.03	Frosinone Unit
5	**GTA05**	13.3876	41.6072	232	8.4 - 7.2	0.31 ± 0.03	Frosinine Unit
6	**FAG 69**	13.1082	41.5811	850	13.8 - 11.6	-	Orbulina Marls
7	**GTA03**	13.7274	41.2804	101	8.4 - 7.2	0.31 ± 0.03	Frosinine Unit
8	**COL 63**	13.3391	42.2955	941	5.9 - 5.33	0.46 ± 0.01	Arenacea - Pelitica Unit
9	**ARS 06**	13.1503	42.1324	844	8.4 – 7	0.30 ± 0.06	Argilloso Arenacea Unit
10	**SOR 19**	13.5384	41.8022	641	8.4 – 7	0.31 ± 0.05	Argilloso Arenacea Unit
11	**GOR 50**	13.3759	42.6286	1572	7.2 - 5.9	0.46 ± 0.07	Laga Fm
12	**GOR 51**	13.3773	42.6271	1655	7.2 - 5.9	0.46 ± 0.07	Laga Fm
13	**GOR 52**	13.3771	42.6244	1812	7.2 - 5.9	0.46 ± 0.07	Laga Fm
14	**GOR 53**	13.3757	42.6230	1880	7.2 - 5.9	0.46 ± 0.07	Laga Fm
15	**GOR 54**	13.3788	42.6194	2099	7.2 - 5.9	0.46 ± 0.07	Laga Fm
16	**GOR 55**	13.3809	42.6190	2154	7.2 - 5.9	0.46 ± 0.07	Laga Fm
17	**LAG 42**	13.1613	42.5111	811	7.2 - 5.9	0.46 ± 0.02	Laga Fm
18	**MOL 28**	14.1891	41.8217	823	11.6 - 5.3	0.43 ± 0.01	Argilloso Arenacea Unit Agnone Fm
19	**AGN33**	14.4188	41.8049	804	8.4 - 5.3	0.44 ± 0.01	Argilloso Arenacea Unit Agnone Fm
20	**AGN31**	14.4005	41.7654	598	8.4 - 5.3	0.44 ± 0.01	Argilloso Arenacea Unit
21	**MAI 38**	13.9829	41.7626	979	8.4 - 7	0.37 ± 0.07	Molise Flysch
22	**MOL 27**	14.2232	41.6803	590	11.6 - 5.3	0.41 ± 0.03	Argilloso Arenacea Unit Agnone Fm
23	**MOL 30**	14.0574	41.6222	602	11.6 - 5.3	0.44 ± 0.11	Argilloso Arenacea Unit Agnone Fm
24	**MOL 24**	14.3922	41.5254	550	8.4 - 7	0.41 ± 0.03	Molise Flysch
25	**MOL 23**	14.3832	41.5085	672	8.4 - 7	0.41 ± 0.03	Molise Flysch

1. METHODS

3.1 Sample collection and processing

Sampling

The Central Apennines are primarily a carbonate massif, thus apatite bearing lithologies are uncommon. A few exceptions lie in the arenaceous units infilling a series of intermontane basins. Those deposits, ranging from coarse breccias to claystone, are generated from the erosion of surrounding mountain ranges, as far away as the Alps (e.g. Stalder et al., 2018). The crystalline nature of the source rocks allows the presence of minerals suitable for low temperature thermochronology such as apatites and zircons. However, due to the relative fragile nature of apatites and the transport, unbroken large grains suitable for dating with the (U-Th)/He method are sparse.

To meet these requirements, we target mainly deposits with medium to coarse grained sandstones (average grain size between 0.1 and 1 mm). We also avoid sandstones with carbonatic cement and calcarenites, as grains are often coated with an opaque layer preventing the identification of inclusions. We aim for apatites that are thermally reset during their latest burial phase, as this is key for recording the subsequent cooling age. Samples must have been buried at a depth sufficient to reach temperatures higher than the system's closure temperature. We also targeted one age-elevation profile by collecting six samples from the footwall of a large extensional fault (Monte Gorzano fault, Fig. 3) and one sample from its hanging wall.

We use data from vitrinite reflectance on organic matter (Ro, see Table 1) (Corrado, 1995; Corrado et al., 1998; Rusciadelli et al., 2005; Aldega et al., 2007) to identify potential sampling sites where maximum burial conditions should have exceeded 40°C, indicated by a Ro >= 0.30 %. In cases where no vitrinite data is available, we sampled the lowermost outcropping unit in the sedimentary sequence to maximize burial depth, as well as the closest locations to thrust faults where the samples might have been subjected to tectonic burial previous to exhumation.

Processing and analytical procedure

We collected 3 – 10 kg of rock per sample, which were entirely processed at ETH Zurich, Switzerland. Samples were reduced to sand size by electrical pulse fragmentation using a Selfrag. The fraction of grain size <400 μm was processed with standard methods to concentrate the heavy mineral fraction containing apatites. Apatites were hand-picked using a

polarizing stereoscope at high magnification to identify inclusions and to measure the grain dimensions. For AHe thermochronometry, we picked up to 6 single apatite crystals per sample, based on the following characteristics ranked by priority:

- Grain size > 60 μm
- No inclusions
- Simple geometrical form (avoiding broken crystals)
- No coating/surface abrasion

When available, we chose the biggest grains with no fractures nor inclusions, and perfect bipyramydal hexagonal shape. When optimal grains were not available, we prioritized respectively size>60 μm, purity (no inclusions), no internal fractures, and absence of broken tips. Each apatite was photographed and measured to calculate the Ejection Factor (Ft) after Ketcham et al., 2011. Single grains were then enclosed in platinum foil and loaded into the laser chamber. 4He abundances for each grain were determined by degassing at a fixed temperature of about 900 ºC with a diode laser equipped with a pyrometer for three minutes. The released gas was measured on a magnet sector field mass spectrometer equipped with a Baur-Signer ion source at ETH Zurich. After degassing, each crystal was weighed before and after adding the U-Th-Sm isotope spike. The same grain was then dissolved in HNO3. The U-Th-Sm concentration of each dissolved grain was then measured on an inductively coupled plasma mass spectrometer at ETH Zurich (ElementXR). The age error was derived from the analytical uncertainties in U, Th, and Sm measurements, and the variance of the single grain ages (1 standard deviation). Together with our samples, we measured 14 fragments from the standard Durango and we obtained a mean age of 31.4 ± 0.9 Ma which is in very good agreement with the nominal age of the Durango apatite (31.44 ± 0.18 Ma, McDowell et al., 2005) and differs by less than 1.0%. For AFT analysis, grains were mounted in epoxy, polished to expose their internal surface and then etched in HNO3 5.5 N at 21 ºC for 20 s to reveal spontaneous tracks. Apatites mounts were covered with the external detector consisting of thin foils of low U muscovites and packed in tubes together with fluence monitors (CN5) and age standard mounts consisting of Durango and Fish Canyon tuff apatites. Tubes were sent to the Radiation Centre of the Oregon State University where they were irradiated with a nominal integrated flux of 1.2×10^{16} neutron cm^{-2}. After irradiation and unpacking, muscovite sheets were etched in HF 40% for 45 minutes to reveal the induced fission tracks. Tracks were counted at a magnification of 1250x. The ages were calculated using the external-detector (EDM) and the calibration methods (Hurford and Green, 1983).

3.2 Method principles

Thermochronology is used to quantify the rate of rock exhumation over geological time scales to constrain rates and timing of surface evolution, and inferring local erosion rates. Here we combine two low-temperature thermochronometers: (U-Th-Sm)/He on apatite (AHe) and apatite fission track (AFT). The AHe method is based on the natural radioactive decay of father isotopes (U, Th and Sm), and accumulation or loss of the thereby created daughter isotope (He). The AFT method is based on the natural decay of U by fission, which produces fragments of nuclei that have a high kinetic energy and that are positively charged. These fragments cause damage trails in the crystalline lattice, namely the fission tracks, which can be visible at the microscope after physical enhancement obtained with a chemical etch procedure. Retention of the decay products in apatites is mainly temperature dependent such that when a rock cools below its closure temperature (Tc; Dodson, 1973), the retention of the decay products occurs at a higher rate than the loss by diffusion or annealing. For the AHe system, assuming a cooling rate of 10 ºC/km, the nominal Tc is about 67 ºC (Reiners and Brandon, 2006), which corresponds to a closure depth of < 2 km if the surface temperature is 10 ºC and if the upper crust is characterized by a steady geothermal gradient of 30°C/km. Thus, exhumation of < 2 km will bring to the surface samples that have cooled below the AHe Tc. The nominal AFT Tc is 116 ºC at a cooling rate of 10 ºC/Ma for average composition apatites. Assuming a surface temperature of 10 ºC and a steady geothermal gradient of 30 ºC/km, the AFT Tc corresponds to a closure depth of about 3.5 km. In order to fully reset the cooling age of detrital apatites by depositional or tectonic burial, temperatures higher than those of the AHe partial retention zone (PRZ) and of the AFT partial annealing zone (PAZ), respectively, are necessary. These temperatures are higher than the closure temperatures of the different thermochronologic systems and they vary significantly with the duration of burial: to fully reset a thermochronometric system, a short burial or heating event requires higher temperatures than a long burial. If burial conditions are such that no full thermal resetting is achieved, samples retain partially or fully the cooling record of their earlier thermal history.

The kinetic parameters of the AHe system vary quite significantly with the degree of the radiation damage induced by the decay process: at low damage density, the He retentivity is increased as the damages act like He traps, whereas at high damage density the He retentivity is increased by the interconnection between defects (Shuster et al., 2006; Flowers et al., 2009; Gautheron et al., 2009). The radiation damage is primarily a function of the U and Th concentrations and also of the thermal history of the sample as it can anneal through diffusive

processes. The effective U (eU in ppm) is commonly used as a proxy to account for the radiation damage due to the U and Th concentration (Flowers et al., 2007). The composition of apatite affects in particular the kinetics of fission-tracks annealing. The composition also affects how apatites respond to the etch procedure such that the diameter of the spontaneous tracks after etching can be used as a proxy to correct the track annealing kinetic parameters (Donelick et al., 1991; Donelick et al., 1999). This proxy, namely Dpar, is measured at the microscope in the direction parallel to the apatite C-axes on the same crystals where tracks are counted and for each crystal an average Dpar is determined based on as many as Dpar are measurable depending on the track density.

3.3 Quantification of cooling histories with thermal modelling

In cases where AHe or AFT ages are complex, for example when single grain ages are dispersed, or if the thermochronological cooling age coincides with the geological deposition age, thermal modelling is useful to refine the thermal history, as it is able to take into account the complex effects of diffusion and annealing kinetics depending on single grain characteristics. This is especially useful for samples that are reset to an unknown degree, have been re-heated, or have spent a long time in the partial retention zone (PRZ).

Thermal histories were determined using the QTQt code from Gallagher (2018), which is based on inversion of thermochronological ages. This approach uses a Markov-Chain Monte-Carlo method to resolve a probability distribution of time-temperature paths for single or multiple samples. The model applies AHe diffusion and AFT annealing kinetics, taking into account the effects of alpha damage (Gautheron et al., 2009) and of variable apatite composition (Ketcham et al., 2007). Alpha ejection factor (Ft) is calculated from the grain geometry during the thermal modelling, and outputs are given in reference to corrected ages (Gallagher, 2018). The input parameters are the AHe data for single grains (He, U, Th, Sm contents and equivalent sphere radius Rs), sampling altitude, and, if necessary, independent time-temperature constraints. We allow for reheating during thermal history, and required the model to keep more complex time-temperature paths if they improved the data fit during inversion, as we do not expect the thermal history to be plain. The burn-in process – the number of steps taken by the model to refine the search domain before creating the thermal history – was set to a minimum of 10 000 iterations, and the post burn-in – the steps retained for the output model – to 100 000. Increasing the number of iterations allows the model to reach a

more reliable result. We qualitatively assess the performance of the model by examining the variation of likelihood and posterior values with iterations, as they should fluctuate around a constant mean value without apparent trend (Gallagher, 2018). We run the model until the likelihood and posterior chains show a satisfying convergence. We do not interpret models that kept diverging. The present-day temperature range is set to 15 ± 10°C. We generally preferred models with the fewest additional parameters input; whenever sufficient, we let the model run freely with only the thermochronological data as input. To test the validity of the outputs, we compared modelled time-temperature paths with independent geological constraints like deposition age of the unit, burial depth, and Tmax as calculated from vitrinite reflectance.

QTQt can also be used to characterize the thermal histories of samples collected along a steep elevation transect. In this case, additional input parameters are necessary and these include an initial geothermal gradient and the modern temperature difference among the samples. We used this approach for the samples collected on the footwall of the Monte Gorzano fault, where six samples are located over an elevation difference of 600 m and a horizontal distance of 1.3 km. We input 30 ºC/km as initial geothermal gradient and 17.5ºC as modern temperature difference.

1.4 Quantification of exhumation

We derived information on the amount and rate of exhumation in the Central Apennines using our fully reset samples as input for Agetoedot by Willett and Brandon, 2013. This method inverts individual ages to erosion rates solving for the closure temperatures based on the Dodson equation (1973) and for the geothermal gradient based on a solution of the thermal field in a semi-infinite space where heat is advected towards the surface with erosion. The basic assumption of this method is that the cooling rate is constant during erosion as this is implicit in the Dodson solution to the closure temperature. The resulting erosion rates are constant from the time of closure to the surface, whereas the geothermal gradient increases with erosion. The input diffusion parameters for the AHe ages are corrected to account for the effect of the grain size. A correction that accounts for the effect of topography on the geothermal gradient and the shape of the isotherms at depth is also possible: however, this correction is commonly quite small and we did not apply it. The input parameters for this inversion without topographic correction are: the cooling age (τ), the equivalent radius for the diffusion domain size (Rs), the onset time for erosion, the final geothermal gradient, and the present surface mean temperature

at the sample location. Output parameters include the closure depth (*Dc*), the geothermal gradient at the onset of erosion and the erosion rate ($\dot{e}$). We input the central age of reset AFT samples and the single grain ages of reset AHe samples. The $\dot{e}$ value of the individual AHe grains were averaged to obtain an $\dot{e}$ value for each sample. We used three different onset times: 5.3 Ma for sample COL63 that has a depositional age between 5.9 and 5.3 Ma, at 6.5 Ma for the samples for the sample from the Messinian foredeep, and 8 Ma for all the other samples. The final geothermal gradients should represent the present-day geothermal field and we used two values for this input parameter, 35 ºC/km and 55 ºC/km, for which we obtained two corresponding $\dot{e}$ that we averaged. As surface temperature, we used 15 ºC for all the input data. In order to constrain the exhumation path of our samples, we used *Dc* and $\dot{e}$ to derive the depth (D_i) of our samples at three significant times (t_i): at 4, 2 Ma and 1.5 Ma. We derived *Di* using this equation:

$$D_i = Dc - (\tau - t_i)\dot{e}.$$

2. RESULTS

4.1 Cooling ages

We report mean ages with their location in Figures 2 and 3. Single grain AHe ages are reported in Table 2, and AFT data in Table 3 and supplementary material Figs. S1 and S2. To discriminate between reset and non-reset samples, we compare their cooling age to their depositional age: we define as reset the samples whose single grain ages (for AHe) or central age (for AFT) are younger than the midpoint of their depositional period (Tables 1, 2 and 3), i.e. they plot above the 1:1 line in Figure 4.

Overall, our AHe ages range from 1 to 23 Ma, and our AFT ages range from 5 to 25 Ma. In the Laga and Molise regions (Fig. 4), single grain AHe ages are as young as 1 Ma and the reset grains scatter around ~ 2 Ma. Everywhere else, the single grain ages are no younger than 4 Ma.

The occurrence of ages younger than the depositional age is very low in the Val Latina region and increases towards the west and the east. Along the Tyrrhenian coast, both thermochronometers are younger than the depositional age and therefore totally reset: they feature ages between ~6 and ~8 Ma. In the Valle Latina area, most samples (SGU12, GTA05,

Table 2. Apatite (U-Th)/He ages. N is the sample number. Bold values are mean ages calculated from the single grain values below. Ft in the ejection factor calculated after Ketcham et al., (2011). eU = U+ 0.235 Th. 1σ are standard deviations.

N.	Sample	^{238}U *(fmol)*	^{232}Th *(fmol)*	^{147}Sm *(fmol)*	He *(fmol)*	eU *(ppm)*	Rs *(μm)*	Raw Age *(Ma)*	Ft	Corrected Age *(Ma)*	Error ±1σ *(Ma)*	Average Age *(Ma)*	Error ±1σ *(Ma)*
1	**TYR15**											**6.41**	**0.60**
1.1	TYR15a1	616.78	3733.54	685.67	8.54	76.55	57.0	4.47	0.747	5.99	0.02		
1.2	TYR15a2	92.76	402.70	204.05	0.95	75.35	28.9	3.94	0.578	6.83	0.05		
2	**CIR62**											**5.80**	**0.87**
2.1	CIR62a1	13.80	166.53	70.29	0.23	15.77	32.3	3.39	0.610	5.55	0.12		
2.2	CIR62a2	37.46	122.95	272.57	0.46	4.84	50.9	5.32	0.829	6.41	0.11		
2.3	CIR62a3	35.30	290.42	184.35	0.36	35.96	30.9	2.70	0.617	4.38	0.14		
2.4	CIR62a4	127.46	455.24	1226.50	1.74	3.69	88.2	5.65	0.907	6.22	0.06		
2.5	CIR62a5	161.79	499.65	1459.85	2.11	6.14	77.0	5.75	0.896	6.42	0.05		
3	**OLE20**											**5.81**	**2.17**
3.1	OLE20a1	98.90	69.60	47.30	0.47	10.38	47.8	3.16	0.740	4.27	0.04		
3.2	OLE20a2	70.90	39.10	23.50	0.49	18.94	35.0	4.70	0.640	7.34	0.08		
4	**SGU12**											**17.43**	**8.17**
4.1	SGU12a1	38.74	86.09	39.86	1.00	36.11	25.8	13.18	0.519	25.39	0.16		
4.2	SGU12a2	89.82	65.78	72.48	0.67	71.70	24.4	4.91	0.542	9.06	0.05		
4.3	SGU12a3	130.70	391.55	383.57	3.77	32.91	40.9	13.10	0.734	17.84	0.05		
5	**GTA05**											**12.40**	**2.08**
5.1	GTA05a1	75.25	24.97	64.72	0.88	14.65	38.1	8.39	0.728	11.53	0.06		
5.2	GTA05a2	12.23	32.37	66.78	0.21	3.21	37.0	8.31	0.762	10.90	0.26		
5.3	GTA05a3	315.04	437.07	143.31	5.09	78.97	37.1	9.46	0.640	14.78	0.05		
6	**FAG69**											**19.37**	**5.23**
6.1	FAG69a1	56.77	247.35	237.35	2.96	15.95	43.9	19.93	0.752	26.49	0.18		
6.2	FAG69a2	50.10	172.45	102.14	1.96	5.03	57.6	16.80	0.788	21.33	0.14		
6.3	FAG69a3	28.62	85.80	51.83	0.56	14.93	32.2	8.91	0.628	14.18	0.26		
6.4	FAG69a4	115.49	410.96	324.95	4.57	33.55	39.5	16.69	0.710	23.52	0.13		
6.5	FAG69a5	123.15	257.61	150.67	2.73	37.09	37.7	11.53	0.676	17.05	0.11		

6.6	FAG69a6	46.62	180.05	163.19	1.07	23.94	34.8	9.33	0.684	13.65	0.10		
7	**GTA03**											**6.38**	**1.40**
7.1	GTA03a1	96.20	718.00	459.00	1.27	49.50	38.1	3.73	0.691	5.40	0.03		
7.2	GTA03a2	144.00	203.00	312.00	1.38	28.10	41.2	5.56	0.754	7.37	0.05		
8	**COL63**											**4.75**	**0.56**
8.1	COL63a1	77.47	11.14	31.42	0.38	6.68	52.3	3.69	0.778	4.75	0.11		
8.2	COL63a3	93.15	177.14	64.60	0.49	21.55	40.8	2.83	0.676	4.19	0.06		
8.3	COL63a4	40.00	17.57	305.21	0.26	9.24	36.9	4.50	0.847	5.31	0.12		
9	**ARS06**											**6.43**	**1.10**
9.1	ARS06a1	36.01	86.21	130.26	0.35	6.97	41.8	4.82	0.767	6.28	0.05		
9.2	ARS06a2	216.93	122.59	492.30	1.97	10.81	56.4	6.17	0.847	7.28	0.04		
9.3	ARS06a4	138.89	183.20	187.60	0.75	60.17	31.7	3.21	0.649	4.94	0.06		
9.4	ARS06a5	68.44	78.48	127.76	0.46	28.66	32.4	4.09	0.688	5.93	0.06		
9.5	ARS06a6	429.75	102.54	136.09	3.35	50.47	47.5	5.71	0.741	7.71	0.04		
10	**SOR19b**											**10.73**	**2.36**
10.1	SOR19ba1	224.00	221.00	144.00	2.61	79.53	32.0	7.33	0.617	11.89	0.06		
10.2	SOR19ba2	37.40	21.20	41.60	0.28	11.39	33.5	5.18	0.694	7.46	0.09		
10.3	SOR19ba3	349.00	162.00	278.00	4.19	51.64	44.9	8.37	0.754	11.09	0.05		
10.4	SOR19ba4	220.00	357.00	405.00	4.13	31.19	46.8	10.51	0.769	13.67	0.05		
10.5	SOR19ba5	20.80	60.80	27.90	0.34	1.65	60.4	7.49	0.786	9.54	0.13		
11	**GOR50**											**1.73**	**0.20**
11.1	GOR50a1	170.79	451.18	298.10	0.53	15.66	51.5	1.49	0.772	1.93	0.02		
11.2	GOR50a2	140.54	313.28	79.44	0.22	87.47	32.3	0.82	0.529	1.54	0.02		
11.3	GOR50a4	415.80	199.98	408.21	0.72	96.13	37.4	1.21	0.704	1.72	0.01		
12	**GOR51**											1.73	0.18
12.1	GOR51a1	32.17	200.15	49.64	0.13	9.86	43.6	1.29	0.681	1.90	0.02		
12.2	GOR51a2	481.94	956.48	356.35	1.05	50.35	55.6	1.15	0.745	1.55	0.01		
12.3	GOR51a4	1794.57	842.31	2268.89	3.94	51.35	74.6	1.53	0.866	1.76	0.01		
13	**GOR52**											**1.64**	**0.34**
13.1	GOR52a1	141.18	257.90	161.24	0.21	57.54	34.1	0.79	0.631	1.26	0.01		
13.2	GOR52a4	12.23	29.88	19.30	0.03	5.76	33.9	1.09	0.626	1.75	0.14		

13.3	GOR52a5	546.13	526.19	607.80	1.21	78.97	50.3	1.40	0.735	1.91	0.01		
14	**GOR53**											2.60	0.02
14.1	GOR53a1	523.10	1034.40	1033.06	2.04	50.91	59.4	2.06	0.793	2.60	0.02		
15	**GOR54**											**2.06**	**0.94**
15.1	GOR54a1	1200.00	2770.00	325.00	2.64	180.15	46.7	1.11	0.684	1.63	0.01		
15.2	GOR54a2	31.50	47.60	25.30	0.06	12.36	32.1	1.07	0.615	1.74	0.11		
15.3	GOR54a3	194.00	490.00	241.00	0.45	9.04	68.8	1.13	0.815	1.39	0.02		
15.4	GOR54a4	242.00	432.00	422.00	1.19	56.22	40.1	2.68	0.723	3.71	0.03		
15.5	GOR54a5	160.00	289.00	162.00	0.36	23.43	38.3	1.23	0.681	1.81	0.02		
16	**GOR55**											**2.38**	**1.05**
16.1	GOR55a1	134.00	59.90	136.00	0.25	36.56	34.1	1.29	0.701	1.85	0.03		
16.2	GOR55a2	214.00	464.00	198.00	0.56	40.75	42.8	1.34	0.699	1.91	0.02		
16.3	GOR55a4	976.00	895.00	915.00	4.71	93.27	51.7	3.07	0.776	3.96	0.02		
16.4	GOR55a5	19.60	101.00	15.50	0.07	5.58	43.8	1.21	0.669	1.81	0.09		
17	**LAG42**											**3.72**	**1.88**
17.1	LAG42a2	53.44	133.63	69.73	0.49	12.39	41.7	4.51	0.699	6.45	0.10		
17.2	LAG42a3	74.27	156.93	148.44	0.32	32.97	34.1	2.20	1.000	2.20	0.03		
17.3	LAG42a4	327.14	544.48	133.77	1.17	51.19	45.4	2.00	0.695	2.87	0.02		
17.4	LAG42a5	649.06	396.09	300.01	2.19	114.22	38.8	2.28	0.683	3.34	0.03		
18	**MOL28**											**2.66**	**0.04**
18.1	MOL28a1	94.44	72.67	191.73	0.28	26.44	34.2	1.95	0.732	2.66	0.04		
19	**AGN33**											**7.98**	**1.41**
19.1	AGN33a1	67.54	42.15	32.17	0.45	12.15	39.2	4.52	0.689	6.57	0.06		
19.2	AGN33a3	129.28	91.64	302.85	1.08	23.06	37.5	5.51	0.768	7.17	0.04		
19.3	AGN33a4	663.02	179.34	1735.22	8.00	20.82	70.5	8.68	0.891	9.75	0.03		
19.4	AGN33a5	533.74	372.57	791.05	5.56	45.01	55.1	6.90	0.818	8.45	0.06		
20	**AGN31**											**5.78**	**3.06**
20.1	AGN31a1	888.88	1356.23	1719.40	10.82	48.16	56.7	6.93	0.814	8.51	0.03		
20.2	AGN31a2	263.21	401.82	124.30	0.68	95.57	32.7	1.48	0.596	2.47	0.02		
20.3	AGN31a3	163.04	131.31	340.99	1.24	26.37	40.3	4.91	0.772	6.36	0.04		
21	**MAI38**											**4.38**	**0.07**

21.1	MAI38a1	44.10	120.00	107.00	0.26	24.98	31.2	2.83	0.646	4.38	0.07		
22	**MOL27**											**1.62**	**0.54**
22.1	MOL27a3	74.02	77.05	35.40	0.16	12.20	45.1	1.39	0.694	2.00	0.03		
22.2	MOL27a4	37.28	78.38	173.21	0.07	6.48	44.1	0.98	0.795	1.23	0.05		
23	**MOL30**											**3.32**	**1.81**
23.1	MOL30a1	225.00	276.00	195.00	1.34	70.21	35.7	3.58	0.663	5.41	0.03		
23.2	MOL30a2	9.08	215.00	22.60	0.11	6.04	45.5	1.45	0.672	2.16	0.07		
23.3	MOL30a3	98.90	69.60	47.30	0.26	8.85	47.3	1.77	0.739	2.40	0.05		
24	**MOL24**											**14.29**	**12.69**
24.1	MOL24a1	62.18	51.98	30.41	0.37	10.64	45.0	3.87	0.699	5.53	0.05		
24.2	MOL24a2	336.27	114.77	803.92	12.01	13.33	68.9	25.30	0.877	28.85	0.10		
24.3	MOL24a3	2.34	41.32	11.02	0.10	0.72	58.5	6.26	0.737	8.50	0.19		
24.4	MOL24a5	1823.13	3771.11	799.10	7.52	70.41	70.9	2.16	0.800	2.70	0.01		
25	**MOL23**											**21.23**	**0.10**
25.1	MOL23a2	107.55	389.89	47.29	2.44	115.53	25.8	9.56	0.450	21.23	0.10		

FAG69) are older than 9 Ma, therefore not reset, and show an important age dispersion. GTA03 and OLE20, from the Upper Tortonian Frosinone Unit, are reset and yield AHe ages between 4 and 7 Ma. ARS06 and SOR19, from Val Roveto, are non- or partially reset, with ages from ~6 to 11 Ma. In the same area, COL63 has a reset mean AHe age of 4.75 ± 0.56 Ma. In the Molise area, some samples are at least partially reset for AHe (MOL24, AGN31 and AGN33) and fully reset samples (MOL27, MOL28, MOL30) feature mean AHe ages between 1.62 ± 0.54 Ma to 3.32 ± 1.81 Ma. AFT ages in this area (> 13 Ma) are not reset. MAI38 (4.38 ± 0.07 Ma; reset) and MOL23 (21.23±0.1 Ma; non-reset) AHe ages are each based on a single grain. In the Laga formation (7.2 – 5.9 Ma), the samples from the vertical profile in the footwall of the Monte Gorzano Fault have been dated with both AHe and AFT (Fig. 5). The AHe ages on the vertical profile range from 1.64 ± 0.34 Ma to 2.6 ±0.02 and the two highest samples have single grain ages that are more dispersed than the those of the lower samples. Only two AFT ages from the lowermost samples have central ages that overlap and or are younger than the depositional age (GOR50 and GOR51), with cooling ages of respectively 5.0 ±1.7 Ma and 6.5 ± 2 Ma. The AFT central ages for the higher samples range from 10.7 ±1.7 Ma to 15.0 ± 1.8 Ma and therefore are non-reset. An additional sample in the Laga Formation (LAG42), in the hanging wall of the Monte Gorzano fault, has a mean reset AHe age of 3.72 ± 1.88.

Table 3. Table 3. AFT data. Ns: number of spontaneous tracks counted on apatite surface; ρs: spontaneous track density; Ni: number of induced tracks; ρi: induced track density; Nd: number of dosimeter tracks; ρd: dosimeter track density; P(χ)2: probability of obtaining Chi-square value for n degrees of freedom (where n= number of crystals − 1). See supplementary material for details.

N.	Sample ID	No. of crystals	N_s	ρ_s	N_i	ρ_i	Mount	ρ_d	$P(\chi^2)$	Central age	2σ	mean Dpar	2std
				$1e^5/cm^2$		$1e^5/cm^2$		$1e^5/cm^2$	%	Ma	Ma	μm	mum
1	TYR15	34	78	0.8	2914	29.76	1	15.93	78.42	7.6	1.8	1.86	0.80
	TYR15						2	16.15					
3	OLE20	27	333	3.00	3866	34.85	1	17.44	0	25.4	12.5	1.62	0.65
11	GOR50	30	37	0.46	1652	20.38	1	12.52	72.24	5.0	1.7	1.35	0.48
12	GOR51	29	80	0.76	2978	28.27	1	13.27	24	6.5	2.0	1.71	0.56
13	GOR52	27	123	1.09	2825	25.07	1	14.03	0	12.1	5.0	2.58	1.30
14	GOR53	32	196	1.49	4502	34.14	1	14.79	0.14	10.7	2.6	2.05	1.40
	GOR53						2	15.16					
15	GOR54	30	116	1.04	2833	25.47	1	15.54	0	11.7	3.7	1.67	0.61
16	GOR55	30	158	1.04	4273	28.19	1	16.30	0	12.6	5.3	1.77	0.55
18	MOL28	22	286	2.94	2885	29.68	1	11.19	0	13.3	9.1	1.67	0.51
20	AGN31	20	196	1.84	2664	25.03	1	10.62	54.93	13.9	2.3	1.71	0.74
22	MOL27	20	169	3.13	1597	29.53	1	10.76	0	18.1	11.3	1.60	0.53

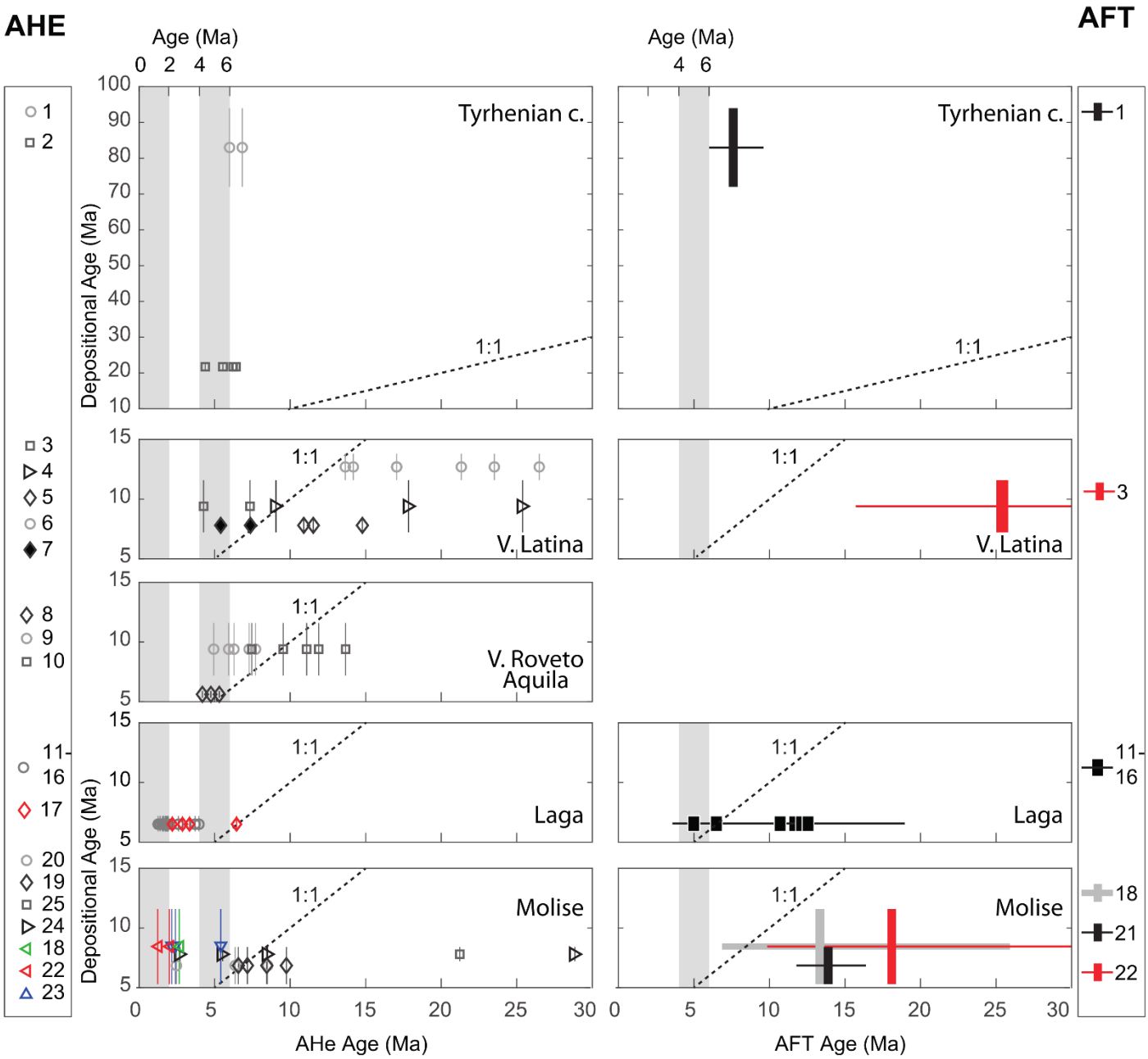

Figure 4. AHe single grain and AFT plotted against their average deposition age. Vertical error bars indicate the maximum span of deposition age. Horizontal error bar of AFT ages represents 95% error. Samples are binned by geographical location (see Fig. 1) and are presented from west to east.

4.2 Thermal Modeling

Among the partially reset samples, we selected for thermal modelling four samples (SOR19, ARS06, AGN31 and AGN33; Fig. 6) with at least three dated grains and with a majority of ages within or younger than the depositional interval. Three of these samples show a positive correlation between ages and effective radius (Rs) and no clear correlation with eU. For all samples, modelling results indicate an acceleration in cooling rate from 2 Ma towards

the present after a stay in the PRZ (Fig. 6). SOR19 shows first slow cooling phase (~ 4°C/ Ma) between 13 and 6 Ma, followed by a 5 My period in the PRZ and a recent rapid cooling to surface temperature (25°C/Ma since 1.5 Ma). ARS06 remains in the PRZ until 2 Ma and then reaches surface temperature with a cooling rate of 15°C/Ma. For AGN 31, the model suggests a stay in the PRZ from 8 to 4 Ma, followed by a re-heat to 70°C around 1 Ma, and a very rapid cooling afterwards. The AGN33 model is characterized by a long stay in the PRZ from ~10 Ma until 2 Ma, from where it cools to surface temperature at a rate of ~20°C/Ma.

Thermal modelling on the samples from the vertical profile is constrained by both AHe and AFT ages, among which several are non-reset. We added a constraint to force the model to meet surface conditions (15 ± 10 °C) around deposition time (9 ± 2 Ma). The cooling history shows heating to 60-120°C before 2 Ma, followed by a very rapid cooling (~70°C/Ma) to surface temperature (Fig. 5).

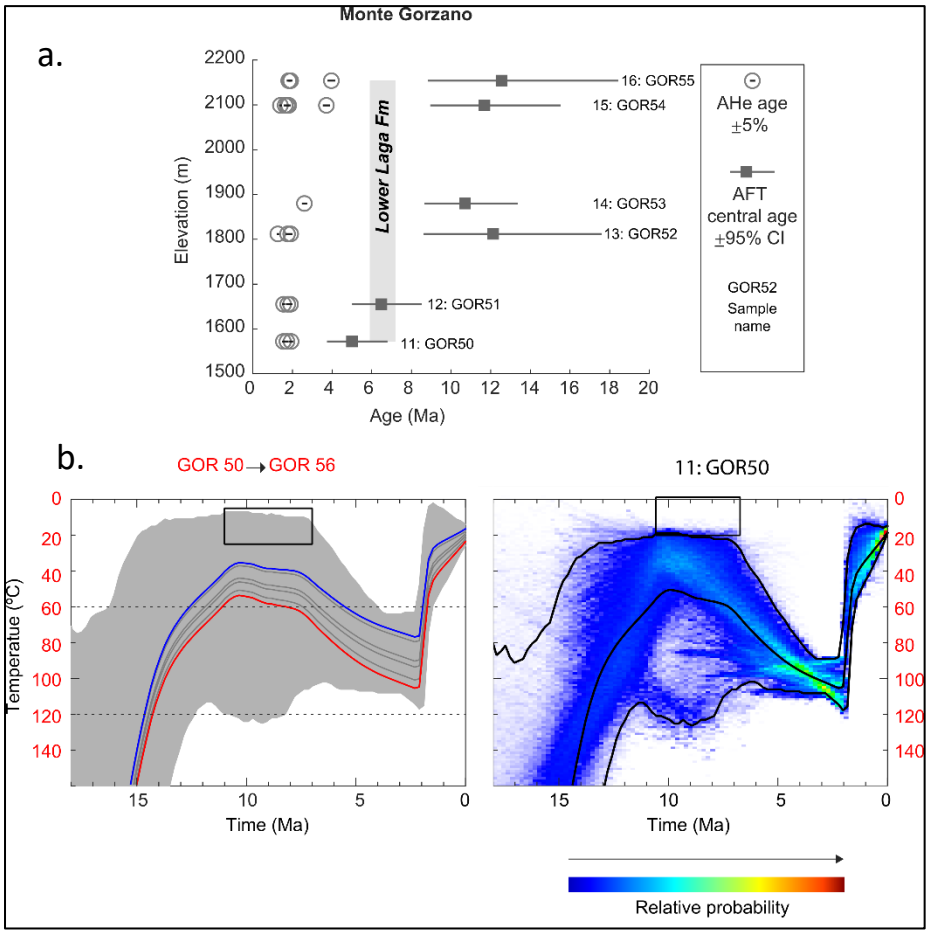

Figure 5. a. Age-Elevation graph for the vertical profile from the Laga basin (GOR 50-GOR55). Grey area indicates the deposition period of the Laga Fm. Horizontal error bars represent the standard error for AHe ages and the 95% error for AFT ages. b. Thermal modelling results for the vertical profile. blue and red lines represent the expected cooling paths of the highest and lowest samples of the profile, and grey lines represent the samples in between. Grey area indicates the 95% probability envelope. c. Thermal modelling results for the lowermost sample GOR50. Relative probability of time-temperature path is indicated by the color scale. Black lines indicate the expected model and its Bayesian credible interval of 95% probability range. (Gallagher, 2018). Black boxes indicate a priori thermal constraints.

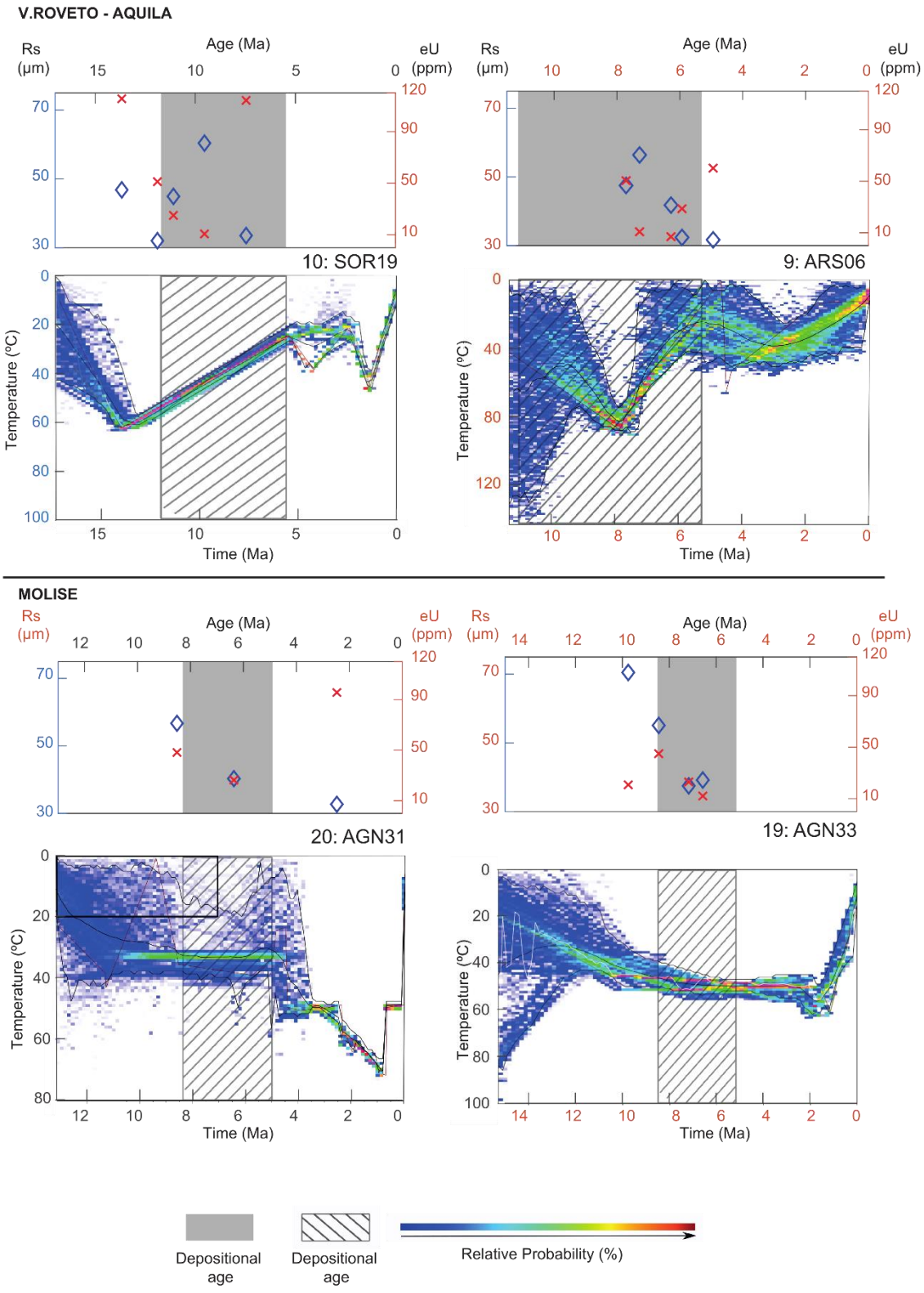

Figure 6. Thermal modelling results and single grain He data. Relative probability of time-temperature path is indicated by the rainbow color scale. Black lines indicate the expected model and its bayesian credible interval of 95% probability range. Dark red line indicates the maximum likelihood model (Gallagher, 2018). Striped boxes and grey areas show the possible range of deposition age for the sample. Black boxes indicate a priori thermal constraints. Rs: equivalent sphere radius of the apatite grain. eU: equivalent Uranium content (eU = U+ 0.235 Th)

4.3 Exhumation paths

With the Agetoedot inversion, for the input present-day geothermal gradient of 35 ºC/km, we derived geothermal gradients at 6.5 and 8 Ma in the range of 13 to 27 ºC/km and for the input gradient of 55 ºC/km, in the range of 31 to 47 ºC/km (Table S1, supplementary material). The lower geothermal gradients correspond to higher $\dot{e}$, in the range from 0.2 to 1.7 km/Ma and the higher geothermal gradient to $\dot{e}$ from 0.1 to 1.0 km/Ma. In Figure 7, we report the results for *Dc* and *Di*: the reset AFT samples closed at depth between 3 and 4 km, whereas the reset AHe closed at depth between 1 and 2 km. At 4 Ma, west of the Molise and Laga region, all the reset samples were at depth less than 1 km whereas the Molise and Laga samples were exhuming fast from depth either greater than 2 (GOR50) or between 2 and 1 km. At 1.5 Ma, most of the Molise samples and all the Laga samples were between 1.5 and 0.5 km deep whereas the rest of the samples were already only less than 0.5 m deeper than today.

5. Discussion

5.1 Robustness of results

5.1.1 Age dispersion

The dispersion of single grain AHe ages can originate from different factors. The grain size (characterized by Rs, Table 2) is primarily correlated to the AHe age (Fig. 6), as the size of the diffusion domain influences the closure temperature of individual grains (Reiners and Farley, 2001). We correct for this influence in the calculation of closure depths reported in Figure 7, as well as in the thermal models. Old outlier grain ages (MOL24a2; MOL30a1; LAG42a2) can be attributed to small He-bearing inclusions that might have been overlooked during picking. Inclusions can degas He but are not entirely dissolved if a gentle dissolution procedure is used, as in our case, thus causing to overestimate the age of the grain (Vermeesch et al., 2007). This is most likely to happen for rough or opaque crystals, common in clastic sediments. Another source of uncertainty comes from the calculation of the alpha ejection factor Ft; although it can account for most morphologies, it is limited in case of irregular or broken grain shapes (Ketcham et al., 2011) and leads to age dispersion (Beucher et al., 2013). Although all of these factors certainly affect to some extent our results, our data indicate that, nevertheless, the age dispersion is mostly controlled by the thermal histories of the dated grains before and after deposition. In fact, for instance, samples GOR50 to GOR55 are from the most deeply buried

sediments that we analysed with Ro values of 0.46 ± 0.07% and have young ages (~ 2 Ma) with a grain age dispersion relatively small in comparison to the rest of our ages (Fig. 4). This likely reflects both deep burial and rapid cooling and all of the factors that could cause age dispersion seem to have little influence on the resulting ages for these samples.

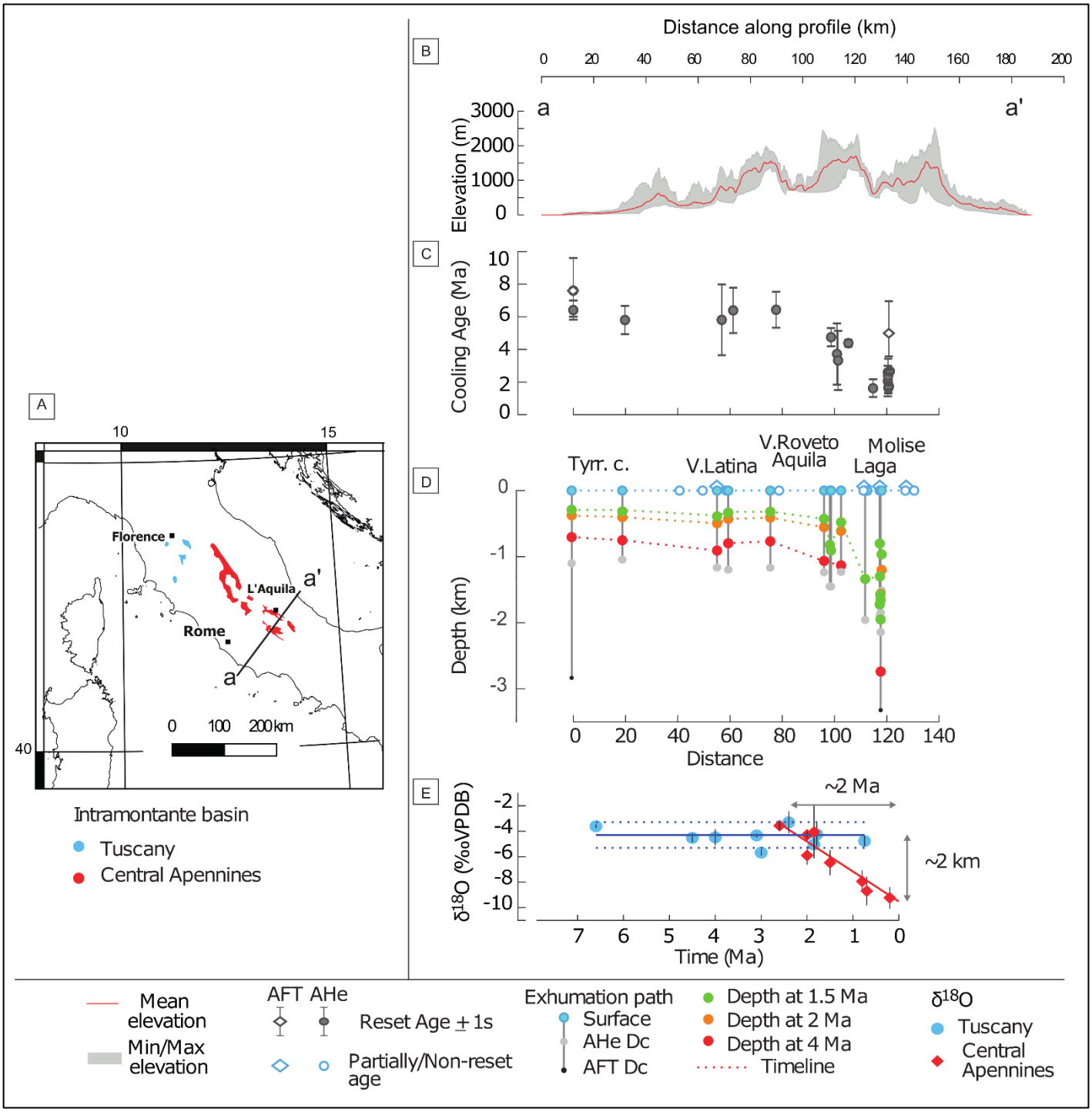

Figure 7. Data summary of surface evolution across the central Apennines. A. Location map of paleoaltimetry data of panel 7.E modified after San Jose et al., (submitted). B. a-a': topographic 40 km-wide swath profile across the central Apennines from panel 7.A. C. AHe (circles) and AFT (diamonds) cooling ages projected along a-a'. D. Exhumation depths over time calculated from cooling ages along the profile a-a'. E. Average autoginic carbonate δ18O and their formation age. The 2 km corresponds to the estimated paleoaltimetry signal. V-PDB: Vienna Pee Dee Belemnite, after San Jose et al., (submitted).

5.1.2 Degree of resetting

In order to define the degree of resetting of our ages, we compare them to the depositional age of the sampled sediments. Alternatively, we could use the available vitrinite data as they constraints the maximum burial temperatures. However, in most cases, we collected our samples not at the same locations of the vitrinite data as we targeted different sedimentary facies to maximize the probability of finding datable apatites. Moreover, the degree of resetting depends not only on the maximum temperatures reached during depositional or tectonic burial but also on the duration of heating such that vitrinite data alone can be insufficient to define the degree of resetting. Due to the scatter and the uncertainty of the cooling ages as well as the uncertainty of the depositional age, caution is necessary when defining the degree of resetting based on the depositional age especially when only a few grains per sample are available. That said, we do not interpret any sample where all the ages are non-reset. Moreover, we model and use for interpretation a few partially reset samples that we selected based on the quantity of dated grains, on their quality and their ages.

Due to the possible differences in apatite composition, pre-depositional history and U concentration combined with maximum temperature conditions close to that of AHe closure, the resetting degree can vary for each single grain within a sample. This is the case for MAI38, SOR19, LAG42, AGN33 and MOL24. We consider those samples partially reset, and, when possible, we process the data with QTQt to gain insights on their post-depositional cooling history.

5.1.3 Thermal modelling

QTQt results are output in terms of a relative probability of a time-temperature combination to reproduce the observed ages (Gallagher, 2012). Any input dataset will be processed by the inversion, regardless of the quality of the dataset, and will result in an output. Therefore, the suggested solution is 1- not unique for the dataset and 2- not necessarily physically meaningful (Vermeesh and Tian, 2014). It is then important to validate the models with independent geological and thermal data to discriminate between scenarios.

For samples SOR19 and ARS06, vitrinite reflectance data give Ro values of about 0.3% that indicate maximum temperature conditions close to the AHe closure temperature (Tc). This is supported by the comparison with data from the Miocene turbiditic deposits of the Northern Apennines, where temperatures estimates based on AFT and Ro data yield 75 ºC corresponding

to Ro values of 0.29 % (Zattin et al., 2002). SOR 19 has two grains older than the depositional interval and therefore modelling results indicate pre-depositional temperatures higher than during and after deposition (Fig. 6). According to the modelling, temperature during deposition decreases and after deposition varies between 20 and 50 ºC until about 2 Ma. The thermal history, as we would expect it, would start with high temperatures before deposition, followed by surface temperatures at the beginning of deposition that increase progressively during deposition. Thus, the scenario proposed by the modelling of SOR 19 appears unlikely but it can be interpreted as indicating that a prolonged stay until 2 Ma at temperatures within the AHe PRZ but close to or below the AHe Tc could be sufficient to obtain the observed ages. The thermal history indicated by the modelling results for samples ARS 06 indicate maximum temperatures during deposition at about 8 Ma and close to 80 ºC. This is dictated by four grains with ages scattered between 8 and 6 Ma that are within the depositional interval. After deposition, modelling indicates permanence at temperature possibly still within the lower AHe PRZ until about 2 Ma. We have no geologic constraints to test the validity of this scenario. However, it is consistent with the scenario proposed sample SOR 19 in that they both indicate that cooling to surface temperatures might have not started before 2 Ma ago.

Vitrinite reflectance data for samples AGN31 and AGN33 indicate quite high Ro high values of 0.44%. In the Northern Apennines, similar Ro values of 0.43-0.44%, have been estimated as corresponding to a temperature of 95 ºC (Zattin et al., 2002), which is higher than the nominal AHe Tc. However, some grains of these samples are older than the depositional age and both samples have a clear positive correlation between ages and Rs indicating a strong control of different diffusion properties on the ages. For both samples, the thermal history proposed by the model can be interpreted as indicating that temperature conditions within the AHe PRZ during and after deposition until about 2 Ma are required to reproduce the observed ages. Thus, although few geologic constrains are available to test the validity of the modelled thermal histories, we suggest that the overall consistency and reproducibility of our outputs for all of the above samples backs up their plausibility.

Thermal modelling results for the age-elevation transect of the Monte Gorzano (Fig. 5) indicates maximum temperatures for the lowest sample (GOR50) close to 120 ºC. Such temperatures are consistent with Ro values of 0.46 % and with 3.5 km thickness estimates for the Laga Fm (Milli et al., 2013). It is important to note that the modelling suggests that cooling did not start until 2 Ma age despite the lowest sample has a fully reset, 5 Ma-old AFT age. According to the modelling, this age could be obtained by heating to temperatures between 90

and 120 ºC from 5 to 2 Ma followed by very rapid cooling after 2 Ma. Thus, the suggestion is that cooling would have not have started at 5 Ma but rather at 2 Ma.

5.1.4 Exhumation paths

The most important parameter that affects our inversion of ages to exhumation rates is the geothermal gradient (Willett and Brandon, 2013). In the western portion of the Central Apennines, the modern geothermal gradient is perturbed by the presence of the large Pleistocene-Quaternary Latium magmatic province. Modern heat flux values close to Rome can reach values over 400 mW m-2 (e.g. Cataldi et al. 1995; Chiodini et al., 2013). However, such high heat fluxes are confined within restricted areas and the most common heat flux values along the Tyrrhenian coastal area of our study area are, instead, in the range of 100 to 150 mW m-2. Close to Rome, these high values decrease eastward with a very sharp gradient down to values between 30 to 50 mW m-2 in the Apennine belt that hosts regional aquifers. Thus, the only samples that could be affected by the very high heat fluxes related to the Latium magmatic province are TYR 15 and CIR 62. Both these samples have cooling ages that are older than the volcanic rocks in this region indicating that they were already below the AHe PRZ zone when the magmatic activity started. Thus, we suggest that it is unlikely that the cooling ages of these samples were significantly affected by the high heat fluxes of this region.

Although the Central Apennines belt, east of the Latium magmatic province, are characterized by very low near-surface geothermal gradients, they reside above a regional heat flux anomaly extending 100-150 km eastward of the Tyrrhenian coast line (Chiodini et al., 2013). This high-temperature system is located in the lower crust or uppermost mantle and, therefore, low geothermal gradients should persist, instead, in the upper crust where the AFT and AHe closure depths are. In fact, these closure depths are no more than 5 km deep given nominal Tc of 116 ºC and 67 ºC for the AFT and AHe systems, respectively (Reiners and Brandon, 2006). Given the large uncertainties on the modern and past geothermal gradients in our study area, we choose to calculate erosion rates for two modern geothermal gradients (35 ºC/km and 55 ºC/km) which give geothermal gradients at the onset of erosion in the range of 13-27 ºC/km and 31-47 ºC/km, respectively. As onset of erosion, we choose times shortly after the end of deposition, when geothermal gradients could have been as low as 10-20 ºC/km as typical in foreland basins. Thus, a minimum modern geothermal gradient of 35 ºC/km appears as a good proxy. However, given the uncertainties on the modern geothermal gradients, to calculate the

exhumation paths of our samples, we used the average erosion rate as derived from both sets of input parameters. The maximum exhumation depth that we obtained for the lowest sample of the Monte Gorzano age-elevation transect, which comes from the bottom of the Laga Fm, is about 3.5 km. This depth corresponds to the maximum thickness of the Laga Fm (Milli et al., 2013) suggesting that our estimates are robust.

5.2 Thermotectonic evolution of the Central Apennines

Our results show diachronous cooling ages through the chain, which decrease towards the east (Figs. 4 and 7c). Single grain ages are never lower than 4 Ma westwards of the L'Aquila basin, whereas in the internal parts of the orogen, samples mostly yield ages as low as 1 – 2 Ma (Fig. 4). The resetting degree also becomes higher in the east, with increasingly more single grains younger than the deposition age (Fig. 4). These general trends reflect the tectonic evolution of the different units that compose the Central Apennines and that we discuss below progressing from west to east.

5.2.1 Cooling of different tectonic units

Our oldest cooling ages, up to 7.6 Ma, are from samples TYR15 and CIR62 along the Tyrrhenian coast. These samples belong to a tectonic unit that was overthrusted during the Serravalian (13.8-11.6 Ma) (Cipollari and Cosentino, 1997). Cooling ages match the onset of offshore normal fault activity in the area related to back-arc extension during the Late Miocene (Patacca, 1992). From seismic line interpretation, the offset of these faults has reached up to 3 km offshore of sample TYR15 (Mascle and Rehault, 1990; Karsten and Mascle, 1990), which is sufficient to exhume rocks from within the AFT annealing zone. Similar normal faulting has been observed close to CIR62, onset during Tortonian-Early Messinian and ongoing until the Late Messinian, as testified by the offset of Messinian Salinity Crisis deposits (Cippollari et al., 1999, and references therein).

Samples deposited in the Messinian foredeep are split between two tectonic units. OLE20, SGU12, GTA03 and GTA05, as well as MOL23 and MOL24 were overthrusted during the Early Messinian (7.2-6 Ma), due to the activity of the Simbruini thrust fault (Cipollari and Cosentino, 1995). Thrusting could have resulted in uplift of this unit above sea level and therefore in exposure to erosion so that the cooling ages of those samples, ranging from 5 to 6

Ma, can be attributed to the activity of this fault. The low resetting degree of samples from this unit correlates with the small lag time between deposition and exhumation, which doesn't allow for long burial of the unit. GOR50 to GOR55, LAG42, AGN31, AGN33, ARS06, SOR19, COL63, MAI38 and MOL27 to MOL30 are part of the tectonic unit transported during the Late Messinian - Early Pliocene (~5.3 Ma) (Cosentino et al., 2010 and references therein). COL63 and MAI38 yield cooling ages of ~ 4-5 Ma, which correlate with age of thrusting. However, MAI38 is based on a single grain age only. The other reset ages from this tectonic unit (LAG42, GOR50 to GOR55, MOL27 to MOL30) show AHe ages around 2-3 Ma. A previous study also reports two AHe ages in the southern Laga basin, dated 2.35 ± 0.11 Ma (Satolli et al., 2014). Model results from the Monte Gorzano vertical profile (Fig. 5) confirm this rapid cooling starting around 2 Ma, as suggested by the AHe data. It is unclear whether the related AFT ages around 5-6 Ma, before the thrusting of this unit, suggest an early onset of slow exhumation shortly after deposition, or whether, as indicated by the modelling, they are consistent with onset of rapid cooling at 2 Ma. The model results for the partially reset ages of this unit (SOR19, ARS06, AGN31 and AGN33) suggest a possible recent cooling phase around 1-3 Ma for each of those samples, after a post-depositional stay in the PRZ. Although generally not recorded by single grain ages, the recent cooling phase inferred by models is consistent with AHe ages from the reset samples, both in the Laga and Molise areas. Average exhumation rates in the last 2 Ma derived from Agetoedot are as high as 0.7 ± 0.3 km/Ma (1s) along the Monte Gorzano transect in the Laga region (GOR50 to GOR55) and 0.6 ± 0.3 km/Ma in Molise (MOL27, MOL28, MOL30) (Fig. 7).

5.2.2 Exhumation at 2 Ma

In the Laga basin, samples GOR50 to GOR55 are in the footwall of a post-orogenic extensional fault, whose activity started probably during the Miocene (Mazzoli et al., 2002; Cosentino et al., 2010; Bigi et al., 2011). The AHe ages are coeval with the onset of this extension, and the 1-2 km offset of the fault derived from seismic data is enough to cause the exhumation of our samples. LAG42 comes from the hanging wall of the same fault, and yields a cooling age slightly older, yet within error, of GOR50 to GOR55. Among the 4 single grain ages of LAG42, three yield ages of 1-2 Ma, whereas one grain has an age of 6 Ma, which makes it difficult to assess if this sample is indeed older than the samples from the footwall. SOR19 and ARS06 were sampled in the hanging wall of extensional normal faults that bound the Val Roveto in

the east (Fig. 1) and that started to be active during the Middle Pleistocene (Fubelli et al., 2009). The total throw of this fault is less than 400 m (Roberts and Michetti, 2004). In the southeast of our study area (Molise), the exhumation signal around 2 Ma (MOL27 to MOL30, AGN31 and AGN33) does not appear as related to extension as our samples there were not collected in the vicinity of any normal fault (Fig. 3). Thus, the 2 Ma signal is only locally related to extensional faulting and it is common along the eastern side of the central Apennines from the Laga region through Val Roveto-l'Aquila to the Molise regions. In this area, that includes the backbone of the Central Apennines, the 2 Ma signal is related to about 2 km of exhumation (Fig. 7d). In this region, the occurrence of marine deposits at currently high elevation is evidence for recent surface uplift (Bartolini et al., 1996; Pizzi, 2003). Moreover, stable isotope paleoaltimetry indicate that the central Apennines started to attain their modern long-wavelength elevation 2 Ma (Fig. 7e; San Jose et al., submitted). Thus, during the last 2 Ma, topographic growth and exhumation in the eastern central Apennines occurred simultaneously, and locally it was amplified in the footwall of normal faults. Both the timing and the amount of exhumation and surface uplift further support the idea of a link between surface uplift and slab detachment in the Central Apennines as suggested by previous geodetic and geologic data (Faccenna et al., 2014).

6. Conclusions

This study provides new constraints on exhumation history in a key area where quantitative data was scarce. A combination of AHe, AFT and thermal modelling allowed to retrieve space-time cooling patterns since the Late Miocene, and link them to possible underlying processes.

- Syn-orogenic crustal thickening is recorded by diachronous cooling ages in the core of the orogen. Those samples located in the hanging wall of the thrusts yield exhumation ages concomitant with thrust activity and related surface uplift. Samples COL63, GTA03, OLE20 and MAI 38 record this early uplift event.

- Post-orogenic back-arc extension is evidenced on the Tyrrhenian coast by cooling ages of 5 to 8 Ma in the footwall of offshore normal faults.

- A large scale, rapid (> 0.6 km/Ma) exhumation phase starting in the Pliocene is recorded through the central and eastern parts of the orogen. Locally, this event can clearly be related to normal faulting (Gorzano fault), but is also recorded as a shallower exhumation through

Molise, Laga, and Val Roveto. This event is clearly recorded in samples with sufficient burial, and in areas close to the trench. In areas farther west, and in partially reset samples, this phase is only evidenced with the help of thermal modelling, but consistently appears through the chain. We attribute this event to a wide-spread phase of surface uplift and exhumation, possibly related to wave of dynamic topography caused by the opening of the Adriatic slab window.

REFERENCES

Aldega, L., Botti, F., and Corrado, S., 2007, Clay mineral assemblages and vitrinite reflectance in the Laga Basin (Central Appenines, Italy): What do they record? Clays and Clay Minerals, v. 55, p. 504–518, doi:10.1346/CCMN.2007.0550505.

Bally, A.W., Burbi, L., Cooper, C., and Ghelardoni, R., 1986, Balanced sections and seismic reflection profiles across the central Apennines: Memorie della Società Geologica Italiana, v. 35, p. 257–310.

Barker, C.E., and Pawlewicz, M.J., 1994, Calculation of Vitrinite Reflectance from Thermal Histories and Peak Temperatures: , p. 216–229, doi:10.1021/bk-1994-0570.ch014.

Bartolini, C., Caputo, R., and Pieri, M., 1996, Pliocene—Quaternary sedimentation in the Northern Apennine Foredeep and related denudation: Geological Magazine, v. 133, p. 255–273, doi:10.1017/s0016756800009006.

Bigi, S., Casero, P., and Ciotoli, G., 2011, Seismic interpretation of the Laga Basin; constraints on the structural setting and kinematics of the Central Apennines: Journal of the Geological Society, v. 168, p. 179–189, doi:10.1144/0016-76492010-084.

Bigi, S., Conti, A., Casero, P., Ruggiero, L., Recanati, R., and Lipparini, L., 2013, Geological model of the central Periadriatic basin (Apennines, Italy): Marine and Petroleum Geology, v. 42, p. 107–121, doi:10.1016/j.marpetgeo.2012.07.005.

Casero, P., 2004, Structural setting of petroleum exploration plays in Italy: Special Volume of the Italian Geological Society for the IGC 32, v. 107, p. 319–322.

Cataldi, R., Mongelli, F., Squarci, P., Taffi, L., Zito, G., and Calore, C., 1995, Geothermal ranking of Italian territory: Geothermics, v. 24, p. 115–129, doi:10.1016/0375-6505(94)00026-9.

Centamore, E., Crescenti, U., and Dramis, F., 2006, Note Illustrative della Carta Geologica d'Italia alla scale 1:50 000 foglio 359 L'Aquila: v. 359, p. 1–128.

Chiarabba, C., De Gori, P., and Mele, F.M., 2015, Recent seismicity of Italy: Active tectonics of the central Mediterranean region and seismicity rate changes after the Mw 6.3 L'Aquila earthquake: Tectonophysics, v. 638, p. 82–93, doi:10.1016/j.tecto.2014.10.016.

Chiodini, G., Cardellini, C., Caliro, S., Chiarabba, C., and Frondini, F., 2013, Advective heat transport associated with regional Earth degassing in central Apennine (Italy): Earth and Planetary Science Letters, v. 373, p. 65–74, doi:10.1016/j.epsl.2013.04.009.

Cipollari, P., and Cosentino, D., 1995, miocene unconformities in the Central Apennines:geodynamic 74 Significance and sedimentary basin evolution: v. 252, p. 375–389.

Corrado, S., 1995, Optical parameters of maturity of organic matter dispersed in sediments: first results from the Central Apennines (Italy): Terra Nova, v. 7, p. 338–347, doi:10.1111/j.1365-3121.1995.tb00803.x.

Corrado, S., Aldega, L., Di Leo, P., Giampaolo, C., Invernizzi, C., Mazzoli, S., and Zattin, M., 2005, Thermal maturity of the axial zone of the southern Apennines fold-and-thrust belt (Italy) from multiple organic and inorganic indicators: Terra Nova, v. 17, p. 56–65, doi:10.1111/j.1365-3121.2004.00584.x.

Corrado, S., Di Bucci, D., Naso, G., Giampaolo, C., and Adatte, T., 1998, Application of organic matter and clay mineral studies to the tectonic history of the Abruzzo-Molise-Sannio area, Central Appenines, Italy: Tectonophysics, v. 285, p. 167–181, doi:10.1016/S0040-1951(97)00195-9.

Cosentino, D. et al., 2017, New insights into the onset and evolution of the central Apennine extensional intermontane basins based on the tectonically active L'Aquila Basin (central Italy): Bulletin of the Geological Society of America, v. 129, p. 1314–1336, doi:10.1130/B31679.1.

Cosentino, D. et al., 2008, Note Illustrative della carta geologica d'Italia alla scala 1:50.000 Foglio 357 Cittaducale:

Cosentino, D., Cipollari, P., Marsili, P., and Scrocca, D., 2010, Geology of the central Apennines: A regional review: Journal of the Virtual Explorer, v. 36, doi:10.3809/jvirtex.2009.00223.

Critelli, S., 2018, Provenance of Mesozoic to Cenozoic circum-Mediterranean sandstones in relation to tectonic setting: Earth-Science Reviews, v. 185, p. 624–648, doi:10.1016/j.earscirev.2018.07.001.

Faccenna, C., Becker, T.W., Miller, M.S., Serpelloni, E., and Willett, S.D., 2014, Isostasy, dynamic topography, and the elevation of the Apennines of Italy: Earth and Planetary Science Letters, v. 407, p. 163–174, doi:10.1016/j.epsl.2014.09.027.

Faure Walker, J.P., Roberts, G.P., Cowie, P.A., Papanikolaou, I., Michetti, A.M., Sammonds, P., Wilkinson, M., McCaffrey, K.J.W., and Phillips, R.J., 2012, Relationship between topography, rates of extension and mantle dynamics in the actively-extending Italian Apennines: Earth and Planetary Science Letters, v. 325–326, p. 76–84, doi:10.1016/j.epsl.2012.01.028.

Flowers, R.M., Ketcham, R.A., Shuster, D.L., and Farley, K.A., 2009, Apatite (U-Th)/He thermochronometry using a radiation damage accumulation and annealing model: Geochimica et Cosmochimica Acta, v. 73, p. 2347–2365, doi:10.1016/j.gca.2009.01.015.

Fubelli, G., Gori, S., Falcucci, E., Galadini, F., and Messina, P., 2009, Geomorphic signatures of recent normal fault activity versus geological evidence of inactivity: Case studies from the central Apennines (Italy): Tectonophysics, v. 476, p. 252–268, doi:10.1016/j.tecto.2008.10.026.

Gallagher, K., 2012, Transdimensional inverse thermal history modeling for quantitative thermochronology: Journal of Geophysical Research: Solid Earth, v. 117, p. 1–16, doi:10.1029/2011JB008825.

Gallagher, K., 2018 QTQt User Guide v5.7.0R

Gautheron, C., Tassan-Got, L., Barbarand, J., and Pagel, M., 2009, Effect of alpha-damage annealing on apatite (U-Th)/He thermochronology: Chemical Geology, v. 266, p. 157–170, doi:10.1016/j.chemgeo.2009.06.001.

van Hunen, J., and Allen, M.B., 2011, Continental collision and slab break-off: A comparison of 3-D numerical models with observations: Earth and Planetary Science Letters, v. 302, p. 27–37, doi:10.1016/j.epsl.2010.11.035. 75

Ketcham, R.A., Carter, A., Donelick, R.A., Barbarand, J., and Hurford, A.J., 2007, Improved modeling of fission-track annealing in apatite: American Mineralogist, v. 92, p. 799–810, doi:10.2138/am.2007.2281.

Ketcham, R.A., Gautheron, C., and Tassan-Got, L., 2011, Accounting for long alpha-particle stopping distances in (U-Th-Sm)/He geochronology: Refinement of the baseline case: Geochimica et Cosmochimica Acta, v. 75, p. 7779–7791, doi:10.1016/j.gca.2011.10.011.

Milli, S., Cannata, D., Marini, M., and Moscatelli, M., 2013, Facies and geometries of Lower Messinian Laga Basin turbidite deposits (central Apennines, Italy): Journal of Mediterranean Earth Sciences, v. 5, p. 179–196.

Patacca, E., Sartori, R., and Scandone, P., 1990a, Tyrrhenian basin and Apenninic Arcs: kinematic relations since Late Tortonian times.: Mem. Soc. Geol. It, v. 45, p. 425–451, doi:10.1007/978-94-011-2016-6_7.

Patacca, E., Sartori, R., and Scandone, P., 1990b, Tyrrhenian basin and Apenninic Arcs: kinematic relations since Late Tortonian times.: Mem. Soc. Geol. It, v. 45, p. 425–451.

Pizzi, A., 2003, Plio-Quaternary uplift rates in the outer zone of the central Apennines fold-and-thrust belt, Italy: Quaternary International, v. 101–102, p. 229–237, doi:10.1016/S1040-6182(02)00105-2.

Roberts, G.P., and Michetti, A.M., 2004, Spatial and temporal variations in growth rates along active normal fault systems: An example from The Lazio-Abruzzo Apennines, central Italy: Journal of Structural Geology, v. 26, p. 339–376, doi:10.1016/S0191-8141(03)00103-2.

Royden, L., Patacca, E., and Scandone, P., 1987, Segmentation and configuration of subducted lithosphere in Italy: an important control on thrust-belt and foredeep-basin evolution.: Geology, v. 15, p. 714–717, doi:10.1130/0091-7613(1987)15<714:SACOSL>2.0.CO;2.

Rusciadelli, G., Viandante, M.G., Calamita, F., and Cook, A.C., 2005, Burial-exhumation history of the central Apennines (Italy), from the foreland to the chain building: Thermochronological and geological data: Terra Nova, v. 17, p. 560–572, doi:10.1111/j.1365-3121.2005.00649.x.

San Jose, M., Caves Rugenstein J., Cosentino, D. Faccenna, C., Fellin M.G., Ghinassi M., Martini, I., Rapid uplift of the central Apennines since the late Pliocene (Submitted)

Serpelloni, E., Faccenna, C., Spada, G., Dong, D., and Williams, S.D.P., 2013, Vertical GPS ground motion rates in the Euro-Mediterranean region: New evidence of velocity gradients at different spatial scales along the Nubia-Eurasia plate boundary: Journal of Geophysical Research: Solid Earth, v. 118, p. 6003–6024, doi:10.1002/2013JB010102.

Stalder, N.F., Fellin, M.G., Caracciolo, L., Guillong, M., Winkler, W., Milli, S., Moscatelli, M., and Critelli, S., 2018, Dispersal pathways in the early Messinian Adriatic foreland and provenance of

the Laga Formation (Central Apennines, Italy): Sedimentary Geology, v. 375, p. 289–308, doi:10.1016/j.sedgeo.2017.09.016.

Vermeesch, P., and Tian, Y., 2014, Thermal history modelling: HeFTy vs. QTQt: Earth-Science Reviews, v. 139, p. 279–290, doi:10.1016/j.earscirev.2014.09.010.

Willett, S.D., and Brandon, M.T., 2013, Some analytical methods for converting thermochronometric age to erosion rate: Geochemistry, Geophysics, Geosystems, v. 14, p. 209–222, doi:10.1029/2012GC004279.

Wortel, M.J.R., and Spakman, W., 2000, Subduction and slab detachment in the Mediterranean-Carpathian region: Science, v. 290, p. 1910–1917, doi:10.1126/science.290.5498.1910.

Zattin, M., Picotti, V., and Zuffa, G.G., 2002, Fission-track reconstruction of the front of the Northern Apennine thrust wedge and overlying Ligurian unit: American Journal of Science, v. 302, p.76 346–379, doi:10.2475/ajs.302.4.346.

Zhong, S., and Gurnis, M., 1994, Controls on trench topography from dynamic models of subducted slabs: Journal of Geophysical Research, v. 99, p. 15683, doi:10.1029/94JB00809.

Neogene exhumation pattern of the central Apennines (Italy) constrained by low-temperature thermochronology

SUPPLEMENTARY MATERIAL

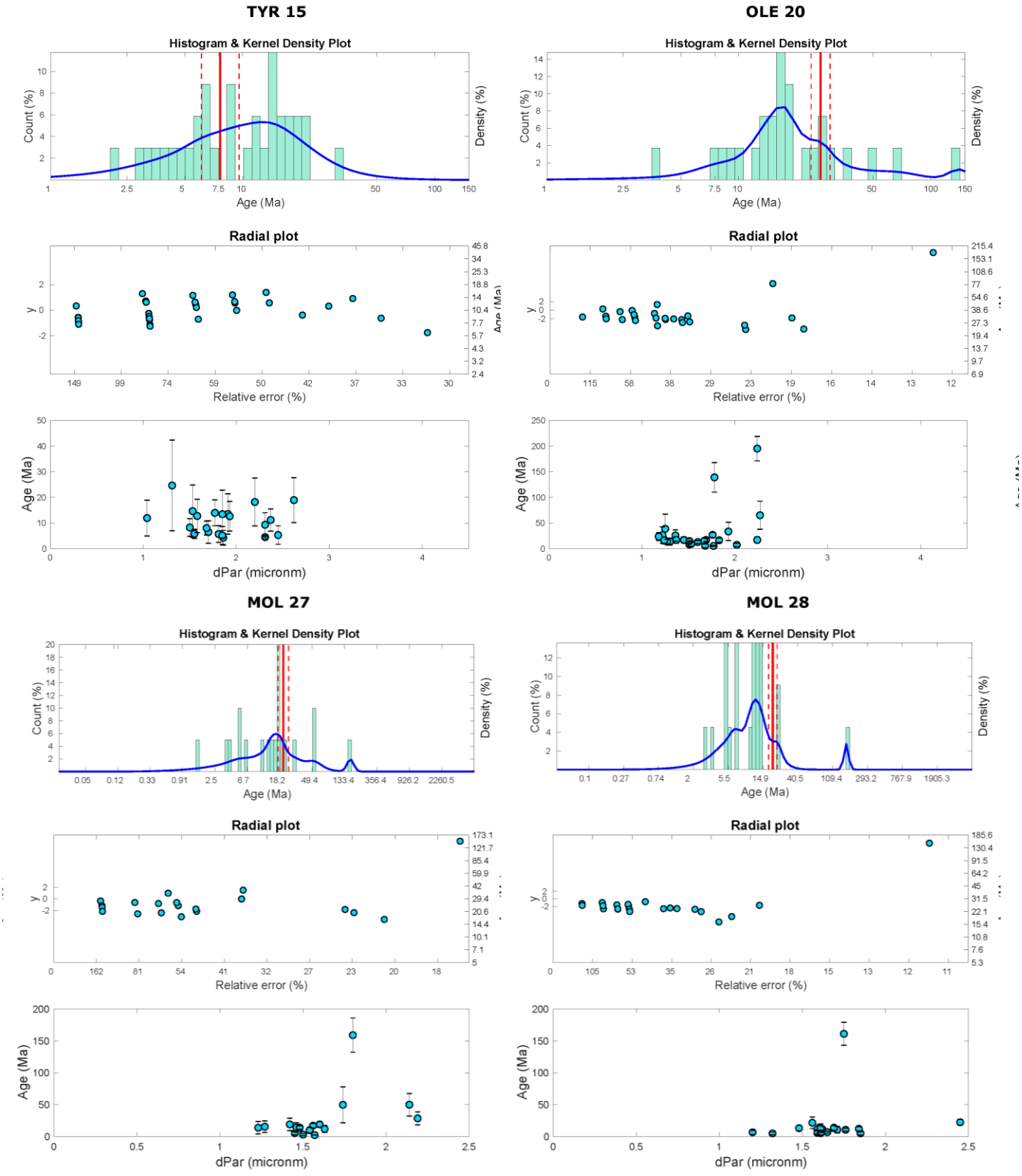

Figure S1. AFT data

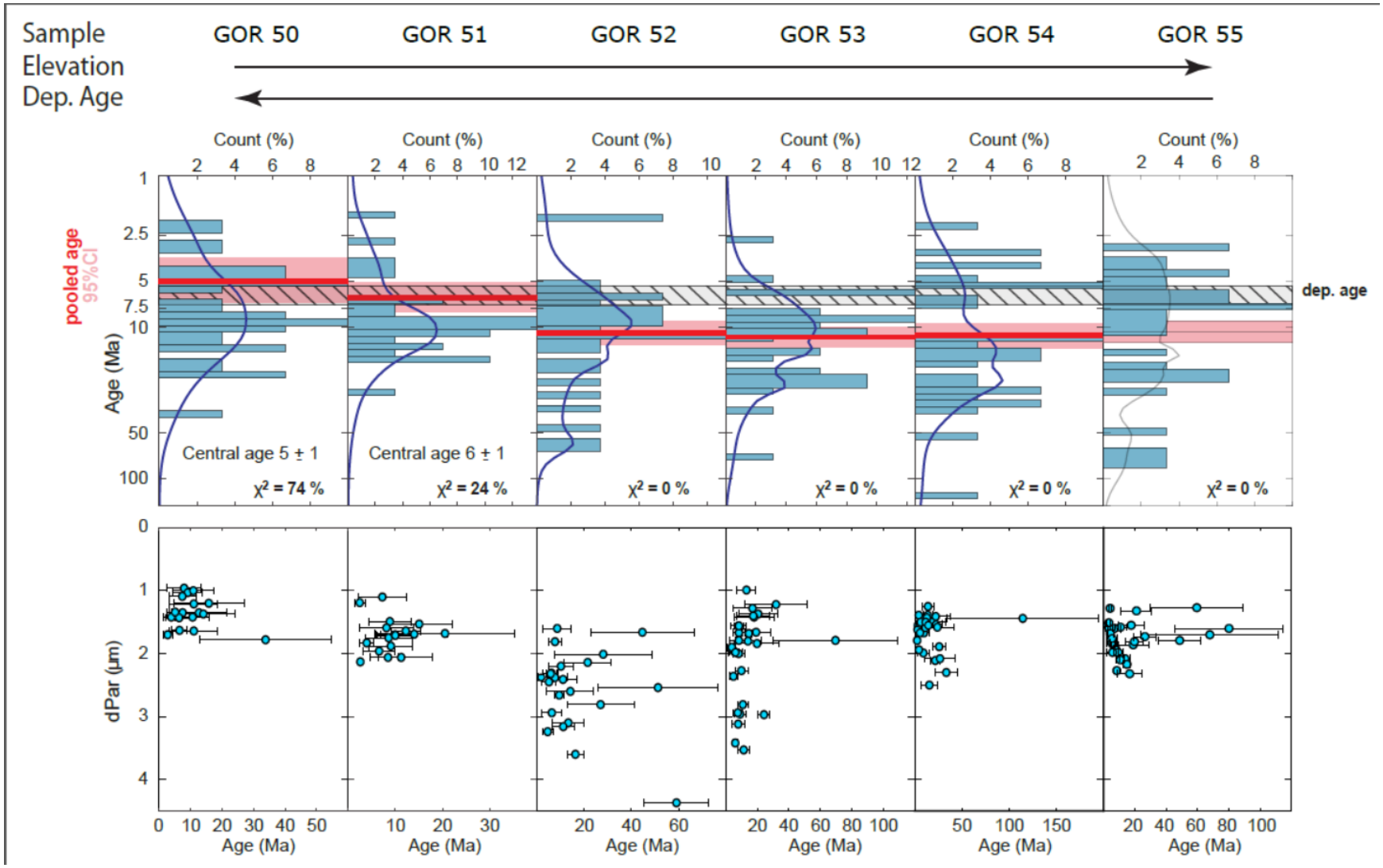

Figure S2. AFT data for the vertical profile from the Laga formation.

Region	ID.n.	SAMPLE	GRAIN	Mid Dep. Age (Ma)	τ (Ma)	Rs (μm)	Gobs (ºC/km)	Gobs2 (ºC/km)	Ω (1/s)	Tc10 (ºC)	Ea (J/mol)	t1 (Ma)	$\dot{e}$ (km/Ma)	$\dot{e}_2$ (km/Ma)	G0 (ºC/km)	G02 (ºC/km)	Dc (km)	Dc2 (km)
TYR	1	TYR15		83.00	7.60		35	55	2.05E+06	116.00	147000	8.0	0.45	0.27	27.41	47.35	3.55	2.11
TYR	1.1	TYR15	TYR15A1	83.00	5.99	57.00	35	55	2.45E+08	65.79	138000	8.0	0.21	0.13	31.32	51.19	1.32	0.81
TYR	1.2		TYR15A2	83.00	6.83	28.90	35	55	1.36E+08	56.99	138000	8.0	0.20	0.12	31.42	51.42	1.41	0.87
TYR	2.1	CIR62	CIR62A1	21.74	5.55	32.30	35	55	2.24E+08	58.40	138000	8.0	0.23	0.14	30.79	50.79	1.37	0.84
TYR	2.2		CIR62A2	21.74	6.41	50.90	35	55	4.13E+08	64.29	138000	8.0	0.17	0.11	31.92	51.94	1.15	0.71
TYR	2.2		CIR62A3	21.74	4.38	30.90	35	55	4.62E+08	57.83	138000	8.0	0.27	0.17	30.21	50.28	1.29	0.78
TYR	2.2		CIR62A4	21.74	6.22	88.20	35	55	1.64E+08	71.70	138000	8.0	0.21	0.13	31.12	51.10	1.40	0.86
TYR	2.2		CIR62A5	21.74	6.42	77.00	35	55	2.69E+08	69.84	138000	8.0	0.19	0.12	31.54	51.64	1.26	0.78
LATINA	3.1	OLE20	OLE20A1	9.40	4.27	47.80	35	55	1.22E+08	63.46	138000	8.0	0.35	0.22	28.96	48.95	1.69	1.01
LATINA	3.2		OLE20A2	9.40	7.34	35.00	35	55	2.64E+08	59.42	138000	8.0	0.16	0.10	32.04	52.04	1.20	0.75
LATINA	7.1	GTA03	GTA03A1	7.80	5.40	38.10	35	55	9.06E+07	60.52	138000	8.0	0.28	0.17	30.01	50.00	1.64	0.99
LATINA	7.2		GTA03A2	7.80	7.37	41.20	35	55	1.57E+08	61.53	138000	8.0	0.18	0.11	31.81	51.73	1.33	0.83
ROVETO	8.1	COL63	COL63A1	5.62	4.75	52.30	35	55	5.47E+07	64.65	138000	5.3	0.36	0.22	29.81	49.88	1.78	1.08
ROVETO	8.2		COL63A3	5.62	4.19	40.80	35	55	1.35E+08	61.40	138000	5.3	0.36	0.22	29.81	49.80	1.60	0.97
ROVETO	8.3		COL63A4	5.62	5.31	36.90	35	55	1.41E+08	60.10	138000	5.3	0.22	0.15	31.70	51.40	1.19	0.80
ROVETO	9.1	ARS06	ARS06A1	9.40	6.28	41.80	35	55	2.83E+08	61.72	138000	8.0	0.19	0.12	31.57	51.47	1.26	0.78
ROVETO	9.2		ARS06A2	9.40	7.28	56.40	35	55	4.13E+08	65.65	138000	8.0	0.15	0.12	32.33	32.33	1.10	0.89
ROVETO	9.3		ARS06A4	9.40	4.94	31.70	35	55	1.36E+08	58.16	138000	8.0	0.29	0.18	29.95	49.83	1.57	0.95
ROVETO	9.4		ARS06A5	9.40	5.93	32.40	35	55	5.79E+07	58.44	138000	8.0	0.27	0.17	30.20	50.13	1.72	1.04
ROVETO	9.5		ARS06A6	9.40	7.71	47.50	35	55	8.04E+07	63.39	138000	8.0	0.19	0.12	31.58	51.57	1.45	0.91
LAGA	11	GOR50		6.55	4.99		35	55	2.05E+06	116.00	147000	6.5	0.74	0.44	24.35	44.53	4.26	2.38
LAGA	11.1	GOR50	GOR50A1	6.55	1.93	51.50	35	55	1.04E+08	64.45	138000	6.5	0.91	0.56	22.54	41.90	2.49	1.35

LAGA	11.2		GOR50A2	6.55	1.54	32.30	35	55	2.64E+08	58.40	138000	6.5	1.02	0.63	21.45	40.51	2.37	1.26
LAGA	11.3		GOR50A4	6.55	1.72	37.40	35	55	1.97E+08	60.28	138000	6.5	0.94	0.58	22.27	41.50	2.34	1.27
LAGA	12.1	GOR51	GOR51A1	6.55	1.90	43.60	35	55	1.45E+08	62.26	138000	6.5	0.88	0.54	22.96	42.30	2.35	1.28
LAGA	12.2		GOR51A2	6.55	1.55	55.60	35	55	8.90E+07	65.46	138000	6.5	1.20	0.74	19.82	38.43	2.99	1.55
LAGA	12.3		GOR51A4	6.55	1.76	74.60	35	55	4.94E+07	69.41	138000	6.5	1.13	0.69	20.42	39.29	3.07	1.61
LAGA	13.1	GOR52	GOR52A1	6.55	1.26	34.10	35	55	2.36E+08	59.09	138000	6.5	1.32	0.81	18.83	37.08	2.83	1.44
LAGA	13.2		GOR52A4	6.55	1.75	33.90	35	55	2.39E+08	59.02	138000	6.5	0.89	0.55	22.73	42.09	2.22	1.21
LAGA	13.3		GOR52A5	6.55	1.91	50.30	35	55	1.09E+08	64.14	138000	6.5	0.91	0.56	22.50	41.87	2.48	1.35
LAGA	14	GOR53	GOR53A1	6.55	2.60	59.40	35	55	7.79E+07	66.34	138000	6.5	0.67	0.42	25.25	44.92	2.22	1.26
LAGA	15.1	GOR54	GOR54A1	6.55	1.63	46.70	35	55	1.26E+08	63.16	138000	6.5	1.08	0.66	20.95	39.95	2.67	1.41
LAGA	15.2		GOR54A2	6.55	1.74	32.10	35	55	2.67E+08	58.32	138000	6.5	0.88	0.55	22.91	42.13	2.18	1.19
LAGA	15.3		GOR54A3	6.55	1.39	68.80	35	55	5.81E+07	68.31	138000	6.5	1.46	0.89	17.67	35.83	3.57	1.77
LAGA	15.4		GOR54A4	6.55	3.71	40.10	35	55	1.71E+08	61.18	138000	6.5	0.39	0.24	28.87	48.76	1.64	0.98
LAGA	15.5		GOR54A5	6.55	1.81	38.30	35	55	1.87E+08	60.58	138000	6.5	0.89	0.55	22.74	42.06	2.29	1.25
LAGA	16.1	GOR55	GOR55A1	6.55	1.85	34.10	35	55	2.36E+08	59.09	138000	6.5	0.84	0.52	23.36	42.64	2.16	1.19
LAGA	16.2		GOR55A2	6.55	1.91	42.80	35	55	1.50E+08	62.02	138000	6.5	0.87	0.54	22.99	42.32	2.32	1.27
LAGA	16.3		GOR55A4	6.55	3.96	51.70	35	55	1.03E+08	64.50	138000	6.5	0.40	0.25	28.81	48.80	1.76	1.05
LAGA	16.4		GOR55A5	6.55	1.81	43.80	35	55	1.43E+08	62.32	138000	6.5	0.93	0.58	22.37	41.56	2.43	1.31
LAGA	17.1	LAG2	LAG42A2	6.55	6.45	41.70	35	55	1.26E+08	61.68	138000	6.5	0.20	0.13	31.79	51.55	1.28	0.83
LAGA	17.2		LAG42A3	6.55	2.20	34.10	35	55	7.54E+07	59.09	138000	6.5	0.82	0.51	23.57	42.91	2.45	1.35
LAGA	17.3		LAG42A4	6.55	2.87	45.40	35	55	8.46E+07	62.79	138000	6.5	0.59	0.37	26.14	45.95	2.09	1.20
LAGA	17.4		LAG42A5	6.55	3.34	38.80	35	55	3.29E+08	60.75	138000	6.5	0.40	0.25	28.79	48.78	1.50	0.90
MOLISE	18	MOL28	MOL28A1	8.45	2.66	34.20	35	55	1.58E+08	59.13	138000	6.5	0.59	0.36	26.32	46.09	1.92	1.11
MOLISE	21	MAI38	MAI38A1	7.70	4.38	31.20	35	55	1.76E+08	57.96	138000	6.5	0.32	0.20	29.86	49.84	1.53	0.93
MOLISE	22.1	MOL27	MOL27A3	8.45	2.00	45.10	35	55	2.01E+08	62.71	138000	6.5	0.79	0.49	23.92	43.28	2.13	1.18

MOLISE	22.2		MOL27A4	8.45	1.23	44.10	35	55	2.00E+08	62.41	138000	6.5	1.39	0.85	18.21	36.43	3.00	1.51
MOLISE	23.1	MOL30	MOL30A1	8.45	5.41	35.70	35	55	2.36E+08	59.68	138000	6.5	0.24	0.15	31.18	51.16	1.34	0.83
MOLISE	23.2		MOL30A2	8.45	2.16	45.50	35	55	1.33E+08	62.82	138000	6.5	0.77	0.47	24.10	43.65	2.22	1.23
MOLISE	23.3		MOL30A3	8.45	2.40	47.30	35	55	1.83E+08	63.33	138000	6.5	0.65	0.40	25.56	45.23	1.97	1.12

Table S1. Agetoedot parameters. Under Region, TYR refers to the Tyrrhenian coast; Mid. Dep. Age: midpoint between upper and lower bounds of the depositional age interval ; τ: cooling age; Rs: effective spherical radius for the diffusion domain; Gobs and Gobs2: final geothermal gradients; Ω: frequency factor; Tc10: closure temperature at a cooling rate of 10 ºC/Ma; Ea: activation energy; t1 : onset time for erosion; $\dot{e}$ and $\dot{e}2$: erosion rates; G0 and G02: geothermal gradients at the erosion onset; Dc and Dc2: closure depth.

CONCLUSION AND OUTLOOK

The central Apennines provide a unique setting where exhumation data and paleoaltimetry records overlap in time. This combination allows to independently define rates and amplitudes of rock and surface uplift. Both approaches reveal a strong evidence for a large scale uplift event around 2 Ma, which correlates with the magnitude and timing of surface evolution expected from a slab-break-off event. However, this interpretation is solely based on correlation, and we can't entirely rule out the possibility of a different geodynamic process resulting in the same surface expression.

To further understand the link between topographic evolution and mantle processes in the Central Apennines, we will need to quantify the coupled interactions between crustal thickening, isostatic adjustment, erosional and topographic unloading, and how a transient system responds to those perturbations. A first step towards quantifying dynamic topography is to constrain the amount of shortening and thickening of the orogen, in order to assess the isostatic compound of topography. Determining the effect (and, eventually the feedbacks) of erosional unloading on fault activity and relief evolution will allow to directly quantify its contribution in topography building and/or destruction.